Influence of Carbonate on the Radium Uptake by Barite and Witherite

Zur Erlangung des akademischen Grades eines

DOKTORS DER NATURWISSENSCHAFTEN

(Dr. rer. nat.)

von der KIT-Fakultät für Chemie und Biowissenschaften

des Karlsruher Instituts für Technologie (KIT)

genehmigte

DISSERTATION

durchgeführt am Institut für Nukleare Entsorgung (INE) des KIT

von

M.Sc. Mohammed Abdullah Alzaydan

1. Referent: Prof. Dr. Horst Geckeis

2. Referent: Priv.-Doz. Dr. Frank Heberling

Tag der mündlichen Prüfung: 21.10.2024

Statement of Originality – Eidesstattliche Erklärung

Ich versichere wahrheitsgemäß, die vorliegende Arbeit selbstständig verfasst, alle benutzten Hilfsmittel vollständig und genau angegeben und alles kenntlich gemacht zu haben, was aus Arbeiten Anderer unverändert oder mit Abänderungen entnommen wurde, sowie die Satzung des KIT zur Sicherung guter wissenschaftlicher Praxis in der jeweils gültigen Fassung beachtet zu haben. Des Weiteren versichere ich, dass die Arbeit in ähnlicher oder gleicher Form noch keiner Prüfungskommission vorgelegt wurde.

Ort, Datum

Karlsruhe, 01.11.2024

Acknowledgements

At this point, I would like to express my deep gratitude to all those who contributed to the success of this work through their guidance and support.

First and foremost, I am extremely grateful to the head of the KIT-INE institute, Prof. Dr. Horst Geckeis, for giving me the opportunity to work on my dissertation in this fascinating field and for the many insightful and productive discussions we had along the way.

Next, I would like to extend my heartfelt appreciation to my division head, Dr. Volker Metz, whose positivity, kindness, and constant encouragement kept me motivated and focused throughout this journey.

A special expression of gratitude goes to my advisor, Dr. Frank Heberling, for his invaluable assistance, continuous feedback, and insightful conversations on the interpretation of results, as well as for contributing many new ideas that shaped the completion of this work. Your support in both experimental approaches and geochemical modeling was irreplaceable.

Additionally, I am profoundly grateful to Dr. Robert Polly for his help with computational techniques and for his patience in guiding me through the learning process.

A big thank you goes to the Analytical Department of KIT-INE: Dr. Nicolas Finck for his help with XRD measurements and related software; Dr. Dieter Schild for his indispensable support with SEM, SEM-EDX, XPS, video-microscope, and Raman spectroscopy; Dr. Oliver Dieste Blanco, Eva Soballa, and Dr. Natalia Müller for their assistance with SEM, SEM-EDX, and FIB-SEM analyses; Frank Geyer for ICP-MS analyses; Stefanie Kraft for ICP-OES; and Markus Fuss for γ-spectroscopy measurements and analyses. I am equally thankful to Tanja Kisely for her unwavering support with the lab's technical requirements and essential materials.

I am also grateful to my friends Lukas Zunftmeister, Thomas Roth, and Dr. Francesca Quinto for their invaluable friendship and unwavering support throughout this journey.

To all the other INE staff members not mentioned by name, I would like to acknowledge your contributions to the excellent work environment and for making my time at INE truly memorable.

I also extend my profound appreciation to Dr. Felix Brandt and Dr. Martina Klinkenberg from Forschungszentrum Jülich for their expertise and support in conducting Focused Ion Beam Scanning Electron Microscopy (FIB-SEM), which greatly contributed to the success of this work.

Last but not least, I want to express my heartfelt gratitude to my parents for their continuous prayers, unconditional support, and unwavering belief in me. Their guidance and love have been a cornerstone in shaping the person I am today.

To my young family, especially my wife, I want to express my deep gratitude. Your unwavering support, despite the challenges we faced, has been a source of strength and perseverance for me. I also wish to thank my children, whose understanding and patience—despite their young age—filled me with inspiration and motivation during this journey.

This doctoral thesis was funded by King Abdulaziz City for Science and Technology (KACST) and the German Federal Ministry of Education and Research (BMBF) through the collaborative project (KRIMI), grant agreement 02NUK056A.

Abstract

This Ph.D. thesis addresses the recrystallization of barite, $BaSO_4$(s), in carbonate bearing aqueous solution into witherite, $BaCO_3$(s), and the influence of carbonate on radium incorporation into both minerals. The uptake of Ra by barite has been investigated for many decades in the context of various environmental and industrial settings, such as Ra retention in nuclear waste repositories, Ra accumulation due to scaling processes in geothermal energy plants and in pipelines of petroleum production fields, removal of Ra from brackish groundwater in desalination plants, as well as other settings of Naturally Occurring Radioactive Materials.

Radium uptake by barite occurs when dissolved Ra^{2+}(aq) cations react with barite, leading to Ra retention by formation of a $(Ba,Ra)SO_4$ solid-solution. In studies under ambient geochemical conditions, it has been shown that barite crystals can recrystallize and spontaneously adapt their composition to the solution conditions through dissolution and re-precipitation processes, and incorporate Ra and other trace elements into the crystal structure of the barite host mineral. The database for describing $(Ra,Ba)SO_4$(s) mixture thermodynamics has improved considerably in recent years. In addition, quantum chemical methods for determining the equilibrium position of Ra in such solid solutions have become established. However, experimental work also shows that equilibration times can vary between one year and extrapolated time spans of about ten thousands of years depending on the specific sample characteristics and pre-treatment of the initial barite mineral. This demonstrates that a reliable consideration of the Ra immobilization potential of a solid solution requires not only a sound thermodynamic description but also a fundamental quantitative understanding of the kinetics of the reactions involved.

In contrast to the knowledge on Ra uptake by barite via formation of a $(Ra,Ba)SO_4$(s) solid solution, little is known about the uptake of Ra by witherite. The starting hypothesis for this work was that the reaction of barite with dissolved CO_3^{2-}(aq) anions at elevated pH can lead to the recrystallization of barite into witherite via dissolution and consecutive precipitation processes, resulting in the formation of a $(Ra,Ba)CO_3$(s) solid solution. Besides a quantitative description of the $(Ra,Ba)CO_3$(s) mixture thermodynamics, the kinetics of the potential $(Ra,Ba)SO_4$(s) to $(Ra,Ba)CO_3$(s) recrystallization process is of interest. The presence of carbonate likely alters the chemical behavior of barite surfaces, via surface mixing or by witherite layer formation through dissolution-precipitation which in turn has an effect on the uptake process.

The final aim of this work is to explore the fate of Ra bearing barite during the recrystallization process of barite in the presence of carbonate. By integrating experimental, analytical and computational approaches, the influence of carbonate concentration in solution, thereby the influence of degree of oversaturation, and the influence of barite mineral properties on the recrystallization of $BaSO_4$(s) to $BaCO_3$(s) is intensively studied. Based on the achieved knowledge about the recrystallization of the barite to witherite, incorporation of radium into the two host minerals is investigated. Since strontium occurs as trace element in natural $(Sr,Ba)SO_4$(s) and $(Sr,Ba)CO_3$(s) solid solutions, the fate of Sr during the recrystallisation of a natural Sr-bearing barite to witherite is studied as an analogy for the fate of Ra to provide further insights into the transformation of $(Ra,Ba)SO_4$(s) to $(Ra,Ba)CO_3$(s) in the presence of carbonate.

The influence of carbonate on the Ra uptake by barite and witherite is studied in batch type recrystallisation experiments with large barite cubes and microcrystalline barite powders as well as in coprecipitation batch type coprecipitation experiments with Ba^{2+}(aq) + SO_4^{2-}(aq) + Ra^{2+}(aq) and Ba^{2+}(aq) + CO_3^{2-}(aq) + Ra^{2+}(aq) bearing solutions, respectively. In the recrystallisation experiments, coarse grained natural barite samples from Androvo (Bulgaria) and Iberg (Germany), freshly precipitated barite and commercial synthetic high purity barite powder (Sachtleben Chemie GmbH, Germany) are used as starting materials. Besides ultra-pure Sachtleben barite powder used in barite and witherite recrystallization experiments, powder samples of Sachtleben barite, which had been equilibrated with $^{226}Ra^{2+}$(aq) bearing and carbonate-free solutions for seven years is used in (Ra,Ba)SO_4(s) to (Ra,Ba)CO_3(s) recrystallization experiments.

Different analytical and spectroscopic methods like scanning electron microscopy and energy / wavelength dispersive X-ray spectroscopy (SEM-EDS / WDS), Raman spectroscopy, X-ray photoelectron spectroscopy (XPS), X-ray powder diffraction (XRD) as well as inductively coupled plasma-optical emission spectrometry (ICP-OES) and γ-spectroscopy are applied for the analysis of the composition of crystals and solutions studied in the batch experiments. A SEM equipped with a focused ion beam (FIB) cutting device is used for removing ultra-thin layers from surfaces of selected samples to reveal interior structures of altered barite. Using a combined FIB-SEM approach, precise imaging with nanometer resolution and simultaneous chemical analysis of the barite/witherite reaction fronts is achieved. In addition to the analytical and experimental methods, numerical simulations based on the Density Functional Theory (DFT) is used as a quantum-mechanical atomistic simulation tool to obtain electronic energies and atomic structures of the barite and witherite host minerals and the solid solutions (Ra,Ba)SO_4(s) and (Ra,Ba)CO_3(s). In case of the solid solution simulations, DFT-based electronic energies are employed in the Single Defect Method (SDM) approach to calculate the extent of solid solution non-ideality. Moreover geochemical modelling by means of the PHREEQC software package is used to calculate saturation levels, solid solutions mixing, precipitation of solid phases and diffusion processes at the barite / witherite reaction front.

In series of recrystallisation experiments under various temperatures, degrees of carbonate concentration and pH in solution it is observed that recrystallization of barite to witherite is a rather slow process in case of macroscopic single crystal cubes of Androvo and Iberg barite. It turned out that only under quite extreme conditions (60°C, 0.1 M Na_2CO_3, pH 11) the replacement (coupled recrystallization) of barite into witherite takes place to a measurable extent within the studied period of five weeks. Microscopic analyses of the initial and replaced barite cubes demonstrate that for the progress of the reaction, in particular the development of the porosity of the growing witherite layer is of importance. With increasing reaction time, the dissolution of barite and the formation of witherite slows down. The experimental results indicate that passivation of the surface by the growing witherite is to be expected over longer periods of time. Compared to results of PHREEQC calculations for full equilibration of the solid-solution system, the theoretical possible formation of approximately 40 wt.% witherite is not achieved or is only achieved over extremely long periods of time even in replacement experiments with barite cubes in 0.1 M Na_2CO_3 at pH 11 and 60°C. In crystal cubes of pure Androvo barite, a sharp interface between barite and witherite, associated with a sharp decrease in sulfur and an increase in carbon is observed. According to the thermodynamically expected distribution coefficients in (Sr,Ba)SO_4(s) to (Sr,Ba)CO_3(s) solid solutions, a significant change

in the Sr/Ba ratio from the initial Sr-bearing Iberg barite to precipitated witherite would be expected. However, in experiments with Iberg barite the Sr/Ba ratio across the interface between barite and witherite does not change significantly. This indicates that at the barite-witherite interface where the replacement reaction proceeds, the cations released by barite dissolution are incorporated into witherite as they come, and that the thermodynamic affinities for incorporation into witherite under these transport-controlled conditions play no / or only a very minor role.

The initial reaction progress in recrystallization experiments with microcrystalline powder samples of natural Androvo barite, natural Iberg barite and of synthetic Sachtleben barite appears to be similar to that of the macroscopic Androvo and Iberg barite single crystal cubes. After a fast start, the transformation (uncoupled recrystallization) slows down and does not reach the theoretically achievable limit as calculated by means of PHREEQC for full equilibration of the solid-solution system. Still, the transformation of barite to witherite is considerably faster in the experiments with Androvo and Iberg barite powders compared to those with the respective single crystal cubes. Sachtleben and Iberg barite powders react at a closer rate. Similar to the kinetic trends in the replacement experiments with macroscopic single crystal cubes, the Androvo samples, which are ground from macroscopic single crystals, also shows in the powder transformation experiments a significantly lower reactivity compared to the reactivity of the Iberg barite powder. Experiments with Androvo and Iberg barite powder samples show that powders are by no means just small single crystals, but that an enormously increased complexity of the processes taking place can be observed here due to shifts in the reaction rates. SEM-EDX investigations demonstrate that in the powders, surface crystal rebuilding / transformation at a reactive barite-witherite interface plays a subordinate role. Instead, barite dissolves, while witherite crystals often form in idiomorphic shapes in various spatial arrangements with respect to the initial barite. The ratios between barite dissolution rate and witherite growth rate are decisive for this difference in the process sequence. If the barite dissolution is the slowest - rate-controlling process, a barite-witherite interface is formed, as in the single crystal experiments. If, on the other hand, witherite growth is slower than barite dissolution, and therefore rate-controlling, the witherite crystals grow increasingly independently of the initial barite.

In order to show what miscibility can be expected for radium incorporation in barite and witherite, both theoretical calculations using DFT and co-precipitation experiments are carried out. The DFT calculation results show that the incorporation of Ra in barite and witherite is almost ideal with rather small Guggenheim parameters ("non-ideality parameter") of 0.84 and 0.58, respectively. The value for Ra in barite agrees very well with calculated results of Vinograd et al., 2013. Using published solubility products of $BaSO_4$(s) and $RaSO_4$(s) at 60°C, a theoretical distribution coefficient of $D_{theo} = 0.42$ is calculated. Coprecipitation experiments with Ba^{2+}(aq) + SO_4^{2-}(aq) + Ra^{2+}(aq) at 60° result in a distribution coefficient of $D_{exp} = 0.34 \pm 0.14$ which is also in excellent agreement with the thermodynamically predicted value for (Ra,Ba)SO_4(s). Co-precipitation experiments for Ra-incorporation into witherite over a wide radium concentration range yield a distribution coefficient of $D_{exp} = 0.15 \pm 0.05$ for (Ra,Ba)CO_3(s). Only few literature data is available for the Ra-witherite system. An existing partition coefficient ($D = 0.13 \pm 0.07$ of Yoshida et al., 2015) agrees exactly with the measured (Ra,Ba)CO_3(s) composition. Together with the Guggenheim parameter of 0.58 for (Ra,Ba)CO_3(s) calculated in this Ph.D. work, this results in partition coefficients of D_{theo} =

0.06 , which closer to the lower limit of the value derived from the coprecipitation experiments with Ba^{2+}(aq) + CO_3^{2-}(aq) + Ra^{2+}(aq), i.e. D_{exp} = 0.15 ± 0.05. The attempt to simulate the incorporation of sulfate into witherite by means of DFT calculation leads to a highly distorted structure indicating an extreme non-ideality of the solid solution. This corresponds to the experimental findings that sulfate could never be detected in witherite from the recrystallization experiments. Experiments on the recrystallization of Sachtleben barite powders, which had been equilibrated with $^{226}Ra^{2+}$(aq) bearing and carbonate-free solutions for seven years, to Ra-bearing witherite shows that the various Ra-bearing barites investigated were quite inert. Interestingly, these long-time equilibrated (Ra,Ba)SO_4(s) powders are less reactive compared to a Ra-free Sachtleben barite powder, which had been equilibrated in parallel with $^{133}Ba^{2+}$(aq) bearing and carbonate-free solutions for seven years. Based on this observation, it is assumed that the Ra content in the barite host mineral actually has an inhibiting influence on the reactivity. Nevertheless, formation of microscopic (Ra,Ba)CO_3(s) crystals is observed. But these do not contain enough Ra for a quantitative evaluation of Ra incorporation after recrystallization.

The comprehensive work undertaken within this Ph.D. represents an important step forward in the scientific understanding of the knowledge of radium geochemistry and contributes to a broader understanding of radium behavior in both natural and anthropogenic contexts. In addition to its contribution to the understanding of the fate of radium, the findings on barite recrystallization into witherite contributes to knowledge of the broader field of mineral dissolution and precipitation processes.

Table of Contents

List of Figures

List of Appendix Figures

List of Tables

1 Introduction

1.1 Radium health impact and contamination pathways

Radium is the heaviest alkaline earth metal with its unstable isotopes, namely ^{224}Ra, ^{226}Ra, and ^{228}Ra that are naturally occurring radioactive materials (NORM) produced as decay products of uranium (^{238}U) and thorium (^{232}Th) in trace quantities in the earth crust (Matyskin et al., 2023; Vinograd et al., 2013). ^{226}Ra with its long half-life, 1600 years, poses health risks especially due to its accumulation in bones and bone marrow as it behaves chemically similar to calcium, potentially causing bone sarcoma (Matyskin et al., 2023; Rowland et al., 1978). The decay chain of ^{226}Ra includes various alpha, beta, and gamma emitting radionuclides, with the emission of the radioactive radon (^{222}Rn) being a significant concern. ^{222}Rn, with its short half-life, contributes significantly to background radiation dose, necessitating extra efforts in assessing and investigating^{226}Ra compounds (Matyskin, et al., 2023; Brandt et al., 2015). Despite the challenges posed by its radioactivity, understanding the behavior and impact of ^{226}Ra isotopes remain crucial in various industrial and environmental contexts.

Radium can find its way into different environmental contexts as a result of anthropogenic activities such oil, gas, coal explorations, mining, geothermal industry, groundwater treatment plants, drinking water wells as well as possible scenarios of migration from radioactive waste disposal sites (Heberling et al., 2018; Weber et al., 2017; Varley et al., 2016; Attallah et al., 2015; Kondash et al., 2014).

In the oil and gas industries, the formation of scales can lead to the accumulation of ^{226}Ra, co-precipitated with barite $BaSO_4$ in the form of $(Ba, Ra)SO_4$ solid solution, which pose concerns for the health workers and environments (Brown et al., 2019; Attallah et al., 2015; Desideri, 2006). In addition to the oil industry, geochemical processes associated with petroleum formation can concentrate ^{226}Ra and other radionuclides in source rocks. These radionuclides become mobilized when formation water, which is in contact with these rocks, dissolves and carries them to the surface. During oil/water separation processes, the dissolved ^{226}Ra can precipitate out, leading to contamination spots on equipment and storage tanks. This precipitation is often enhanced by changes in pressure, temperature, and chemical composition. This phenomenon results in the accumulation of ^{226}Ra containing materials such as scales, sludges, and drilling mud, all of which contribute to the broader issue of NORM and their

Technologically Enhanced Naturally Occurring Radioactive Materials (TENORM) counterparts (Attallah et al., 2015; Desideri et al., 2006; White and Rood, 2001). Furthermore, uranium mining and milling activities serve as significant sources of ^{226}Ra contamination, as trace amounts of radionuclides can leach into groundwater, causing concerns over ^{226}Ra transport and mobility in the environment (Yoshida et al., 2014; Martin et al., 2003).

In addition to oil, gas industries and uranium tailings, barite ($BaSO_4$) deposits formed during geothermal energy utilization, desalination processes, and even in drinking water wells, result in ^{226}Ra accumulation as $(Ba,Ra)SO_4$, reaching radioactivity levels of radiological concern, which necessitate careful handling and disposal to prevent hazardous impacts on health of human and the environment (Heberling et al., 2018; IAEA, 2004).

In scenarios concerning the long term evolution of high level nuclear waste disposal sites and upon the interactions between groundwater and waste packages that contain a few Kilograms per package of Ba as a fission product of ^{235}U as well as ^{226}Ra as a progeny of ^{238}U through a series of decays, the waste packages are expected to corrode after (<10000 to 100000 years); Barite precipitation may occur when Ba released from the waste packages through corrosion processes reacts with sulfate-rich groundwater (Cao, Xiaoyuan, et al., 2019; Brown et al., 2019; Heberling et al., 2018; Curti et al., 2010; Curti and Tits, 2005; Abdelouas et al., 1997). Furthermore, because ^{226}Ra will be in secular equilibrium with ^{238}U, most of ^{226}Ra will likely reside in sparingly soluble corrosion products of the waste materials , including the spent fuel composed of mainly of UO_2, and be released at a later stage after (10^5 years) of the sites evolution (Brown et al., 2019; Curti et al., 2010). Under such circumstances, the relevant process for $(Ba,Ra)SO_4$ solid solution formation will be via recrystallization processes rather than coprecipitation (Curti et al., 2010). This release of ^{226}Ra from the UO_2 matrix of the spent nuclear fuel and its incorporation into barite solid solutions are significant factors in assessing the radiological impact and implementing safety measures in nuclear waste disposal sites (Heberling et al., 2018).

1.2 Barite recrystallization into witherite in ^{226}Ra contained environments

The groundwater in the vicinity of radioactive waste disposal sites could contain high concentrations of carbonate and the temperature of water can be elevated (up to 80^0 C) for a certain period of time (<100 to 1000 years) due to substantial radioactive decay of the disposed spent fuel (Brown et al., 2019; Brown et al., 2015). In addition, the cementitious materials that are present in the disposal sites as a (geo-) technical barrier system protective system can lead

to local high pH plumes. The interactions of groundwater with cementitious materials will lead to the degradation of cementitious materials, and subsequently elevate pH value of the pore solutions (Berner, 1992). Upon a scenario of groundwater intrusion with high carbonate concentration as well as high pH and elevated temperature, barite recrystallization into witherite ($BaCO_3$) can occur. Such recrystallization is not limited to the radioactive disposal sites, but can occur in other industrial and environmental settings when processes conditions are met (Baldasari and Speer, 1979; Rendón-Angeles et al., 2008; Suarez-Orduña et al., 2009).

1.3 Paragenesis and properties of barite and witherite

Barite, a mineral abundant in the Earth crust, arises from various geological processes. Primarily, barite formation occurs in environment such as hydrothermal veins, sedimentary layer or / and volcanic settings through the mixing of two fluids: one enriched with Ba leached from silicate minerals, and the other, typically an oxidized shallow fluid like seawater, containing sulfate. These fluids converge in areas of focused flow, leading to barite formation; therefore, barite can play a role in facilitating insights into the Earth crust past hydrogeological processes (Hanor, 2000). In addition, barite can originate through the alteration of preexisting other minerals primary deposits or as a gangue mineral in secondary formations, such as Lead-Zinc deposits in which barite can be present as an accessory mineral in the host rock or vein fillings within the ore body (Kolawole et al., 2019; Bulatovic, 2015). Furthermore, in marine environments, seawater generally lacks saturation with respect to barite. Consequently, most oceanic barite forms through fluid mixing, wherein one solution is enriched in barium and another solution is enriched in sulfate which results in supersaturation upon their convergence. This diverse formation spectrum renders barite geochemistry invaluable for paleoenvironmental, hydrogeological, and hydrothermal investigations (Griffith and Paytan, 2012).

Occurrences of witherite are mainly associated with the presence of barite such lead-zinc-barite deposits and sulfates / metal sulfide ores in relatively low temperature hydrothermal or supergene environments. This, therefore, leads to the suggestion that witherite is forming from barite under relatively low temperature conditions. Investigatory studies on barite and witherite origins indicate that at a temperature range (150°-70° C) witherite likely forms at the lower end of this temperature range subsequent to barite formation. The mechanism of witherite formation is believed to involve the alteration of barite by carbonated solutions. This process, documented in various studies, involves the recrystallization of barite into witherite through carbonate solutions (Weller et al., 1952; Helz and Holland, 1965; Baldasari and Speer, 1979;

Hazen, et al., 2013). Observations from geological studies on strontianite ($SrCO_3$) localities indicate the same phenomena as for witherite formation by suggesting a paragenetic sequence where witherite typically proceeds the formation of strontianite since witherite is found to form on barite and strontianite is found to from on witherite with the absence of celestite ($SrSO_4$), concluding a systematic alteration process from barite to witherite via carbonate rich solutions (Weller et al., 1952; Helz and Holland, 1965; Baldasari and Speer, 1979).

Characteristic properties and features of barite and witherite are given in Table 1.

Table 1. Properties and features of barite and witherite (Al-Awad and Al-Qasabi, 2001; Hanor, J. S., 2000; Deer, W. A., Howie, R. A., & Zussman, J., 2nd edition. 1992; Brown et al., 2019)

Mineral	Barite	Witherite
Chemical formula	$BaSO_4$ / (Ba,Sr)SO_4	$BaCO_3$
Composition	Barium sulfate, and often with trace amount of strontium	Barium carbonate
Color	Colorless (in thin section), white, yellow, red, brown, blue (many, which is possibly due to radiation exposure from incorporated radium), gray, multicolored or banded	Colorless (in thin section), white, greyish or light yellowish brown
Hardness	3.0 to 3.5	3.0 – 3.5
Crystal forms	Orthorhombic	Orthorhombic
density (g/cm^3)	4.48	4.29
Solubility (K_{sp}) at 25^0 C	$10^{-9.97}$	$10^{-8.56}$

The crystallographic structure of barite is orthorhombic, dipyramidal, and belongs to the space group Pnma. Within the structure, each sulfate tetrahedron consists of sulfur (S) and two oxygen (O) atoms lying on a mirror plane, while the other two oxygen atoms are equidistant above and below this plane (see Figure 1). The barium ions are also situated on this mirror plane and exhibit 12-fold coordination with oxygen atoms from seven different sulfate groups. (Griffith and Paytan, 2012; Hanor, 2000; Gaines et al., 1998).

The crystal structure of witherite, a member of the aragonite group, was initially elucidated by Bragg (1924) and is orthorhombic with the standard space group Pnam, where c < a < b. However, for convenience, the structure is often described in a non-standard orientation with a < c < b, resulting in space group Pmcn. In this orientation, the structure comprises alternating (001) layers of Ba cations and CO_3^{2-} anions (see Figure 1). These layers consist of two types of

carbonates (CO_3^{2-}) in layers (C1 and C2) alternating with two orientations of Ba cations (A and B) in a stacking sequence […AC1BC2…]. Each CO_3^{2-} anion is coordinated to 6 Ba atoms, while each Ba atom is coordinated to 9 oxygen atoms (Hazen, et al., 2013; Speer, 1983).

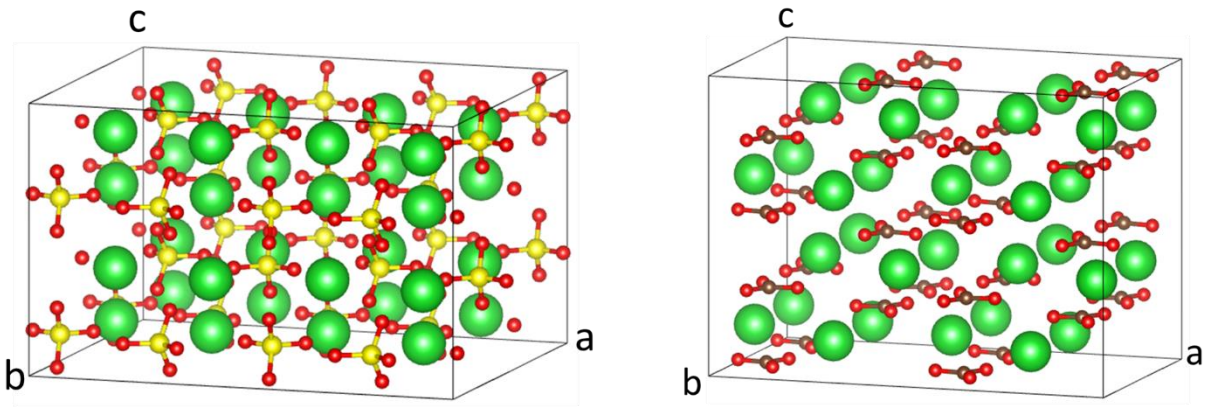

Figure 1 The left image shows the barite supercell (2x2x2) and the right image shows the witherite supercell (2x2x2). These visualizations illustrate the crystal structures of barite and witherite highlighting the differences in their structural arrangements. Green is barium, yellow is sulfur, brown is carbon and read is oxygen). Images generated using VESTA (Momma and Izumi, 2008).

1.4 Motivation and goal of the study

The recrystallization of barite into witherite, facilitated by carbonate-rich solutions, can be of significant relevance due to its implications for ^{226}Ra uptake. Studies such as Baldasari and Speer, 1979 bring forth the importance of understanding the fate of ^{226}Ra during this recrystallization process. Calculations carried out by Baldasari and Speer, 1979 show that under thermodynamic considerations, during conversion of Sr-contained barite into witherite, Sr would strongly partition into witherite. In addition, observations of natural samples by Baldasari and Speer, 1979, of barite containing Sr that was altered into witherite under equilibrium and disequilibrium conditions suggest that Sr preferentially partitions into witherite. Such observations also indicate that the most Sr-rich witherite is typically found as the early alteration products of Sr-bearing barites.

This natural process hints at the potential role that carbonate can play in influencing ^{226}Ra fate during the recrystallization of barite into witherite. As barite undergoes alteration via carbonate solutions, the incorporation of ^{226}Ra into the evolving witherite becomes a focal point of investigation. Understanding the mechanisms by which barite is converted into witherite and then the mechanism of ^{226}Ra partitioning between barite and witherite phases is crucial for elucidating the fate and distribution of ^{226}Ra in geological environments.

Through experimental and analytical approaches, this study aims to explore the fate of ^{226}Ra containing barite during the recrystallization process of barite in the presence of carbonate. By

the utilization of barite that was recrystallizing for long time in the presence of ^{226}Ra as well as barite that was freshly precipitated in the presence of ^{226}Ra along with carrying out experiments at different experimental conditions, the current study objective is to unravel the intricate interplay between carbonate induced ^{226}Ra contained barite alteration, witherite formation, and ^{226}Ra sequestration.

Several key aspects that are closely associated with the aforementioned objective are to be addressed as well:

How do the size-scale of the initial barite materials, different barite types and various experimental conditions influence the recrystallization process into witherite when ^{226}Ra is absent?

Since Sr incorporated barite recrystallization into Sr incorporated witherite can be an analogy that provides insights into Ra incorporated barite recrystallization into witherite and since previous studies were on observations of natural samples after the occurrence of the process or investigations on the process but with synthesized samples, the current study aims to answer the following: how does the recrystallization of natural, microscopic crystals and powders Sr-barite of into witherite influence the fate of Sr?

What insights do experiments on witherite precipitations in the presence of radium, particularly with varying Ra concentrations, provide into the partitioning behavior of radium and its consistency with theoretical expectations?

How can computational approaches, particularly density functional theory (DFT), be used to develop thermodynamic mixing models for radium-incorporated witherite compared to barite, and what predictions can be made about radium partitioning during the recrystallization process based on these models and experimental results?

The objectives and aspects that are covered in the current study research questions aim to deepen the understanding of the complexities of barite-witherite recrystallization and the behavior of ^{226}Ra within carbonate-rich environments. By integrating experimental, analytical, and computational approaches, this study seeks to provide a comprehensive understanding of the mechanisms and kinetics involved in the recrystallization process. The insights gained will enhance the state of knowledge of ^{226}Ra geochemistry, contribute to broader understanding of radium behavior in both natural and anthropogenic contexts. The study offers information on the predication ^{226}Ra in different settings, which can be implemented when considering protective strategies to mitigate ^{226}Ra impact on human and environmental health and safety. In addition to its contribution to the understanding of ^{226}Ra fate, the findings on barite

recrystallization into witherite will contribute to the broader field of mineral dissolution and precipitation, offering valuable comparisons between different sizes and types of barites starting materials and their behavior in carbonate solutions.

2 Physical and chemical aspects of dissolution and precipitation processes

2.1 Dependency of dissolution, precipitation and coupled dissolution-precipitation processes on changes of Gibbs free energy

When a mineral contacts an aqueous solution that is undersaturated with respect to the mineral, the dissolution process begins. This dissolution continues until the system reaches equilibrium, where the Gibbs free energy change (ΔG) equals zero. Equilibrium can be achieved through the dissolution and reprecipitation of the same mineral or the formation of a new secondary mineral phase if the solution contains foreign ions. These dissolution-precipitation (DP) processes drive recrystallization reactions between mineral phases and aqueous solutions in various geological systems such as sedimentary, diagenetic, metamorphic, and metasomatic environments (Forjanes et al., 2020; Putnis, 2009).

DP reactions are driven by the reduction of Gibbs free energy in response to changes in system parameters like temperature (T), pressure (P), mechanical stress, and local solution chemistry. The change in internal energy (ΔU) during DP reactions results from both thermal contributions (heat absorbed or released) and non-thermal contributions (mechanical work, surface work, chemical work, and strain work). The change in Gibbs free energy (ΔG) is related to the change in enthalpy (ΔH = ΔU + PΔV, where V is the system volume) and the system T times the change in entropy (ΔS) as follows (Benjamin, M. M., 2014):

$$\Delta G = \Delta U + P\Delta V - T\Delta S$$

Equation 1

When a mineral phase dissolves and another mineral forms via DP processes, the change in Gibbs free energy reflects the energy difference between the reactant and product phases. When considering stochiometric dissolution of pure barite (chosen here since it is the dissolving mineral in the current study), a reaction can be written as follows (Prieto, 2009):

$$BaSO_{4\,(s)} = Ba^{2+}{}_{(aq)} + SO_4^{2-}{}_{(aq)}$$

Equation 2

The equilibrium distribution between the species in Equation 2 can be written according to the law of mass action as follows (Prieto, 2009):

$$K_{BaSO_4} = \frac{[Ba^{2+}][SO_4^{2-}]}{a_{BaSO_4}}$$

Equation 3

where K_{BaSO_4} is the equilibrium constant that also known is the solubility product constant, the quantities between brackets denote the activities of the aqueous ions and a_{BaSO_4} represents the activity of barite solid phase. Since a_{BaSO_4} for a pure barite activity is equal to 1 for the standard conditions, meaning that K_{BaSO_4} is solely a function of the ion activities of the solution.

Now ΔG per mole for the reaction in Equation 2 can be written as follows (Prieto, 2009):

$$\Delta G_{BaSO_4} = \Delta G^{\circ}_{BaSO_4} + RT \ln K_{BaSO_4}$$

Equation 4

The term ΔG^{o} is the standard Gibbs free energy of the reaction under standard conditions, R is the gas constant (8.3143 J/mol·K) and T is the temperature (K). Upon the progress of Equation 2, ΔG will eventually be equal to zero, indicating the arrival to equilibrium. Therefore, Equation 4 can be written as follows: (Benjamin, M. M., 2014):

$$\Delta G^{\circ}_{BaSO_4} = - RT \ln K_{BaSO_4}$$

Equation 5

The significance of Equation 5 lies in the fact that ΔG^{o} is directly linked to K_{BaSO_4}, reflecting the amount of energy required under standard conditions to bring the system to an equilibrium state (see Figure 2).

By the substituting Equation 5 into Equation 4, replacement of $[Ba^{2+}]$ and $[SO_4^{2-}]$ with ionic activity product (IAP) and considering that the saturation index (Ω) is equal to $\frac{IAP}{K_{BaSO_4}}$, the following equation can be written (Prieto, 2009):

$$\Delta G_{BaSO_4} = RT \ln \Omega$$

Equation 6

This Equation *6* shows that ΔG reflects the energy the system is using or releasing as it moves toward the equilibrium state, depending on whether the system is undersaturated or supersaturated (see Figure 2).

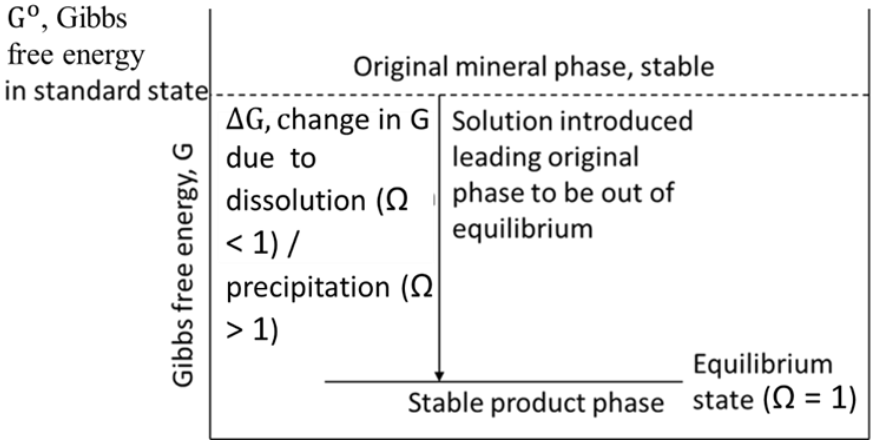

Figure 2. Schematic diagram showing free energy changes due to dissolution-precipitation process (adapted from White, 1997)

For the aforementioned free energy changes to occur, access to the reactive mineral surface by the aqueous solution is critical for the reaction progress. If the parent surfaces cannot fully contact the solution, the main driving force for the DP is absent, strongly inhibiting the reaction and potentially causing it to stop (Putnis, 2002). The extent of contact between the solution and parent mineral surfaces determines the nature of the DP processes that occur.

The DP processes can be either coupled or uncoupled; coupled dissolution-precipitation (CDP) processes occur when dissolution and precipitation happen close to each other spatially and temporally. In such cases, these processes are often termed "replacement processes," as the product phase preserves the shape of the parent phase, resulting in no major textural changes between the two mineral phases as will be addressed later.

In uncoupled processes dissolution-precipitation (UCDP), where there is no spatial or temporal closeness, the product phase does not preserve the shape of the parent phase, making the term "replacement" misleading. The term "recrystallization" is more general and can describe both coupled and uncoupled processes. However, "transformation" is a more precise term for describing uncoupled processes, as it clearly distinguishes them from coupled replacement processes without implying shape preservation (Gorski and Fantle, 2017). Therefore, throughout the present study the term “replacement” will be used for CDP, whereas the term “transformation” will be used UCDP and the term “recrystallization” will be will be used as a general term for changes in mineral phases due to external interactions for both CDP and UCDP as presented in Table 2.

Table 2. Terms that are used to describe the dissolution-precipitation processes throughout the present study

Term	Usage
Replacement	For coupled dissolution-precipitation processes (CDP) where the product phase preserves the parent phase shape.
Transformation	For uncoupled dissolution-precipitation processes (UCDP) where there is no preservation of the parent phase shape.
Recrystallization	For general description of chemical or structural change in the mineral due to external interactions, applicable to both CDP and UCDP processes.

2.2 Role of mass transfer in dissolution-precipitation processes

2.2.1 Replacement process as coupled dissolution-precipitation processes

A mineral replacement process primarily involves a solution/mineral interfacial layer within a reaction zone, which often is referred to as the reaction or replacement front (Ruiz-Agudo et al., 2014; Putnis, 2009). Throughout this study, the term replacement front (Figure 3) will be used for CDP reaction zone. In the replacement front, reactions between the solution and the parent phase induce the dissolution and, consequently, the interfacial layer becomes supersaturated with respect to the product mineral. This leads to the nucleation of the product phase to begin at the surfaces of the parent phase and that eventually results on a growth of product layer (Ruiz-Agudo et al., 2014).

There are two sources of interacting ions responsible for reactions at the replacement front: ion released into the interfacial layer from the dissolution of the parent phase, and dissolved ions delivered by the aqueous solution. The latter requires the creation and maintenance of transfer pathways in the product layer for product phase ions to continuously reach the replacement front, as schematically illustrated in Figure 3. The maintenance of these pathways is typically achieved through the generation of porosity in the product layer and/or the formation of fractures in both the parent and product phases (Putnis and Putnis, C. V., 2007; Altree-Williams et al., 2015).

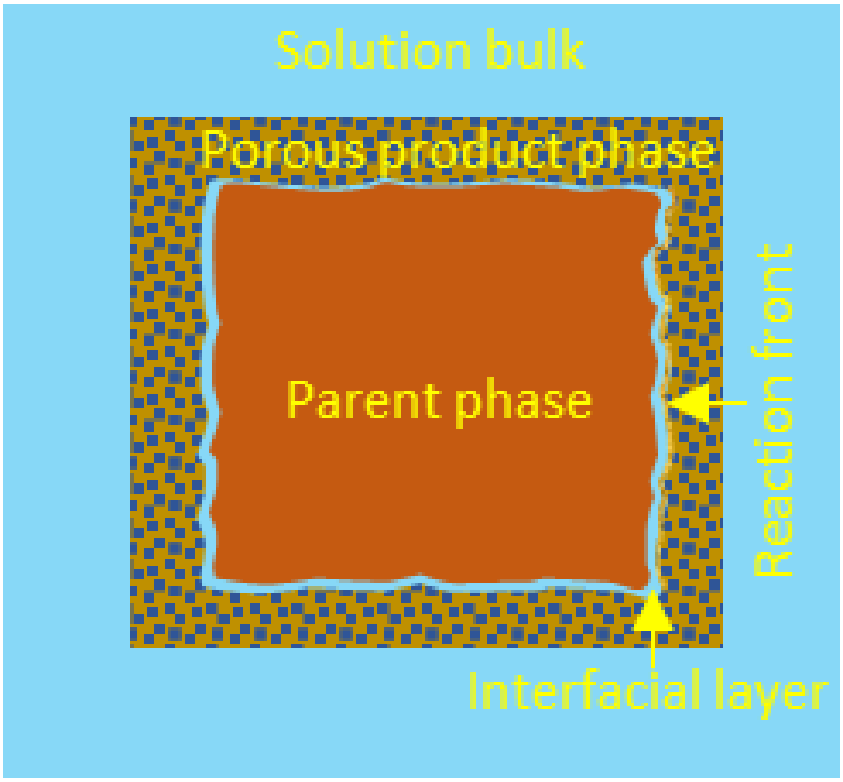

Figure 3. Schematic illustration of the parent phase, product phase with porosity, interfacial layer and replacement front in a solution bulk (adopted from Ruiz-Agudo et al., 2014).

2.2.2 Porosity generation during CDP to maintain reactions pathways

The generation of porosity during CDP replacement processes has been extensively observed in both experimental and natural systems. Putnis, A., & Putnis, C. V., 2007 documented porosity formation in KCl, orthoclase ($KaAlSi_3O_8$), and analcime ($NaAlSi_2O_6 \cdot H_2O$) as they replaced KBr, sodium feldspar (albite), and leucite ($KaAlSi_2O_6$), respectively. Similarly, Altree-Williams et al., 2015 observed porosity development in various phase replacements, including rutile and magnesite being replaced by titanite and dittmarite, respectively.

A crucial factor for porosity generation is the change in overall volume of the product phase due to differences in molar volumes and/or solubility between the parent and product phases. This molar volume difference effect occurs when the dissolved volume of the parent mineral exceeds the precipitated volume of the product mineral, as some dissolved material from the parent is lost to the solution (Putnis, A., 2009). As the product forms, it does not consume all ions lost from the parent mineral due to slow precipitations kinetics, and even if it would consume all ions a smaller molar volume of the product phase would still result in a smaller overall volume of product phase. Thus, to preserve the shape of the parent mineral, porosity must develop in the product phase.

As the parent mineral continues to dissolve and the product precipitates, the replacement front moves into the shrinking parent phase, leaving behind a thickening product phase with solution-filled pores. These pores are a necessary prerequisite for mass transport between the reaction front and the bulk solution. As long as the amount of precipitant is less than the amount dissolved, porosity is generated and pathways for mass transfer are maintained and replacement process can continue until the entire parent phase is replaced (see Figure 4). Solubility differences also play a significant role in losing ions to the solution and generating porosity, which is discussed in section 2.4.

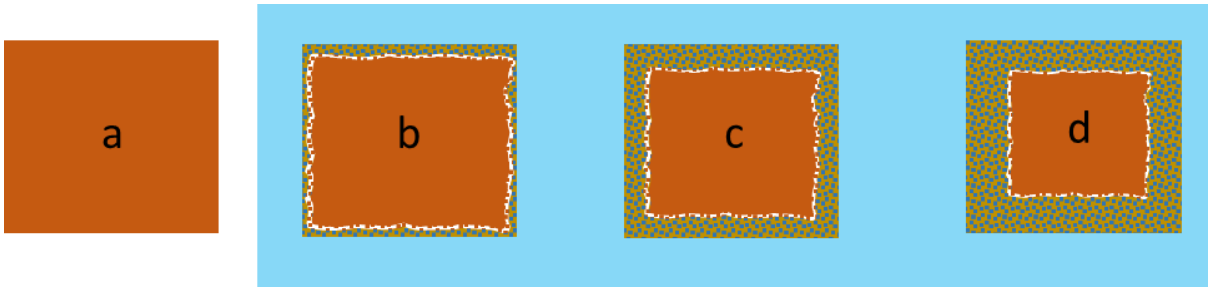

Figure 4. Schematic illustration of the pseudomorphic CDP reaction (adopted from Putnis, 2015). (a) is the parent phase prior to immersion into the solution, (b) reaction initiated by the solution: parent dissolves and product forms, (c) reaction carries on and porosity is being generated forming pathways from bulk solution to parent surfaces and (d) parent shrunk and product advanced preserving parent shape.

2.2.3 The role of crystallographic fit in the maintenance of CDP reactions

Porosity generation during the early stages of CDP processes can be influenced by the crystallographic fit between the parent and product phases. A perfect structural match can lead to the growth of a homogeneous layer on the parent substrate, fully covering it and preventing the solution from reaching the parent surfaces. This phenomenon, known as surface passivation, can halt the replacement process. Prieto et al., 2013 observed this effect when calcite and aragonite were replaced by $(Cd,Ca)CO_3$ solid solution, which has a structure similar to calcite. The resulting product formed a thin layer of tiny crystallites that quickly armored the parent calcite substrates, stopping further replacement as the solution could no longer contact the parent surfaces.

Conversely, porosity can develop when there is a structural mismatch between the parent and product phases. In such cases, the solution continues to access the parent reactive surfaces, allowing CDP reactions to proceed and generating porosity. For example, when aragonite is replaced by $(Cd,Ca)CO_3$, the lower structural match compared to calcite results in the formation of pore spaces on the parent substrates, facilitating continuous growth of the product and effective remediation of Cd from contaminated solutions (Prieto et al., 2003).

Another example is the replacement of leucite by analcime, reported by Altree-Williams et al., 2015. The lattice misfit in this system initially creates pore spaces in the leucite substrates, resulting in well-ordered pore networks that serve as migration routes for fresh solution from the bulk to the reaction front.

2.3 Epitaxy and pseudomorphism effects of replacement process

The effects described above are related to two crystallographic phenomena: epitaxy and pseudomorphism. Epitaxy occurs when there is a near-perfect crystallographic matching between the parent and product phases, leading to parent substrate armoring and surface passivation, as seen in the replacement of calcite by $(Cd,Ca)CO_3$. When the crystallographic match is sufficiently close but not exact, a single crystal of the parent can still be replaced by a single crystal of the product. This can be seen in the case where one feldspar is replaced by another, with only minor lattice mismatch (Putnis, 2015). In cases where there is no epitaxial relationship, CDP still proceeds, but the product phase will be polycrystalline, as observed in the replacement of calcite by apatite.

This lack of prefect crystallographic matching epitaxy can enhance product nucleation on the parent surface, increasing the parent dissolution rate and, consequently, the product growth rate. This can establish autocatalytic reactions, creating a feedback mechanism between dissolution and precipitation, and leading to nearly equal rates for both processes. This balance is why the term “coupled” is used for DP replacement processes. The near-equal rates of dissolution and precipitation result in the preservation of the parent volume and shape by the growing product phase, defining pseudomorphism (Putnis, 2015).

The pseudomorphic replacement mechanism depends on two key factors: the dissolution rate being the limiting step and a low nucleation activation energy barrier. If the nucleation rate is the limiting step, coupling effect highly likely can’t occur, leading to uncoupled processes.

Epitaxy effect and pseudomorphism effect are connected phenomena with epitaxy being a precursor to pseudomorphism. Putnis, 2009 suggests that structural similarity between the parent and product phases favors the crystallographic orientation of the parent by the growing product phase, reducing the interfacial energy at the replacement front. This energy reduction continues as long as nucleation occurs, maintaining the parent crystallographic orientation and preserving its overall shape. Based on anions and isotope analysis by Putnis, C. V. and Mezger, 2004 and in situ observations of solids and fluids at the interface by Putnis et al., 2005, Putnis, A., 2009 suggests that the solution composition at the interface is the most crucial factor in determining the coupling process and shape preservation. Putnis, 2009 further explains that

when the new product phase begins to form (nucleate) on the surface of the parent mineral, it does so within a specific area in the surrounding solution, known as the "diffusion profile." This profile is a zone where the concentration of elements dissolved from the parent mineral changes gradually. Because the product phase forms within this zone, it can naturally follow the shape and structure of the parent mineral. This allows the new mineral phase to "inherit" or mimic the external shape of the parent mineral, maintaining the overall appearance of the original mineral even though the material is different.

2.4 Solubility role and interfacial layer dynamics in coupled dissolution-precipitation reactions

The solubility of parent and product phases is a critical factor affecting the formation of the product, as it determines supersaturation in the interfacial layer. Achieving the supersaturation threshold required for product formation necessitates only a monolayer of parent dissolution, regardless of the crystallographic relationships between the parent and product phases (Putnis, 2002). Various studies have highlighted the role of solubility in replacement processes, such as the topotaxial replacement of celestite by strontianite (Pina, 2019) and the formation of calcite and aragonite through the replacement of anhydrite and gypsum, respectively (González-Illanes et al., 2017).

The solubility plays a role by influencing the amount generated by parent dissolution and the amount consumed by product precipitation. Consequently, porosity can still form even when the product molar volume is larger than the parent, as seen in the replacement of leucite by analcime (see 2.2.3).

To illustrate solubility role in CDP reactions, Putnis, 2002 used the KCl-NaCl-H_2O system from Silcock 1979 experimental solubility study. In the solubility diagram (Figure 5), points represent solution compositions saturated with respect to either end-member. When one phase contacts a solid of the other, the solution becomes undersaturated with the contacted solid, causing it to dissolve and supersaturated with the other, leading to precipitation. The system reaches equilibrium at point E (the eutonic point). For instance, a solution saturated with KCl at point A contacting NaCl will dissolve NaCl and precipitate KCl until NaCl is completely dissolved or equilibrium is reached.

The slope of the saturated line in Figure 5 indicates whether more material from the dissolved NaCl is lost to the solution than precipitated as KCl. A slope > -1 suggests fewer moles KCl precipitated compared to NaCl dissolved, resulting in a molar deficit in the product phase, which must be compensated by porosity. Thus, if dissolution due to solubility exceeds what is

needed for precipitation, porosity forms regardless of relative molar volumes. Conversely, a slope < -1 and a larger product molar volume than the parent implies a molar excess in the product, potentially forming an armor layer that halts the replacement reaction. This stoppage can be understood as another type of passivation effect, alongside the perfect structural matching between parent and product phases discussed earlier.

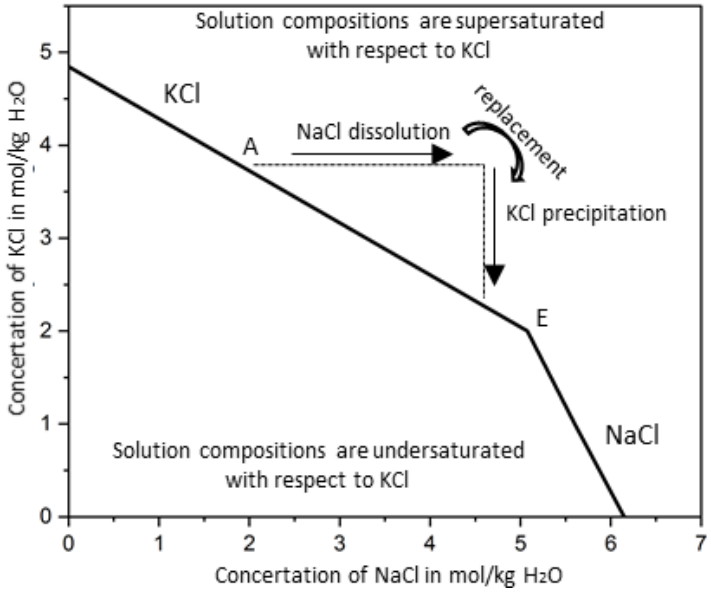

Figure 5. KCl-NaCl-H_2O solubility diagram to illustrate the effect of solubility on the dissolution of NaCl and the precipitation of KCl upon contacting an NaCl crystal with a solution that is saturated with respect to KCl until a global equilibrium with the two solid phases is achieved (reproduced from Putnis, 2002).

In CDP processes, relative solubility, rather than absolute solubility, is key since reactions occur in the interfacial layer between the two solid phases (Putnis, 2002). Even limited parent dissolution can supersaturate the interfacial layer with respect to the product phase.

Ruiz-Agudo et al., 2014 stated that new mineral assemblages form even when the bulk solution is undersaturated with respect to the new phase, inferred from AFM experiments showing new phase formation under such conditions. This undersaturation is attributed to the interfacial layer distinct thermodynamic and thermodynamic physical properties, such as diffusion rate, viscosity, solute adsorption, dielectric constant, and pH, differing from the bulk solution. These properties aid in achieving supersaturation within the interfacial layer when the parent surface dissolves.

Putnis, C. V., et al., 2005 confirmed this interfacial supersaturation using real-time phase-shift interferometry to observe compositional gradient changes on a KBr crystal surface reacting with saturated KCl solution. The technique showed refractive index changes (related to concentration gradients) at the crystal surface, indicating CDP reactions initiated by a high solution concentration gradient created by KBr dissolution, enriching the interface layer with

K^+ and Br^-. This demonstrates that the interfacial layer accumulates dissolved materials from the parent faster than diffusion to the bulk solution, allowing precipitation even when the bulk solution is undersaturated.

Hövelmann et al. 2012 provided another example for the role of interfacial dissolution in CDP through AFM investigation of CO_2 sequestration during brucite ($Mg(OH)_2$) dissolution. They suggested that both dissolution and precipitation of a new Mg-carbonate phase (likely dypingite) are parent surface-controlled, as nucleating particles were more abundant at lower pH levels (4-5) compared to higher levels (7.20-9.30). Areas of enhanced dissolution supported more Mg-carbonate nucleating particles, indicating local Mg^{2+} contributions from dissolved brucite controlled the reaction. Similar to Putnis, C. V., et al. (2005), Hövelmann et al. (2012) proposed a Mg^{2+} build-up in the interfacial layer, if brucite dissolution outpaces Mg^{2+} diffusion to the bulk solution. This creates a concentration gradient near the brucite surface, enabling local supersaturation and Mg-carbonate nucleation.

Rendon-Angeles et al., 2000 studied fluorapatite ($Ca_5(PO_4)_3F$) replacing hydroxyapatite ($Ca_5(PO_4)_3(OH)$) that has low solubility, highlighting how minimal dissolution can drive CDP. They proposed that dissolved OH^- ions were consumed by precipitating fluorapatite almost immediately, preserving the hydroxyapatite crystal morphology. This indicates that the dissolved OH^- from hydroxyapatite was sufficient to create a concentration gradient in the interfacial layer, enabling fluorapatite precipitation.

3 Solid solution mixing

Solid solutions are minerals with substitutional impurities in their structures (Prieto et al., 2013). They form by the simultaneous crystallization of two solutes with similar crystal structures from an aqueous solution (Prieto, 2009). The formation of solid solutions and the related solid-solution-aqueous solution (SSAS) mixing processes are common in natural environments and industrial systems due to the frequent occurrence of the necessary physiochemical conditions for such crystallization or recrystallization reactions.

As discussed earlier in the section on dissolution–precipitation processes, the presence of an ion in an aqueous solution can lead to the crystallization of a phase in which that ion is incorporated into the solid phase structure. When a multi-ion aqueous solution interacts with a mineral via a dissolution-precipitation process, a nonstoichiometric multicompositional phase is expected to form—this is a solid solution. Additionally, solid solutions can also form when water contacts preexisting multicompositional mineral phases, and dissolution-precipitation

processes occur, potentially resulting in a new equilibrium distribution of ions between the solid and aqueous phases.

However, the formation and stability of solid solutions are highly dependent on the miscibility of the involved solids—how well the different ions can substitute for each other in equivalent structural positions within the solid's crystal lattice. The degree of miscibility influences whether a homogeneous solid solution will form or if phase separation will occur, leading to the formation of distinct mineral phases.

These aspects have led environmental geochemists to consider solid solutions as potential remediation options for incorporating harmful metals, such as radionuclides and inorganic contaminants, into various aquatic environments. However, the effectiveness of such remediation strategies depends on thermodynamic and mechanistic factors, including the miscibility of the solids and the specific conditions under which solid solution incorporation occurs (Prieto et al., 2013).

Since the incorporation of Ra into witherite is in the focus of the present study, a $(Ba_{1-x}\ Ra_x)CO_3$ binary solid solution will be used as example to describe law-of-mass-action equations that relate the composition of aqueous and solid phases, as follows (Prieto, 2009; Glynn, 2000):

$$[Ba^{2+}]\,[CO_3^{2-}] = K_{wrt}\ a_{wrt} = K_{wrt}\ \lambda_{wrt}\ \chi_{wrt}$$

Equation 7

$$[Ra^{2+}]\,[CO_3^{2-}] = K_{RaCO_3}\ a_{RaCO_3} = K_{RaCO_3}\ \lambda_{RaCO_3}\ \chi_{RaCO_3}$$

Equation 8

where $[Ba^{2+}]$, $[CO_3^{2-}]$, $[Ra^{2+}]$ are the aqueous activities of Ba^{2+}, CO_3^{2-} and Ra^{2+}, respectively; K_{wrt} and K_{RaCO_3} are the solubility products of the two end member phases; a_{wrt}, a_{RaCO_3}, λ_{wrt} λ_{RaCO_3}, χ_{wrt} and χ_{RaCO_3} are solid phase activities, activity coefficients and mole fractions of the two end member phases, respectively. The two end members' mole fractions are related as follows:

$$\chi_{RaCO_3} = 1 - \chi_{wrt}$$

Equation 9

The aqueous Ra activity being in equilibrium with a $(Ba_{1-x}\ Ra_x)CO_3$ solid solution requires a simultaneous fulfillment of the two mass-action equations. Therefore, the combination of the two mass-action equations is beneficial to construct phase diagrams that depict different equilibrium states for Ra solution and Ra witherite (Prieto, M., 2009; Glynn, P., 2014). Such a

combination is usually formulated in analogy to Lippmann's binary liquid-vapor systems (Lippmann F., 1977, 1980, 1982), and it yields a relation knows as the solidus equation (Prieto, 2009; Glynn, 2000:

$$\Sigma\Pi_{eq} = \mathrm{K_{sp,\ wrt}}\,\lambda_{\mathrm{wrt}}\,\chi_{\mathrm{wrt}} + \mathrm{K_{sp,\ RaCO_3}}\,\lambda_{\mathrm{RaCO_3}}\,\chi_{\mathrm{RaCO_3}}$$

Equation 10

where $\Sigma\Pi_{eq}$ is the value of total solubility product expressed as a function of the solid phase composition.

For a complete description of the aqueous solution and Ra witherite equilibrium, the total solubility should also be expressed as function of the aqueous solution composition, and such expression is derived from Equation 7 and Equation 8 (Lippmann, F., 1977, 1980, 1982) that yields a relation known as the solutus equation (Prieto, 2009; Glynn, 2000:

$$\Sigma\Pi_{eq} = 1/\left(\frac{\chi_{Ba,aq}}{\mathrm{K_{sp,\ wrt}}\,\lambda_{\mathrm{wrt}}} + \frac{\chi_{Ra,aq}}{\mathrm{K_{sp,\ RaCO_3}}\,\lambda_{\mathrm{RaCO_3}}}\right)$$

Equation 11

where $\chi_{Ba,aq}$ and $\chi_{Ra,aq}$ are the aqueous activity fraction of the substituting ions at the thermodynamic equilibrium and can be defned as follows:

$$\chi_{Ba,aq} = \mathrm{Ba^{2+}}/\left(\mathrm{Ba^{2+}} + \mathrm{Ra^{2+}}\right)$$

Equation 12

$$\chi_{Ra,aq} = \mathrm{Ra^{2+}}/\left(\mathrm{Ba^{2+}} + \mathrm{Ra^{2+}}\right)$$

Equation 13

To measure the partitioning of Ra between the witherite and the solution phases, the mixing properties of Ra witherite need to be investigated. One important concept is the free energy of mixing (ΔG_M), which is the difference between the free energy of the solid solution (Ra-witherite) and those of a hypothetical compositionally-equivalent mechanical mixture of the two end members witherite and $\mathrm{RaCO_3}$. Such energy differences reveal whether Ra witherite is an ideal or non-ideal mixture, which is directly related to Ra partitioning between the aqueous and the solid phase. The ΔG_M is related to another concept that is the excess free energy of mix (ΔG_E) as follows (Prieto, 2009):

$$\Delta G_E = \Delta G_M - \Delta G_{M,id}$$

Equation 14

where $\Delta G_{M,id}$ is the free energy mixing for the ideal solid solution.

Therefore, the concept of excess free energy of mixing (ΔG_E) is used to evaluate the ideality or non-ideality of the solid solution and can be subdivided into an excess enthalpy term (ΔH_E) and an excess entropy term (ΔS_E) at a given temperature as follows (Prieto, 2009):

$$\Delta G_E = \Delta H_E - T\Delta S_E$$

Equation 15

Excess enthalpy primarily determines whether a solid solution is ideal or non-ideal. It reflects the interactions between dissimilar cations—such as Ra and Ba in the present study—within the crystal structure, and accounts for effects like lattice strain and other energetic contributions (Prieto, 2009). Given the small difference in the ionic radii of Ba and Ra (1.47 Å and 1.54 Å, respectively (Yoshida et al., 2014)), the strain introduced into the lattice by substitution is minimal, leading to a relatively small excess enthalpy contribution. This suggests that the Ra witherite solid solution is slightly non-ideal, but the degree of non-ideality is expected to be small, as the atomic radius difference is only about 5%.

Excess entropy, on the other hand, refers to contributions beyond the ideal entropy of mixing, such as when specific ions, like Ra and Ba, show a preference for certain lattice positions or induce some degree of ordering within the witherite crystal structure (Prieto, 2009). However, this ordering does not relate to lattice strain, which, as noted, is an enthalpy-driven factor.

The simplest type of non-ideal solid solution is the regular solid solution (Prieto, 2009), and ΔG_E can be expressed with one dimensionless fitting parameter known as Guggenheim parameter (a_0) (Guggenheim, 1937): (Glynn, 2000:

$$\Delta G_E = \chi_{\mathrm{wrt}}\, \chi_{\mathrm{RaCO_3}} \mathrm{RT} a_0$$

Equation 16

In many cases such a simple model is sufficient to quantify the non-ideality of solid solutions. Since the non-ideality of the solid solution is a deviation from the ideal state, activity coefficients can be introduced to Equation 16 to account for such deviation (Redlich and Kister 1948; Plummer, L. N., & Busenberg, E., 1982). This can be done via introducing chemical potential (μ_i) expression as follows (Prieto, 2009):

$$\mu_i = \mu_i^{\mathrm{o}} + \mathrm{RT} \ln a_i$$

Equation 17

where μ_i^{o} is the standard chemical potential and a_i is the activity a component i. For a non-ideal solution, the activity $a_i$can be related to the mole fraction χ_{i} and the activity coefficient λ_{i} :

$$a_i = \lambda_i \ \chi_i$$

Equation 18

Substituting the expression for the activity into the chemical potential gives:

$$\mu_i = \mu_i^o + RT \ln \lambda_i \ \chi_i$$

Equation 19

This expression shows that the chemical potential depends on the non-ideality of the system, as reflected in the activity coefficients λ_i (Redlich, O., & Kister, A. T., 1948; Plummer, L. N., & Busenberg, E., 1982). In the context of the regular solution model, the activity coefficients can be derived from the excess Gibbs free energy (Prieto, 2009):

$$\lambda_{wrt} = \exp\left(\chi^2_{RaCO_3} a_0\right)$$

Equation 20

$$\lambda_{RaCO_3} = \exp\left(\chi^2_{wrt} \ a_0\right)$$

Equation 21

Since measuring the partitioning is of importance in the SSAS systems, geochemists suggested describing it in terms of a partition coefficient, D, (Renderson and Kracek 1928), which is defined as follows (Shtukenberg et al., 2006; Prieto, 2009):

$$D = \frac{\chi_{RaCO_3} / \chi_{wrt}}{[Ra^{2+}]/[Ba^{2+}]}$$

Equation 22

D > 1 indicates that Ra is preferentially partitioning towards the solid phase and the contrary is true for D < 1. It is worth noting that the tendency of Ra to incorporate into witherite is not merely based on thermodynamics, but kinetics may play a role as well. Therefore, factors such the aqueous solution supersaturation state and solid phase growth rate may affect the partitioning processes.

At thermodynamic equilibrium and by substituting Equation 7 and Equation 8 into Equation 22, an expression for D at equilibrium in terms of the two end member's solubilities can be derived to as follows (Heberling et al., F., 2018):

$$D = \frac{K_{sp,\ wrt} \lambda_{wrt}}{K_{sp,\ RaCO_3} \lambda_{RaCO_3}}$$

Equation 23

For a regular solid solution and to link the equilibrium partition coefficient with the non-ideality parameter (a_0) of the solid solution, the activity coefficients in Equation 23 can be

replaced with Equation 20 and Equation 21, which can then be algebraically solved considering $\chi_{\mathrm{wrt}} = 1 - \chi_{\mathrm{RaCO_3}}$ and considering the dilute limit in which $\chi_{\mathrm{RaCO_3}}$ is close to zero to obtain the following relation (Brandt et al., 2015; Heberling et al.,2018):

$$D_{regualr} = \frac{\mathrm{K_{sp,\ wrt}}}{\mathrm{K_{sp,\ RaCO_3}}} \exp(-a_0)$$

Equation 24

4 Analytical methods

X-ray Diffraction

X-ray diffraction (XRD) is a primary technique for determining the composition and crystalline structure of mineral samples. In XRD, a sample is illuminated by an X-ray beam. The scattering of the X-ray beam by the sample is influenced by the spacing between the atoms in the crystal lattice, which is similar to the wavelength of the X-rays.

As X-rays travel through the sample, they are scattered by the electrons, changing direction based on the electron density distribution in the crystal, which shows regular oscillations along the spacing between the crystal lattice planes. This scattering can result in constructive or destructive interference, depending on the path length differences of the scattered beams. Constructive interference leads to amplified scattered X-ray intensities at specific angles, which can be described by Bragg's law:

$$n\lambda = 2d \sin\theta$$

Equation 25

where n is an integer, λ is the X-ray wavelength, d is the distance between lattice planes, and θ is the diffraction angle (see Figure 6).

The resulting diffraction peaks, measured at specific angles, provide information about the crystal lattice. The characteristic distances between lattice planes can identify mineral phases or determine the composition of a mixture of crystalline materials by comparing the peak patterns to known crystal structure databases (Bunaciu et al., 2015).

The intensity of diffraction peaks relates to the electron density distribution within the crystal unit cell, allowing to infer the atomic structure. Additionally, peak widths provide information about crystallite sizes: sharper peaks indicate larger crystallites, while broader peaks suggest smaller ones.

An X-ray diffractometer consists of three primary components: an X-ray tube, a sample holder, and an X-ray detector. X-rays are generated in a cathode ray tube by heating a filament to emit

electrons, which are accelerated towards a target material, producing characteristic X-ray spectra, including K_α and K_β lines. Copper is commonly used as the target material, generating CuKa radiation at 1.5418 Å.

X-rays are collimated and filtered to achieve monochromatic radiation. During diffraction, the sample rotates at an angle (θ) in the X-ray beam path, while the detector rotates at 2θ to collect diffracted X-rays. Constructive interference, satisfying Bragg's law, results in intensity peaks recorded by the detector. Typical powder diffraction patterns are collected over a 2θ angular range from 5° to 70° (Connolly, 2007; Bunaciu et al., 2015).

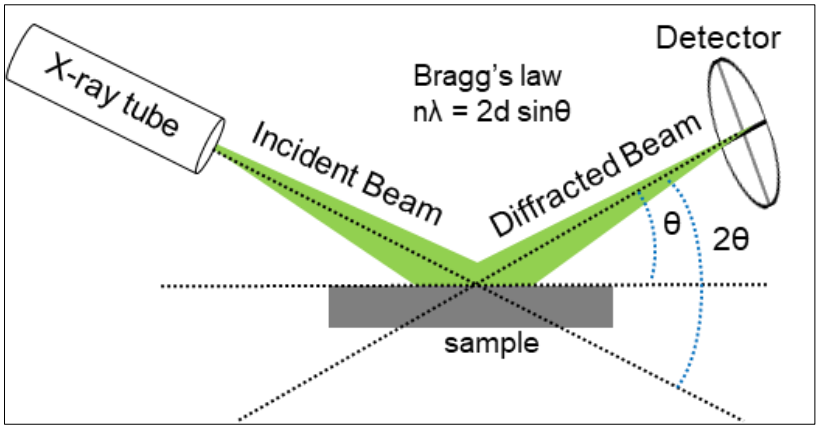

Figure 6: schematic representation of main XRD components (adopted from Bunaciu et al., 2015)

Scanning electron microscope

Scanning electron microscope (SEM) is an electron based analytical technique, where electrons are emitted as a beam from a so-called electron gun and then narrowed to a dimeter of about 0.4-5 nm, defining the maximum resolution of the images. The beam narrowing is carried out via the use of one or two condenser lenses. Rectangular images are obtained by scanning the beam in a raster fashion over the sample. The scanning motion is achieved by passing the electron beam through a pair of deflection coils, deflecting the beam in x and y direction before it reaches and interacts with the sample. When the electron beam reaches the sample, it undergoes various interactions with the sample material and loses energy through scattering and absorption by the sample (Goldstein 2017; Mohammed and Abdullah, 2018).

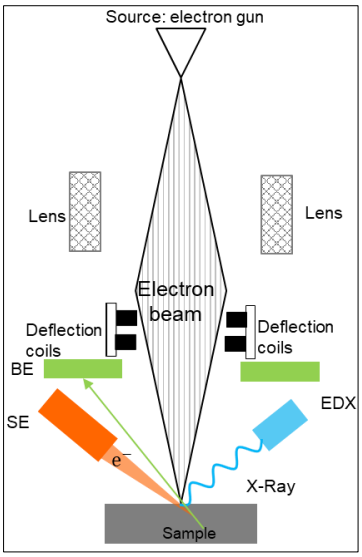

Figure 7: schematic representation of main SEM working principles (modified from Mohammed and Abdullah , 2018)

The different interactions with the sample atoms result in various signals such as secondary electrons (SE), back-scattered electrons (BE) and the fluorescent x-ray, which may be analyzed in an energy dispersive x-ray detector (EDX). The source of SE signals is the low energy electrons that are ejected from the sample atoms conduction band due to the inelastic scattering by the electron beam. The information depth of SE is 5~50 nm and mostly used to obtain topographic information about the analyzed sample surface. The signal from elastically scattered electrons termed backscattered electrons, BE. The denser the sample material, the more electrons in the sample atoms (high Z materials), the larger the elastic scattering interactions and thus, the higher the intensity in the BE image. Therefore, BE is a first qualitative way to obtain information about the distribution of heavy elements in a sample. The BE information depth is 450 nm, therefore, it can reveal elemental information buried beneath the sample surface. The EDX detector analyses characteristic x-rays that are emitted upon the interactions of the electron beam with the sample atoms. It provides information on the elemental composition of the sample. Signals may be quantified to obtain the concentration and distribution of elements in the sample. EDX information depth is about 2 µm, which makes it rather a bulk method compared to SE or BS (Mohammed and Abdullah, 2018).

The samples can be internally investigated further when a SEM is equipped with Focused Ion Beam (FIB) cutting device. FIB-SEM is a technology developed based on SEM technology with an ion beam added to preform cutting. The fundamental work principle of a FIB is a direct effect to the sample surface via removing ultra-thin layers from the sample surface to reveal interior structures. The fact that FIB can be combined with SEM makes FIB-SEM a powerful

tool that allows for instantaneous SEM images to be produced as the sample surface being cut via FIB. The combined FIB-SEM allows for precise imaging with nanometer resolution and simultaneous chemical analysis (J. Weber at el., 2017).

The samples can be internally investigated further using a Scanning Electron Microscope equipped with a Focused Ion Beam (FIB) cutting device (see Figure 8). FIB-SEM is an advanced technology that builds upon traditional SEM technology, where the electron beam is replaced with a highly focused beam of ions. The fundamental working principle of a FIB involves the direct interaction with the sample surface, where ultra-thin layers are sequentially removed to expose and analyze the interior microstructures of the sample. This ion milling process allows for precise sectioning at nanoscale resolutions, revealing detailed structural information that is not accessible through conventional methods (Weber at el., 2017).

The integration of FIB with SEM enhances its capabilities, enabling real-time imaging of the sample surface as it is being milled. This combination provides a powerful analytical tool, allowing for immediate SEM imaging of the freshly exposed surface, which is critical for maintaining the integrity of the sample during the analysis process. The FIB-SEM system thus facilitates high-resolution imaging with nanometer-scale resolution and allows for simultaneous chemical characterization through techniques such as EDX. One of the significant advantages of FIB-SEM is its ability to create cross-sectional images and 3D reconstructions of the sample, providing insights into the internal morphology and composition at sub-micron to nanoscale levels. This capability is particularly valuable for studying the microstructure of materials, the distribution of elements within complex composites, and the detailed examination of defects, inclusions, and phase boundaries (Weber at el., 2016; Weber at el., 2017).

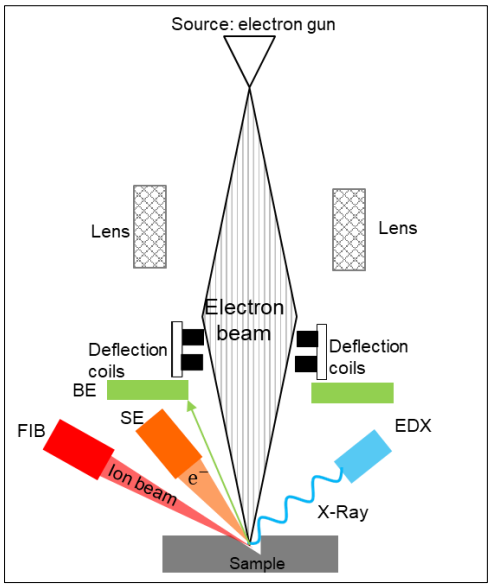

Figure 8: FIB-SEM components illustrating working principle of the two combined technologies (modified from Mohammed and Abdullah, 2018)

Raman microscope

The Raman microscope (RM) is a useful technique to analyze the crystal structures or certain aspects of the chemical composition of a sample. The RM technique is based on sending laser light to the sample, which will result in elastic (Rayleigh) scattering with the same wavelength as the incident light and inelastic (Raman) scattering with different wavelengths due to the interactions of the laser light with molecular vibrational modes and crystal phonons leading to various vibrational bands (Efremov et al 2008; Rostron et al., 2016).

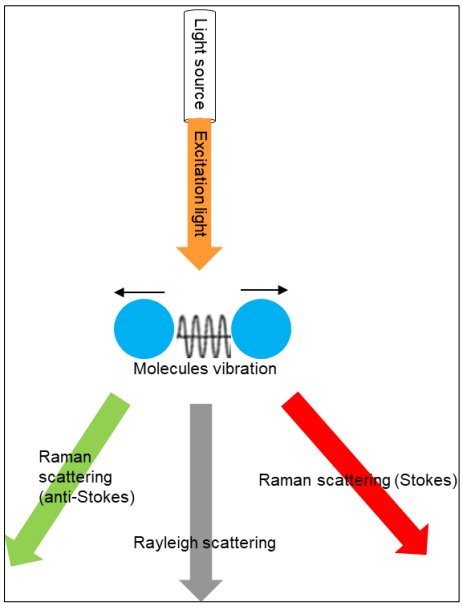

Figure 9: Molecular vibrations and Raman scattering (modified from Das and Agrawal, 2011)

The Raman spectra can be obtained when the scattered light is analyzed by a spectrometer, which allows to determine the Raman shift that is the wavelength difference between the

incident light and the scattered light. There are two types of Raman shifts: shifts to higher wavelengths than the incident light from constructive interference between the laser light and the vibrational modes, known as Stokes scattering, and shifts to lower wavelengths, from destructive interference, known as anti-Stokes scattering. Typically Stokes scattering is used for the analysis (Das and Agrawal, 2011).

Gamma Spectroscopy

The Gamma Spectroscopy (GS) is a radioanalytical technique that is used to determine the radioactivity of a sample and to identify contained radionuclides via measuring the electromagnetic gamma rays (Ahmed, 2021). The GS detection systems are built to convert gamma-rays to electrons or visible photons inside the detector material with a reasonable cross section in order to enable efficient measurements. The denser the matter, the more gamma rays will be absorbed (or scattered) and the more electrons or photons are excited, therefore, density is the main characteristic determining how many gamma-photons are interacting with the matter. Different materials can be used for detectors such as sodium iodide (as an example for a scintillation detector / photon excitation) or high purity germanium (as an example for a semiconducting detector / electron excitation) (Alexiev et al., 2002).

The interactions of gamma-photons with the detector lead to the following effects: Photoelectric effect, Compton effect and Pair production. The photoelectric effect is a low energy process where an electron absorbs all the energy of an incident gamma-ray, gets ejected and detected to produce a single gamma peak with an energy correlated with the incident gamma-ray energy. The Compton effect is a medium energy process where an incident gamma-photon is partially absorbed by an electron and scattered with lower energy. Since there are different scattering angles, this leads to different energy absorption and different energy depositions in the detector resulting in a signal termed Compton continuum. The Pair Production is a high energy process where the interaction of a gamma-photon at high energy produces an electron / positron pair resulting in a single peak if captured by the detector or in double escape peaks if escaping the detector (Knoll, 2010).

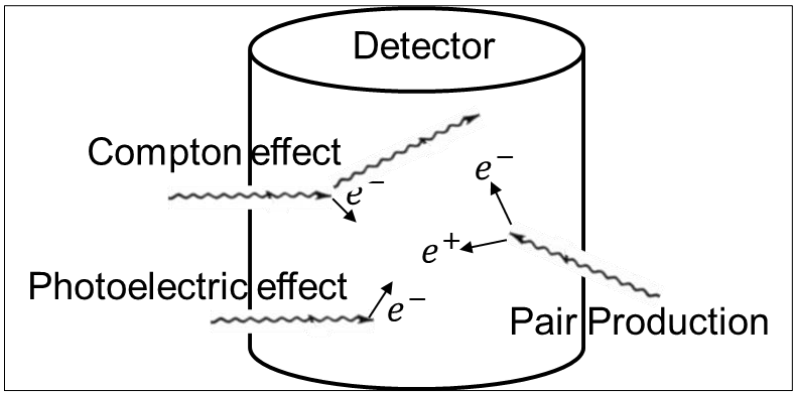

Figure 10: A simplified illustration of a gamma detection system (adopted from Knoll, 2010)

Inductively coupled plasma - optical emission spectrometry

Inductively coupled plasma-optical emission spectrometry (ICP-OES) is a technique for analyzing aqueous ions that is widely used. With ICP-OES the concentration of various elements in a sample can be determined via the use of the emissions of the atoms and ions that are excited in the plasma (Hou and Jones, 2000). The analysis is carried out by nebulizing the solution to produce an aerosol that is introduced to an argon plasma leading to the excitation of atoms to ions and electrons via the plasma energy. After excitation electrons return to the ground state, and emit light during the deexcitation process. A spectrometer is used for the identification of the elemental emission lines that is characteristic for every element. The element concentration is obtained via the intensity of the emission lines, after calibration, by measuring standards with defined concentration (Douvris et al., 2023).

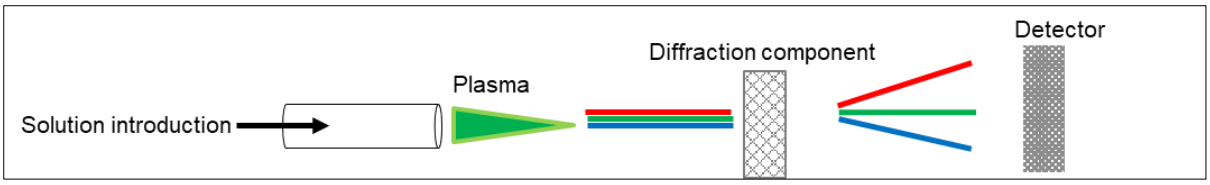

Figure 11: Conceptual illustration for the ICP-OES working principle (modified from Douvris et al., 2023)

Atomic Force Microscope

Atomic Force Microscopy (AFM) is a powerful technique to measure the topography of a sample surface at the nanoscale. The advantageous aspect of AFM is the use of a physical probe to determine the surface features of samples in contrast to light based microscopes, which are restricted to microscale resolution levels, due to wavelength constraints.

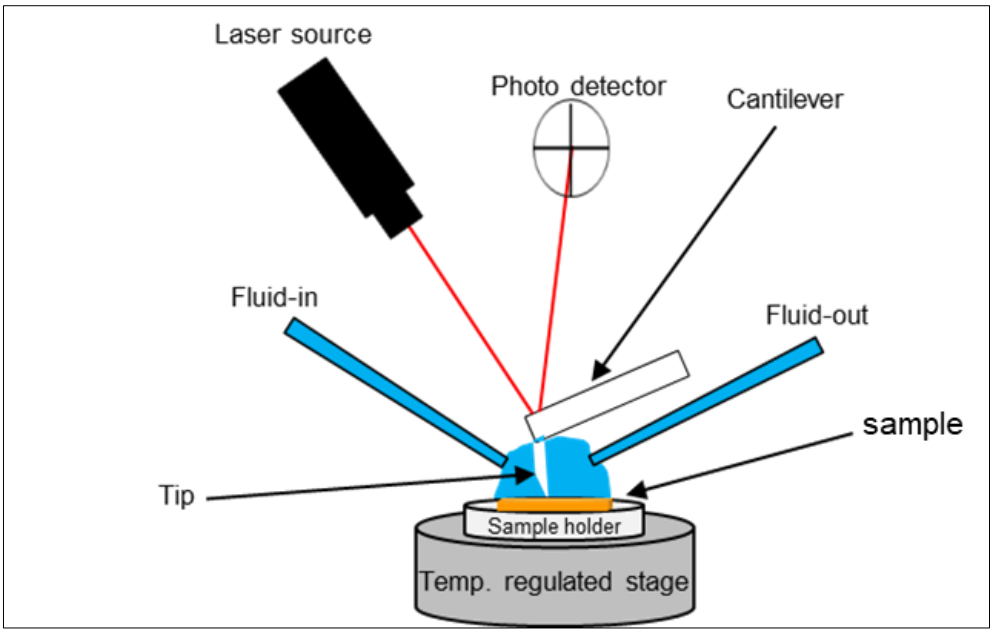

Figure 12: Schematic depiction for AFM working principle (adopted from Jagtap and Ambre, 2006)

The principle operational concept of AFM is that a rather sharp nano-tip is attached to a small cantilever and that tip is used to scan surfaces in a raster fashion with dominantly two operations modes: contact mode and tapping mode. The tip in contact mode is pressed to the surface with a constant force, which causes the cantilever to bend. Surface topographical features, cause changes in cantilever bend, which are detected in a split photodetector via a laser that is reflected from the back of the cantilever. The sample stage, mounted on a piezo crystal, compensates the cantilever bend, and from the required motion of the piezo crystal a display of the surface topographical features is produced (height image). In tapping mode, the tip is not pressed onto the sample surface constantly, but the cantilever is oscillating at its resonance frequency. Thus, its contact with the surface is limited to preserve both the tip and the surface. The cantilever is oscillating at a certain amplitude while raster scanning the surface as in contact mode. The oscillation amplitude is affected by the distance to the surface features, a feedback loop between the photodetector and the height piezo, aiming to keep the cantilever oscillation amplitude constant, is used to detect height changes in the same fashion as in contact mode (amplitude modulation tapping mode) (Jagtap, R. N., & Ambre, A. H., 2006).

5 Experimental details

The experimental procedures of the study are detailed below. Towards the end of chapter 5 a complete overview of all experiments is provided in Table 3 and Table 4.

5.1 Initial solid materials

5.1.1 Barite used for experiments in the absence of ^{226}Ra: cubes and powders

The initial materials were two natural barite crystals obtained from the Androvo mine, Bulgaria (AR) and from Iberg hill, Western Harz Mountains, Germany (IB). Both types were analyzed with X-ray photoelectron spectrometry (XPS, ULVAC-PHI, model VersaProbe II) for the purity of barite. Crystals from both natural types were cut into cubes with ~ 3x3x3 mm. Following the cutting process, the cubes were fine-ground with 1200-grit sandpaper to achieve a smooth surface finish. The cubes were washed in ethanol (Merck Emsure, absolute, for analysis) and MilliQ water (18.20 MΩ cm) in an ultrasonic bath for few minutes and dried in room temperature.

The initial powder materials were four types: a freshly precipitated barite (P), Sachtleben barite (SL), as well as AR and IB. The P barite was prepared by the quick addition of $BaCl_2$ (Alfa Aesar, anhydrous, 99,998% (metal basis)) to Na_2SO_4 (Merck Suprapur, anhydrous, 99.99%) while stirring at 25°. The precipitate was filtered, washed with MilliQ water multiple times and dried at room temperature. The SL was a commercial synthetic high purity powder (XR-HR10) from Sachtleben Chemie GmbH, previously used by Curti et al., 2010, Klinkenberg et al., 2014, Brandt at al 2015 and Heberling et al., 2018. In addition, an SL type that was a long time treated (LT-SL) via pre-equilibration with (0.1M) NaCl for 0.8 years, followed by 7 years equilibration with ^{133}Ba; this long time treatment was carried out by Heberling et al., 2018.

The crystals of AR and IB were identical to the ones used in the cubes experiment; they were ball-milled for 30 sec and sieved with a 50μm sieve. They particles underwent a cycle of sonication for several minutes in MilliQ water to remove small particles, followed by wet-sieving with a 10μm sieve to obtain particle size of 50-10μm.

5.1.2 Barite used for experiments in the presence of ^{226}Ra: precipitated and ^{226}Ra long time treated

$BaCl_2$ solutions were prepared to have five batches with ($8.56 \cdot 10^{-3}$ mol/L) concentration and 5 ml volume each denoted as RB1, RB2, RB3, RB4, and RB5, which were then each spiked with ($4.28 \cdot 10^{-7}$ mol/L) of (0.004 mol/L) HNO_3 Ra source. Similarly, one batch was prepared in the absence of Ra denoted as BB. The pH of Ra spiked batches was adjusted to be identical to free Ra batches (5.23 ± 0.03) NaOH and using an Apera LabSen881 glass-body pH electrode

and Orion Dual Star Benchtop pH meter from Thermo Fisher Scientific. The pH electrode was calibrated against five standard reference buffer solutions. To initiate co-precipitation, (5 ml) of Na_2SO_4 with (0.1 mol/L) concentration was added to each batch to form 10 mg of Ra doped barite. The batches were then kept in the oven for 6 days at 60°C and then at ambient temperature for 3 weeks.

After that solid / liquid separation was carried out by centrifugation and decantation, and the solution pH was measured. The solids were washed with MilliQ water two times with centrifugation after washing. The solutions and solids of a Ra batch and a Ra free batch were analyzed with gamma spectroscopy, ICP-OES, XRD SEM-EDX, and SEM-EDX to determine Ra activity, Ba concentration, morphology and elemental distribution, and crystallinity. For gamma spectroscopy, 3 ml of the solutions were transferred into 10 ml Kautex bottles and measured for 4 hrs. In addition, 3 ^{226}Ra known activity (50, 10, 300 Bq) standards with volumes of 3ml each were prepared and submitted along the samples of the RB series to determine the activities of the samples. Solutions for ICP-OES (Perkin Elmer Optima 2000) analysis were diluted (1:2) with 2% HNO_3 Suprapure. For solid characterizations, sample solids were washed with MilliQ water and ethanol multiple-times to remove salt. The solids were prepared in ethanol suspensions then onto a flat Si wafer in an airtight specimen holder for samples which reacted in the presence of ^{226}Ra, whereas the batch solid without ^{226}Ra was prepared in the same wafer, but without the airtight holder (Bruker) to obtain XRD diffractograms in a D8 advance Powder XRD (Bruker AXS). The XRD was equipped with a Cu radiation source and Ni filter and its radiation source current and voltage were set at 40 mA and 40 kV. Diffractograms were recorded in a 2θ angular range of $10 - 70^0$, and a step size of and 0.015^0 at 0.4 seconds/step and a sample stage rotation 30 r/min. XRD patterns were analyzed via the EVA V5.0 (Bruker AXS) and Topas 4.2 software (Bruker AXS). The suspensions were also prepared onto Al Pin stubs for SEM and SEM-EDX using a FEI QUANTA 650 FEG environmental SEM with a CamScan CS44FE for image acquisition, equipped with EDX and operating at an electron accelerating voltage of 30 kV.

The ^{226}Ra long treated SL $(Ba, Ra)SO_4$ solids (RaLT-SL) were prepared by Heberling et al., F., 2018 as follows: firstly, solids were pre-equilibrated for 0.8 years in (0.1 mol/L) NaCl (Merck, reagent grade) as background electrolyte in batches of 100 mL in Kautex bottles (S/L = 0.1 g/L). After the pre-equilibration step, the solids were spiked with ^{226}Ra ($0.44 \pm 0.04 \cdot 10^{-09}$ mol/l, denoted as B; $1.1 \pm 0.1 \cdot 10^{-09}$ mol/l denoted as C; and $11 \pm 1 \cdot 10^{-9}$ mol/L denoted as D) to be then equilibrated for 7.0 years with ^{226}Ra. After 7

years of equilibration, the reaction was terminated. Solid / liquid separations for the batches were carried out via centrifugation to retrieve the solids. Cycles of washing with ethanol and MilliQ were carried out for the solids, which then were prepared in ethanol suspensions for analysis.

For revealing changes in particles crystallinity, $(Ba, Ra)SO_4$ solids were analyzed with XRD. To uncover the morphological changes that crystals underwent, solids were measured via SEM. XRD and SEM preparations followed identical protocols as precipitated barite preparation.

To measure the ^{133}Ba activity via gamma spectroscopy, aliquots were withdrawn from centrifugates, diluted (1:10) with 2% HNO_3 Suprapure and measured.

5.2 Recrystallization experiments

5.2.1 Barite cubes and powders experiments

The cubes of AR and IB were contacted with 0.1 mol/L NaCl (VWR Chemicals, 99.9%) and S/L ($\cong$ 1) for 10 days as a pre-equilibration period at temperatures of 25^0, 40^0 and 60^0 C. Thermodynamic calculations using PhreeqC (Parkhurst and Appelo, 1999) and the Nagra/PSI thermodynamic database (Hummel et al., 2002), were employed to calculate the amount of barite, expected to dissolve upon the contact with the NaCl solution. To prevent dissolution, 0.35 µmol/L of $BaCl_2$ (Alfa Aesar, anhydrous, 99,998%) as well as Na_2SO_4 (Merck Superapur, anhydrous, 99.99%) were added to batches, prior to immersing the barite cubes.

The powder pre-equilibration step for the four types of barite powder was identical to the cubes pre-equilibration step, except it was only carried out at 25^0 C. No pre-equilibration period was applied for the LT-SL powder as it was already pre-equilibrated by Heberling et al., F., 2018.

The reactions were initiated by treating the cube batches with Na_2CO_3 solution (Meck, anhydrous, for analysis) and the concentrations were (0.01, 0.05 and 0.1 mol/L), pH (11) and (S/L = 1 g/l). The reactions were stopped after defined time intervals throughout 30 days and pH was measured. The solid / liquid separation was via decantation and the cubes were then washed with ethanol and MilliQ water in ultrasonic bath to remove precipitants of NaCl followed by a drying step at ambient temperature. Upon dryness and as a preparational step for analysis, most of the cubes were embedded in epoxy resin, cut into halves, mirror polished and washed with ethanol and MilliQ water in the ultrasonic bath and dried; some cubes were left without the aforementioned cutting procedure.

The carbonate treatment for powders were at 25^0 C and concentrations for powders were similar to the cubes except for LT-SL concentration that was only (0.1M). The pH values for

powder batches were (9.50, 10, 11), LT-SL pH was (10 and 11.30). For solid / liquid separation, batches were centrifuged (Thermo Fisher Scientific Megafuge 2.0R), followed by decantation of the liquid phase. The centrifugates were washed with ethanol and MilliQ water and prepared in ethanol suspensions for analysis.

5.2.2 Precipitated and ^{226}Ra long treated SL $(Ba, Ra)SO_4$ barite experiments

After pre-equilibration, the solids RB1, RB2, RB3 and RB4 were contacted with 10 ml of Na_2CO_3 (0.15M, S/L =1) solution and pH was adjusted to 11. RB series after the contact with carbonate were denoted as: RBC1, RBC2, RBC3 and RBC4. The batches were subsequently terminated after 7, 14, 21 and 44 days. At each termination, pH was measured, solid / liquid separation was carried out and solid and liquid analyses were preformed after centrifugation identical to the steps carried out for batch experiments on powders reacted in the absence of Ra.

The RaLT-SL solids were contacted with (0.1 M) Na_2CO_3 solution (S/L = 1 g/L). RaLT-SL solids after carbonate contact denoted as SL-Ra series and were divided into eight batches as: SL-RaA10, SL-RaB10, SL-RaC10 with pH adjusted to 10; and SL-RaA11, SL-RaB11, SL-CRa11 with pH adjusted 11. The letters A, B, D indicate the initial ^{226}Ra concentrations that Heberling, F., et al., 2018 spiked: $4.4 \cdot 10^{-10}$, $1.1 \cdot 10^{-11}$ and $1.1 \cdot 10^{-8}$ mol/L, respectively. The reaction periods, pH measurements and termination procedures are identical to RBC series expect that the last batch was terminated after 30 days reaction time instead of 44 for RBC.

5.3 Characterization and analysis after recrystallization experiments

5.3.1 Barite cubes and powders

The uncut cubes analysis was done by optically inspecting them with a video microscope (Keyence VHX-1000D) to study external surfaces of the cubes after reactions. The video microscope allowed for a good visual impression of the surface features after reaction with carbonate. The unreacted cubes, reacted cubes and embedded cubes were then analyzed by employing a Senterra Raman Microscope (Bruker) equipped with a laser wavelength and power of 785 nm and 25 mW; Raman spectra were analyzed via the OPUS spectroscopy software (Bruker). For internal investigation of the cubes, the embedded cubes were then sputtered with carbon and mounted to Al in Stubs for SEM and SEM-EDX analysis. XRD was used to investigate the mineralogical composition of reacted powders by having suspensions prepared on a flat Si wafer. XRD patterns were analyzed via Eva V5.0 Topas 4.2.

The physical characteristics of reacted and unreacted powder surfaces were studied via the SEM and SEM-EDX. For gaining more structural insights into the samples interior characteristics, a $60Ga^{+}$FIB instrument was employed. The FIB instrument is part of the NVision 40 CrossBeam® workstation (Carl Zeiss AG, Germany) units equipped with imaging and analytical capabilities of the high resolution field emission GEMINI®SEM with the high performance SIINT zeta FIB column; and thus ion milling and physical characterizations can be operated simultaneously. Milling current was initially 700 pA for sample layers milling and then reduced gradually to 150 pA for polishing milled zones.

For analyzing Ba release into the solutions from cubes and powders during reacting with carbonate, aliquots of the experimental solutions were diluted (1:5) with 2% HNO3 and measured via ICP-OES.

The solids of RB and SL-Ra series were measured via XRD with identical sample preparation and instrumental step-ups used for analyzing the retrieved the RB precipitants and RaLT-SL solids. For solution analysis via gamma spectroscopy (Canberra GX3018-7500SLGermanium detector; spectra were analyzed using the Canberra Genie 2000 software) for RB series, (3 ml) of undiluted solutions of each batch were transferred into 10 ml Kautex vials and measured. Known ^{226}Ra activity standards were submitted along CRB batches as well to calculate RBC activities similar to RB series. For SL-Ra series, aliquots were diluted (1:10) with 2% HNO_3 Suprapure into 10 ml Kautex vials to obtain ^{226}Ra activity via gamma spectroscopy. In addition, solutions from each batch were diluted by 1:5 with 2% HNO_3 for measuring Ra concentration via ICP-MS (ELEMENT XR from THERMO Scientific) for SL-Ra samples as another mean with a low detection limit. To measure Ba concentrations via ICP-OES (Avio550Max, PerkinElmer) for RBC and SL-Ra series, solutions were diluted (1:5) with 2% HNO_3 Suprapur.

5.4 The precipitation of witherite in the presence of Ra

$BaCl_2$ solutions (5 ml) were prepared similar to solutions prepared for precipitated of barite in the presence of Ra, but the Ra source (0.004 M HNO_3, 45 kBq/L) was spiked into four batches with the following denotations and concentrations: RW1, 8.25 kBq/L; RW2, 0.825 kBq/L; RW3, 82.50 Bq/L; RW4, 8.25 Bq/L. In addition, Ra free $BaCl_2$ solutions were prepared for one batch denoted as W. The pH of the batches was adjusted to 2.32±0.04. This was followed by the introduction of 0.1 M Na_2CO_3 solutions (5 ml) that were added to the batches and pH for the batches was then adjusted at 11. The batches were left for a period of 4 weeks

in ambient temperature, followed by the reaction termination for all the batches and measurements of pH.

The solid / liquid separation step was carried identical to the procedures mentioned before as well as the washing cycles. The solids were then prepared in ethanol suspensions for analysis. The analysis preparation and analysis for RW series solids via XRD, SEM and SEM-EDX were identical to the way the aforementioned series. At the end, RW series solids were digested in (3ml) 2% HNO_3 for measuring ^{226}Ra in the solids via gamma spectroscopy.

^{226}Ra analysis in solution was performed identically to the RB and RBC series. For measuring Ba in the solutions, (1:1) dilution with 2% HNO_3 was done for analysis via ICP-OES.

Table 3. Summarized experimental details and analysis methods for barite and witherite precipitation experiments the presence of radium

Experimental series	Starting materials	Concentrations (M)	pH	Temperature (°C)	Reaction periods (days)	Analytical methods	Computing methods
RB1	Sulfate solution and barium-radium solution	Na_2SO_4 (0.1) $BaCl_2$ (8.56E-3) $^{226}Ra^{2+}$ (4.26E-7)	5.5	60°C for 4 days followed by 25^0 for 3 weeks	25	ICP-OES, gamma spectroscopy	PHREEQC code DFT-SDM
RB2	Sulfate solution and barium-radium solution	Na_2SO_4 (0.1) $BaCl_2$ (8.56E-3) $^{226}Ra^{2+}$ (4.26E-7)	5.5	60°C for 4 days followed by 25^0 for 3 weeks	25	ICP-OES, gamma spectroscopy	PHREEQC code DFT-SDM
RB3	Sulfate solution and barium-radium solution	Na_2SO_4 (0.1) $BaCl_2$ (8.56E-3) $^{226}Ra^{2+}$ (4.26E-7)	5.5	60°C for 4 days followed by 25^0 for 3 weeks	25	ICP-OES, gamma spectroscopy	PHREEQC code DFT-SDM
RB4	Sulfate solution and barium-radium solution	Na_2SO_4 (0.1) $BaCl_2$ (8.56E-3) $^{226}Ra^{2+}$ (4.26E-7)	5.5	60°C for 4 days followed by 25 for 3 weeks	25	ICP-OES, gamma spectroscopy	PHREEQC code DFT-SDM
RB5	Sulfate solution and barium-radium solution	Na_2SO_4 (0.1) $BaCl_2$ (8.56E-3) $^{226}Ra^{2+}$ (4.26E-7)	5.5	60°C for 4 days followed by 25 for 3 weeks	25	XRD, SEM, SEM-EDX ICP-OES, gamma spectroscopy	PHREEQC code DFT-SDM
B	Sulfate solution and barium solution	Na_2SO_4 (0.1) $BaCl_2$ (8.56E-3)	5.5	60°C for 4 days followed by 25 for 3 weeks	25	XRD, SEM, SEM-EDX ICP-OES	PHREEQC code
RW1	Carbonate solution and barium-radium solution	Na_2CO_3 (0.1) $BaCl_2$ (8.56E-3) $^{226}Ra^{2+}$ (4.26E-7)	11	25°C	44	XRD, SEM, SEM-EDX, ICP-OES, gamma spectroscopy	PHREEQC code DFT-SDM
RW2	Carbonate solution and	Na_2CO_3 (0.1) $BaCl_2$ (8.56E-3) $^{226}Ra^{2+}$ (4.26E-8)	11	25°C	44	XRD, SEM, SEM-EDX, ICP-OES, gamma spectroscopy	PHREEQC code DFT-SDM

	barium-radium solution							
RW3	Carbonate solution and barium-radium solution	Na_2CO_3 (0.1) $BaCl_2$ (8.56E-3) $^{226}Ra^{2+}$ (4.26E-9)	11	25°C		44	XRD, SEM, SEM-EDX, ICP-OES, gamma spectroscopy	PHREEQC code DFT-SDM
RW4	Carbonate solution and barium-radium solution	Na_2CO_3 (0.1) $BaCl_2$ (8.56E-3) $^{226}Ra^{2+}$ (4.26E-10)	11	25°C		44	XRD, SEM, SEM-EDX, ICP-OES, gamma spectroscopy	PHREEQC code DFT-SDM
W	Carbonate solution and barium solution	Na_2CO_3 (0.1) $BaCl_2$ (8.56E-3)	11	25°C		44	XRD, SEM, SEM-EDX, ICP-OES	PHREEQC code DFT-SDM

Table 4. Summarized experimental details and analysis methods for different barite types reacting with carbonate in the absence and presence of radium

Experimental series	Starting materials	type	Pre-equilibration period (days)	Na_2CO_3 (M)	S/L (g/L)	pH	Temperature °C	Reaction period (days)	Analytical methods	Computing methods
A1	3x3x3 (mm) cube	IB	10	0.1	1	11	60°C	35	Video-microspore, Raman spectroscopy, SEM, SEM-EDX, ICP-OES	PHREEQC code
A1	3x3x3 (mm) cube	AR	10	0.1	1	11	60°C	31	Video-microspore, Raman spectroscopy, SEM, SEM-EDX, ICP-OES	PHREEQC code
B1	Powder	SL	10	0.01	1	9.50	60°C	36	XRD	PHREEQC code

B2	Powder	SL	10	0.01	1	10	25°C	36	XRD	PHREEQC code
B3	Powder	SL	10	0.01	1	11	25°C	36	XRD	PHREEQC code
B4	Powder	SL	10	0.05	1	9.50	25°C	36	XRD	PHREEQC code
B5	Powder	SL	10	0.05	1	10	25°C	36	XRD	PHREEQC code
B6	Powder	SL	10	0.05	1	11	25°C	36	XRD	PHREEQC code
B7	Powder	SL	10	0.1	1	9.50	25°C	36	XRD	PHREEQC code
B8	Powder	SL	10	0.1	1	10	25°C	36	XRD	PHREEQC code
B9	Powder	SL	10	0.1	1	11	25°C	36	XRD, SEM, SEM-EDX, FIB-SEM, ICP-OES	PHREEQC code
B10	Powder	LT-SL	-	0.1	1	10	25°C	30	XRD, SEM, SEM-EDX, ICP-OES, gamma spectroscopy	PHREEQC code

B11	Powder	LT-SL	-	0.1	1	11.30	25°C	30	XRD, SEM, SEM-EDX, ICP-OES, gamma spectroscopy	PHREEQC code
B12	Powder	IB	10	0.01	1	9.50	25°C	31	XRD	PHREEQC code
B13	Powder	IB	10	0.01	1	10	25°C	31	XRD	PHREEQC code
B14	Powder	IB	10	0.01	1	11	25°C	31	XRD	PHREEQC code
B15	Powder	IB	10	0.05	1	9.50	25°C	31	XRD	PHREEQC code
B16	Powder	IB	10	0.05	1	10	25°C	31	XRD	PHREEQC code
B17	Powder	IB	10	0.05	1	11	25°C	31	XRD	PHREEQC code
B18	Powder	IB	10	0.1	1	9.50	25°C	31	XRD	PHREEQC code
B19	Powder	IB	10	0.1	1	10	25°C	31	XRD	PHREEQC code

B20	Powder	IB	10	0.1	1	11	25°C	31	XRD, SEM, SEM-EDX, ICP-OES	PHREEQC code
B21	Powder	AR	10	0.01	1	9.50	25°C	31	XRD	PHREEQC code
B22	Powder	AR	10	0.01	1	10	25°C	31	XRD	PHREEQC code
B23	Powder	AR	10	0.01	1	11	25°C	31	XRD	PHREEQC code
B24	Powder	AR	10	0.05	1	9.50	25°C	31	XRD	PHREEQC code
B25	Powder	AR	10	0.05	1	10	25°C	31	XRD	PHREEQC code
B26	Powder	AR	10	0.05	1	11	25°C	31	XRD	PHREEQC code
B27	Powder	AR	10	0.1	1	9.50	25°C	31	XRD	PHREEQC code
B28	Powder	AR	10	0.1	1	10	25°C	31	XRD	PHREEQC code

B29	Powder	AR	10	0.1	1	11	25°C	31	XRD, SEM, SEM-EDX, ICP-OES	PHREEQC code
RBC1	Powder	RB1	-	0.15	1	11	25°C	44	XRD, SEM, SEM-EDX, ICP-OES, gamma spectroscopy	PHREEQC code DFT-SDM
RBC2	Powder	RB2	-	0.15	1	11	25°C	44	XRD, SEM, SEM-EDX, ICP-OES, gamma spectroscopy	PHREEQC code DFT-SDM
RBC3	Powder	RB3	-	0.15	1	11	25°C	44	XRD, SEM, SEM-EDX, ICP-OES, gamma spectroscopy	PHREEQC code DFT-SDM
RBC4	Powder	RB4	-	0.15	1	11	25°C	44	XRD, SEM, SEM-EDX, ICP-OES, gamma spectroscopy	PHREEQC code DFT-SDM
SL-RaA10	Powder	RaLT-SL	-	0.1	1	10	25°C	30	XRD, SEM, SEM-EDX, ICP-OES, ICP-MS gamma spectroscopy	PHREEQC code DFT-SDM
SL-RaB10	Powder	RaLT-SL	-	0.1	1	10	25°C	30	XRD, SEM, SEM-EDX, ICP-OES, ICP-MS gamma spectroscopy	PHREEQC code DFT-SDM
SL-RaC10	Powder	RaLT-SL	-	0.1	1	10	25°C	30	XRD, SEM, SEM-EDX, ICP-OES, ICP-MS gamma spectroscopy	PHREEQC code DFT-SDM
SL-RaA11	Powder	RaLT-SL	-	0.1	1	11	25°C	30	XRD, SEM, SEM-EDX, ICP-OES, ICP-MS gamma spectroscopy	PHREEQC code DFT-SDM

SL-RaB11	Powder	RaLT-SL	-	0.1	1	11	25°C	30	XRD, SEM, SEM-EDX, ICP-OES, ICP-MS gamma spectroscopy	PHREEQC code DFT-SDM
SL-RaC11	Powder	RaLT-SL	-	0.1	1	11	25°C	30	XRD, SEM, SEM-EDX, ICP-OES, ICP-MS gamma spectroscopy	PHREEQC code DFT-SDM

1

6 Computational approaches

6.1 Atomistic simulations: the Density Functional Theory based Single Defect Method

Density Functional Theory (DFT) (Hohenberg and Kohn, 1964; Kohn and Sham, 1965; Balasubramanian, 1998) is used as a quantum-mechanical atomistic simulation tool to obtain electronic energies and atomic structures of solid phase systems. The electron density is a function of variable positions of electrons and the energy of the system is a functional of the electron density. DFT is used in the present study with periodic boundary condition (PBC) in the Vienna Ab Initio Simulation Package (VASP) (Kresse and Hafner, 1993; Kresse and Furthmüller, 1996a; Kresse and Furthmüller 1996b). A plane-wave basis set was employed to solve the Kohn-Sham equations. The Perdew-Burke-Ernzerhof (PBE) version (Perdew et al., 1996) of the generalized gradient approximation (GGA) was utilized for describing Electron exchange and correlation. The modeling of ion cores was via projector augmented wave (PAW) potentials (Blöch, 1994) as described by Kresse and Joubert, 1999.

DFT-based electronic energies are employed in the Single Defect Method (SDM) approach as implemented by Vinograd, V.L., et at., (2013), to calculate solid solution non-ideality. Therefore, the endmember structures and a solid solution containing a single defect, i.e. a super-cell of the host crystal with a single substitutional foreign atom replacing one of the system original atom are optimized.

DFT-SDM Computations for Ba (SO_4,CO_3), (Ba,Ra)SO_4 and (Ba,Ra)CO_3

A bulk calculation of a witherite unit cell was run with a kinetic energy cutoff 500 eV. The unit cell was then relaxed by changing degrees of freedom: ion positions, cell shape and cell volume, respectively. The relaxed unit cell was then used to generate a 2 x 2 x 2 witherite supercell and relaxed similarly to the unit cell. Consequently, the relaxed witherite supercell was run with one of the 32 CO_3^{-2}groups being replaced by one SO_4^{-2}group. To resemble a total replacement of witherite supercell CO_3^{-2} with SO_4^{-2}, a bulk of a barite unit cell was run with kinetic energy cutoff 500 eV. Then relaxation procedures of the barite unit cell were carried out similar to witherite procedures and a 2 x 2 x 2 supercell was generated and relaxed to mimic a complete replacement of witherite into barite.

DFT calculations for the formation of Ra doped barite the solid-solution (Ba,Ra)SO_4 was implemented with SDM and PBC. Initially, a bulk of barite unit cell was run with the following:

cutoff energy was 500 eV, and then the unit cell was allowed to relax. In a converged and relaxed barite 2x2x2 super cell, one of Ba atom was replaced with one Ra atom. Once optimized, the rest of Ba atoms in the super cell were all replaced with Ra atoms and optimized. The details of the calculations are similar to the details stated in (SO_4,CO_3)Ba calculations.
The calculation for Ra doped witherite, (Ba,Ra)CO_3, were carried out in the same fashion as Ra doped barite using a witherite bulk unit cell. The rest of calculations were identical to Ra doped barite.

6.2 Geochemical Modelling using PHREEQC

PHREEQC stands for PH REdox EQuilibrium in C language. It is a computer program to simulate chemical equilibria and reactions, as well as transport processes in geochemical systems (Parkhurst and Appelo, 1999). Applications of PHREEQC extend beyond geochemical questions to natural environments, laboratory experiments and industrial treatments. The program is capable of simulating aqueous solution interactions with different solid materials and gas phases based on equilibrium chemistry as well as modeling kinetic reactions and one-dimensional transport. One important capability of PHREEQC is the simulation of geochemical equilibria between various phases such as dissolution and precipitation of solid phases and gases, which allows for obtaining molalities, activities of aqueous species, pH and saturation indices. The one-dimensional transport can be simulated to facilitate the calculations for solute diffusion in a porous medium with the options of different flow directions, boundary conditions and diffusion coefficients.

PHRREQC diffusional model calculations

To assess possible reasons for the slowdown of cubes replacement reaction after a certain reaction period (see results and discussion), a PHREEQC diffusion model was implemented. The model was set to simulate the growth of witherite on barite cubes. It consisted of 21 cells in a 1D diffusion column. The two cells at the ends were designated as a replacement reaction front holding a reservoir of barite while the cell at the other end resembled bulk solution as a carbonate reservoir, with conditions similar to the cubes experiments. The rest of the cells were meant to resemble the witherite crust with a porosity of 18 %, which was based on theoretical considerations and experimental observations (see results and discussion). The boundary conditions were defined as Neumann conditions (No flux at boundary) the transport model was set to “diffusion only”; therefore, the solution is stagnant and carbonate travels through the witherite cells to the reaction front and sulfate and barium diffuse between reaction front and

the solution bulk. The database used for the diffusion model calculation was PHRREQC.DAT (Parkhurst and Appelo, 1999).

PHREEQC calculations for saturation levels, solid solutions mixing, and precipitation

A solution of NaCl (0.1 mol/L) with different carbonate concentrations (0.01-0.1 mol/L), pH (8-11) and temperature (25-60 °C), was equilibrated with barite,. to assess conditions at which witherite formation may be expected, i.e. the saturation index of witherite is > 0. Based on these calculations experimental conditions were selected. The database used for the aforementioned calculations was PHRREQC.DAT (Parkhurst and Appelo, 1999).

PHREEQC was also used to simulate the reaction of carbonate solution with $(Ba, Ra)SO_4$ solid solution using the results of Heberling et al. (2018), as their samples are being used in the current study, as shown in the experimental details. The aim of this solid solution simulation was to determine the experimental conditions at which $(Ba, Ra)SO_4$ transforms into a $(Ba, Ra)CO_3$ solid solution, and to assess whether a change in Ba/Ra ratio is to be expected.

The database PHREEQC.DAT was used with Ra being added to the solution master species list. The following aqueous complexes and reactions for Ra were considered (ThermoChimie-TDB database, Grivé et al., 2015):

$Ra^{2+} \rightleftharpoons Ra^{2+}$ ($\log K = 0.0$)

$RaCO_3 \rightleftharpoons Ra^{2+} + CO_3^{2-}$ ($\log K = 2.500$)

$RaHCO_3^{+} \rightleftharpoons Ra^{2+} + HCO_3^{-}$ ($\log K = 10.920$)

$RaSO_4 \rightleftharpoons Ra^{2+} + SO_4^{2-}$ ($\log K = 2.760$)

$RaCl^{+} \rightleftharpoons Ra^{2+} + Cl^{-}$ ($\log K = -0.100$)

A solution of carbonate and background electrolyte NaCl at 25 °C was set to equilibrate with the $(Ba, Ra)SO_4$ phase. The $(Ba, Ra)SO_4$ unitless Guggenheim excess free-energy parameter of solid solution non-ideality (0.84) obtained from DFT-SDM calculations (see results details) was used to account for solid solution non-ideality, as discussed in detail in the chapter on solid solution mixing.

The precipitation of barite in the presence of radium to form $(Ba, Ra)SO4$ solid solution and the transformation to $(Ba, Ra)CO3$ via the addition of carbonate was simulated as well using ThermoChimie-TDB database (Grivé et al., 2015). The simulation was carried out via mixing (Ba,Ra) solution with a sulfate solution to form $(Ba, Ra)SO4$. Subsequently, carbonate solution was equilibrated with $(Ba, Ra)SO4$, which is resulted in $(Ba, Ra)CO3$.

The precipitation of witherite in the presence of Ra was simulated as well to shed light on Ra partitioning into witherite, forming a $(Ba, Ra)CO3$ solid solution. The simulation was

preformed using the ThermoChimie-TDB database (Grivé et al., 2015) by mixing a (Ba,Ra) solution with a carbonate solution to form a $(Ba, Ra)CO_3$ solid solution and the DFT-SDM obtained non-ideality parameter (0.58) for that purpose.

7 Results

7.1 DFT-SDM computations

The 2x2x2 supercell structures of barite, radium sulfate, witherite, radium carbonate endmembers and Ra substituted Ba structures as well as the structure of SO_4^{2-} substituted CO_3^{2-} are all shown in *Table 5*. The optimized electronic energies obtained after the calculations are listed below the corresponding structures. It is clear that there is an increase of the energy of system when a single Ba atom is replaced with Ra and further increase occurred when the whole system Ba atoms replaced with Ra atoms. The increase in electronic energy upon substituting Ba with Ra in the barite supercell and further replacing all Ba with Ra indicates that the presence of Ra destabilizes the barite structure. This destabilization is due to the larger ionic radius of Ra 1.54 Å compared to Ba 1.47 Å (Yoshida, Y. et al., 2014), which causes lattice distortions and increases the overall energy of the system. The results highlight the less favorable incorporation of Ra into the barite lattice compared to Ba. The substitution of one single Ba atom with a Ra atom in the witherite supercell caused the system energy to increase as well, and a further increase of the energy of the system occurred when all Ba atoms in witherite were replaced with Ra atoms showing a similar effect of Ra replacement with Ba as in the barite system. The replacement of one CO_3^{2-} with one SO_4^{2-} showed a high increase in the system energy much more than the increase seen after the replacement of Ba with Ra for barite and witherite.

The reaction energies calculated from the electronic energies can be considered as a good approximation for the excess free energy of mixing ($\Delta E \cong \Delta G_E$, Heberling et al., 2014; Polly et al., 2017). Therefore, ΔG_E can be calculated by using the electronic energies obtained from DFT-SDM as follows:

$$\Delta G_E = \frac{G(BA_{x-1}\,CA_1)_{strained} - G(BA_{x-1}\,CA_1)_{relaxed}}{1/x}$$

Equation 26

where BA_{x-1} barite or witherite supercell with one atom of Ba replaced with one atom of Ra or with one CO_3^{2-} replaced with SO_4^{2-}, whereas CA_1 is radium sulfate in barite supercell, radium carbonate in witherite supercell or barite in witherite supercell. The subscript "strained"

denotes enthalpic contributions as discussed in solid solution chapter, whereas The subscript "relaxed" denotes a mechanical mixture, where the atomic positions are also allowed to relax, but without any strain relative to the pure host phase, as the interaction between components is minimized, and there are no external effects. When the energy of the system after relaxation reflects only the contribution from the mechanical mixture (i.e., no excess enthalpy), the solid solution can be considered ideal (Vinograd et al., 2013; Heberling et al., 2014; Polly et al., 2017). The (1/x) is the molar fraction, where x is the number of cations or anions in 2x2x2 supercell (32); the division over (1/x) is to account for ΔG_E for the whole system atoms replacement not just the replacement of one atom with another.

The calculations showed that ΔG_E for the substitution of Ra into barite is (2.10 kJ/mol). This positive value indicates that the mixing of Ra into the barite structure is energetically unfavorable, leading to an increase in the free energy of the system. This further supports the observation that Ra substitution destabilizes the barite structure. The calculations of ΔG_E for the witherite system after the replacement of Ba with Ra turned out to be (1.45 kJ/mol), which also indicates unfavourable energetics, however, less than for Ra in barite. In the case of substituting sulfate into witherite, the results indicate that this replacement is highly unfavorable. Notably, the strain associated with this substitution was so significant that the system did not converge to a well-relaxed structure, resulting in a highly distorted sulfate group. The non-ideality parameters can be calculated from the ΔG_E values as follows (Vinograd et al., 2013):

$$a_0 = \Delta G_E/\mathrm{RT}$$

Equation 27

Table 5. shows the system structures used for DFT calculation as well as the resulted structures along the resulted energies that used to obtain non-ideality parameters.

System	$BaSO_4$	$(Ba_{31}Ra_1)SO_4$	$RaSO_4$	$BaCO_3$	$(Ba_{31}Ra_1)SO_4$	$BaCO_3$	$(CO_{31}SO_1)Ba_{32}$
Structures	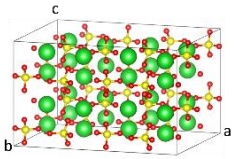	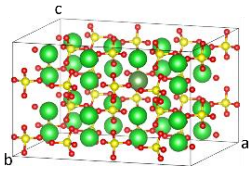	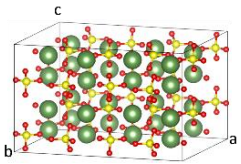	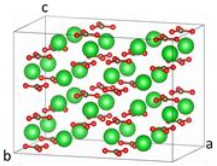	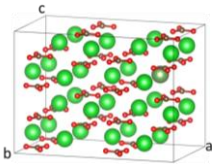	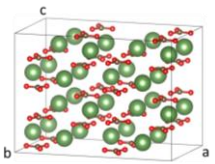	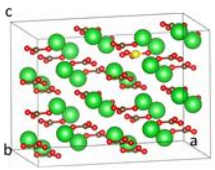
Total energy (kJ/mol)	-3792.0982	-3789.8697	-3722.7863	-3599.9763	-3597.5328	-3523.2354	-3590.3415
ΔG_E (kJ/mol)	2.10			1.45			105.9821
Non-ideality parameter, a_0	0.84			0.58			42.75

7.2 Characterization of initial solid materials

7.2.1 Barite used for experiments in the absence of ^{226}Ra

The crystals forms of type IB and AR barite

Visual inspection of the raw IB and AR barite crystals before they were cut into cubes and milled into powder provides insights into their growth conditions. The images of the raw IB and AR crystals show significant differences in their physical appearance (see Figure 13). In type IB barite, crystals appear rough and pseudomorphic and exhibits smaller crystallite sizes, as typical for hydrothermal barite formation in mineral veins, while type AR exhibits clear idiomorphic barite single crystals, indicating stable and favorable growth conditions.

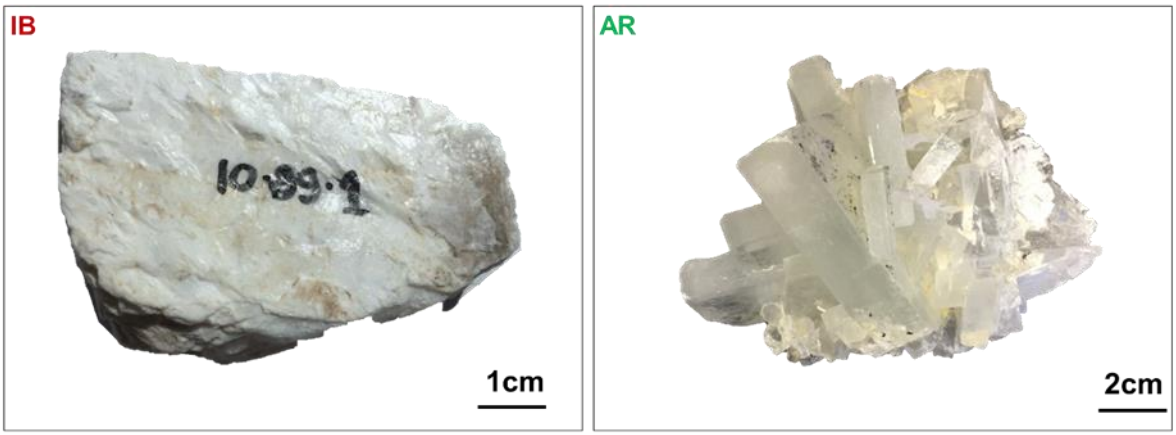

Figure 13. Images for IB and AR crystals form before cutting and milling.

Cubes

The crystals forms seen in Figure 13 are the ones, where cubes were cut out of in sizes of approximately 3x3x3 mm. The cubes were inspected under a digital microscope (Keyence VHX-1000D) to assess their physical appearance after cutting, polishing and washing. As shown in Figure 14, both IB and AR barite cubes exhibited a relatively smooth and uniform surface with some imperfections due to cutting. Both types of crystals were not optically clear indication numerous internal defects.

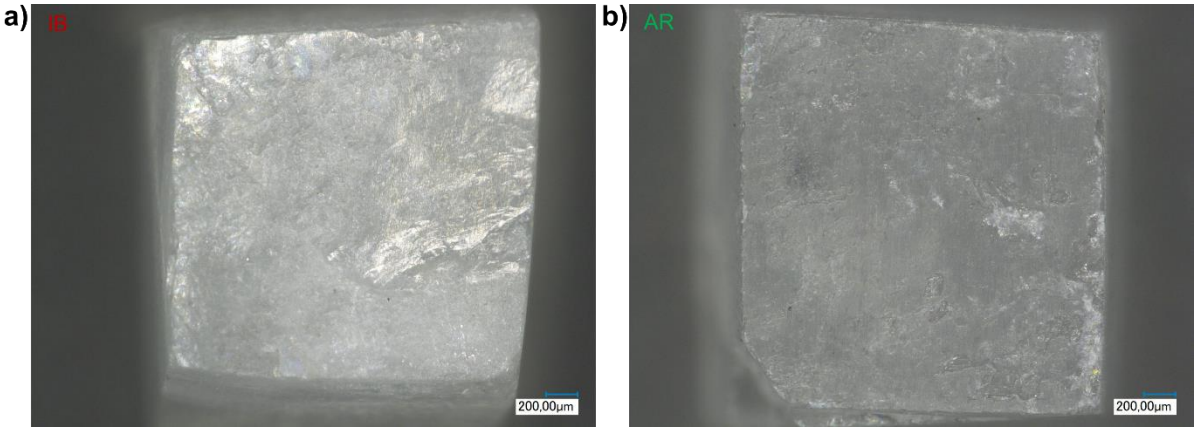

Figure 14. Digital microscope images for the type IB and AR barite after cutting and grinding processes.

Powders

The P type barite was freshly precipitated, leading to the formation of nanoparticles that predominantly appear as aggregates, as observed in Figure 15a. The fast precipitation process under high supersaturation conditions (SI ≅ 7.79) influences the characteristics of the barite, particularly in terms of particle size and crystallinity, as at high supersaturation nucleation of new small crystals is favored over the growth of existing crystals.

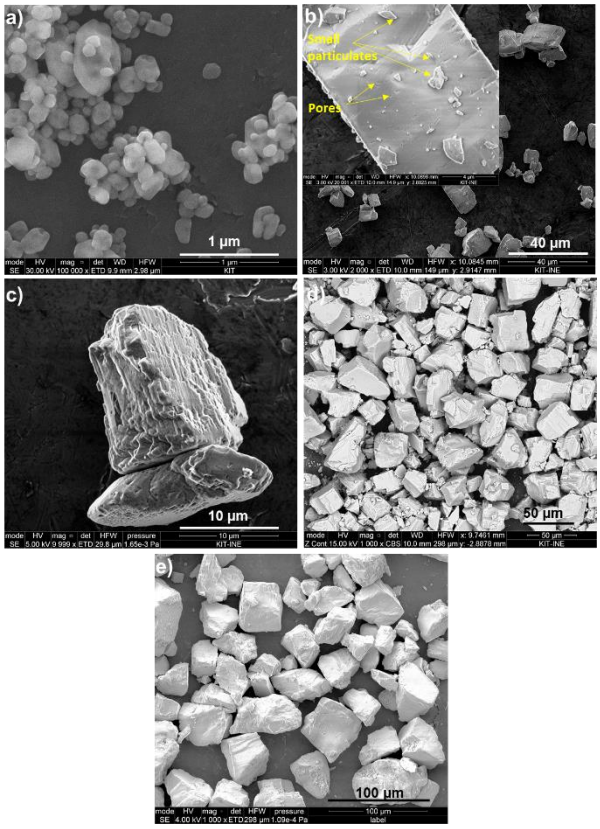

Figure 15. (a) SEM-SE images for P barite in the form of nanoparticles agglomerates with observable roundness effect that particles possess. (b) SEM-SE shows SL barite with its distinct intergrown particulates and surface porosity (c) shows LT-SL after being treated for 7.80 years with 0.1M NaCl with surface irregularities (d) and (e) are SEM-SE for the two-natural barites AR and IB, respectively, that appear to be lumpy and solid particles with no apearnt porosity

P barite has exceptionally small particle sizes (range ~ 100 nm to 100µm). These nanoparticles tend to aggregate, forming larger clusters. The aggregation is possibly due to small precipitant surface areas, which possess high energy that leads them to coalesce in order to minimize the total surface energy (Li and Luo, 2007).

The crystallite size of the resulting particles, is evident in the XRD patterns, which are the broadest compared to other types (Figure 16).(Zhang et al., 2003).

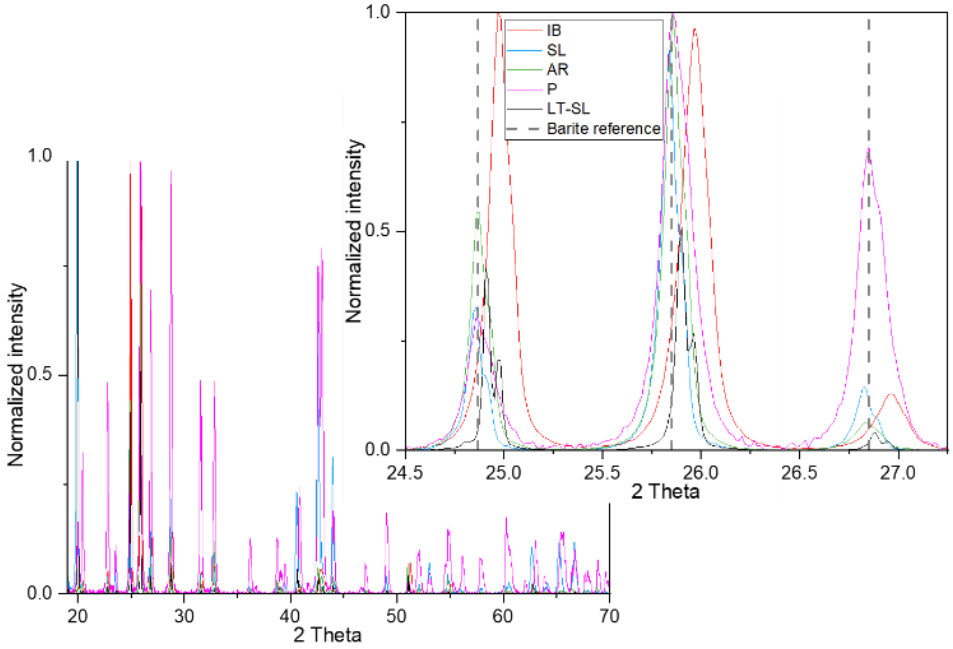

Figure 16. XRD patterns for the starting barite materials and clear differences can be observed. Different starting materials show different peak broadenings. Type IB shows a considerable shift to a higher angle. The barite reference pattern presented here is obtained from Antao, 2012.

The particle size for type SL, IB and AR barite was analyzed by using SEM images to determine the variations in particle dimensions. The distributions, as shown in Figure 17, illustrate both the length and width (long and short axes) of the particles.

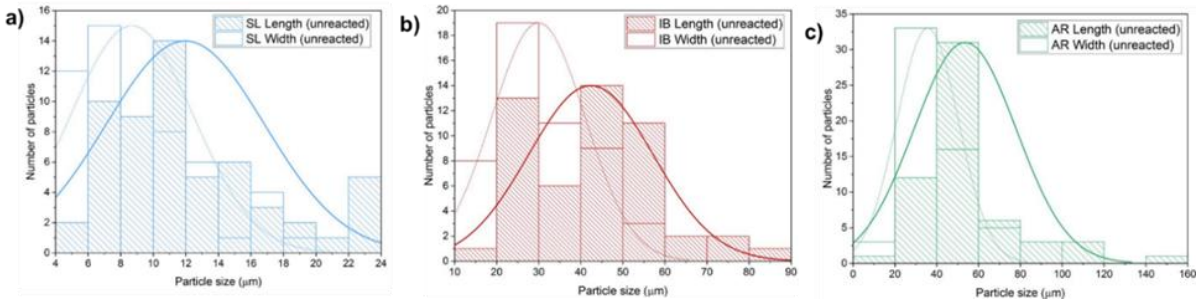

Figure 17. shows particle size distributions obtained from SEM images for different types of barites. Type SL is shown in (a) and has the smallest particles followed by type IB (b) and the largest particles were identified for type AR (c).

The lengths of the SL particles exhibit a wide distribution, with most particles falling between 6 and 18 µm, the width distribution shows that particles fall between 4 and 16 µm. Thus, the

data reveal a moderate variation in particle dimensions. The average L/W ratio is 1.45 ± 0.41. This indicates a moderate elongation of the particles.

The SL type barite exhibits several distinct external and internal particle features revealed by SEM images (see Figure 15.b). A notable characteristic is the presence of small particulates attached to the surfaces of larger SL particles. These small particulates appear to be intergrown with the larger particles, as can be observed in the images shown in Figure 15.b. This intergrowth suggests a complex formation for the SL barite, where smaller crystals may have nucleated on or coalesced with larger crystals during growth.

Another significant feature of the SL barite was its external porosity. The particle surfaces display visible porosity, which is evident from the pitted and uneven texture seen in Figure 15.b. This external porosity could result from dissolution processes or incomplete crystal growth, leading to the formation of voids and channels in the crystal.

In contrast, the LT-SL barite sample that were pre-equilibrated for 7.80 years with 0.1 M NaCl exhibited significantly different morphological characteristics compared to raw SL. SEM images (Figure 15.c) demonstrated that the small intergrown particles observed in the fresh samples vanished, leading to a notable change in surface topography. The surfaces of the LT-SL barite particles appear much rougher, with visible signs of dissolution and reprecipitation processes during long-term reaction with the NaCl solution.

The XRD pattern of the LT-SL barite exhibited sharp peaks indicating high crystallite size, likely due to the extended equilibration period, which allowed for internal restructuring leading to more crystal ordering (Heberling et al., 2018).

The particle size distribution for IB barite shows a higher number of particles in the 30-60 µm length- and 20-30 µm width range (see Figure 17.b). The average length/width ratio is 1.49 ± 0.41, similar to that of SL barite, but with broader particle size distribution and larger average particle size.

The particle size distribution for AR barite is similar, with lengths falling mostly between 40 and 80 µm and widths between 20 and 40 µm (see Figure 17.c). The average length/width ratio is 1.49 ± 0.53, which is close to IB barite.

Both natural barite samples in the present study, type IB and type AR underwent milling, sieving, and washing following identical procedures as detailed before (see 5.1.1). Despite the same preparation method, a IB in Figure 15.e appears to an extent to possess rougher surfaces than AR in Figure 15.d their physical and chemical characteristics were observed. Such

difference observed in the SEM images, can be linked to the features of samples seen in the visual inspections of the raw crystals seen in Figure 13.

The SEM-EDX analysis of the barite samples shows that type IB has a strontium (Sr) content of 1.8 ± 0.2 atomic %. This Sr incorporation in type IB barite is likely influencing its crystalline properties. The presence of Sr in barite as $(Ba, Sr)SO_4$ solid solution can contribute in the diminishment of crystalline size of barite (Brower and Renault, 1971). In contrast, type AR barite, SEM-EDX analysis showed negligible Sr content.

The XRD peaks for type IB are broader compared to those of type AR as can be seen in Figure 16, which suggests a smaller crystallite size. The broadening of the XRD peaks is consistent with the presence of Sr in the lattice, which can introduce lattice strain.

7.2.2 Barite used for experiments in the presence of ^{226}Ra

The RaLT-SL barite type

The SEM images obtained for extended treated RaLT-SL Ra-barite by Heberling, F., et al., 2018 with NaCl (0.1M) and ^{226}Ra shows that such a treatment led to changes in the morphology of particles compared to the fresh SL (Figure 18).

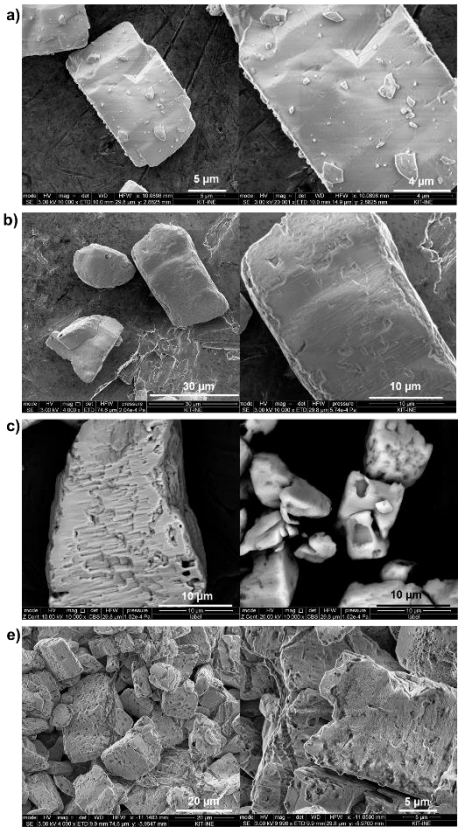

Figure 18. SEM images show (a) exhibited here as a baseline, (b) sample from RaLT-SL series with lowest ^{226}Ra content, (c) sample C with a higher ^{226}Ra content and (d) sample D with highest ^{226}Ra content. Morphologies of samples with ^{226}Ra contents clearly differ compared to each other and compared fresh SL as well.

After treatment of RaLT-SL sample B with NaCl and ^{226}Ra ($0.44 \pm 0.04 \cdot 10^{-09}$ mol/l) for 7.80 years (Figure 18.b), the SEM images show significant changes in the surface morphology of the SL barite. The well-formed edges observed in fresh SL barite are less distinct (see Figure 18.a), and the surfaces exhibit traces of dissolution reprecipitation reactions like etch pits and kinks. The small intergrown particulates present in the fresh sample vanished, suggesting preferred dissolution of the small particles.

Vanishing of small particulates was observed by Heberling et al., 2018 after the pre-equilibration period as well and it was suggested that this is the typical development driven by surface free energy, i.e. Ostwald ripening. This phenomenon occurs as smaller particles dissolve and the material reprecipitates onto larger particles, minimizing the overall surface area and surface energy of the system.

The XRD pattern for RaSL-SL sample B differs compared to the pattern of the fresh SL (Figure 19)

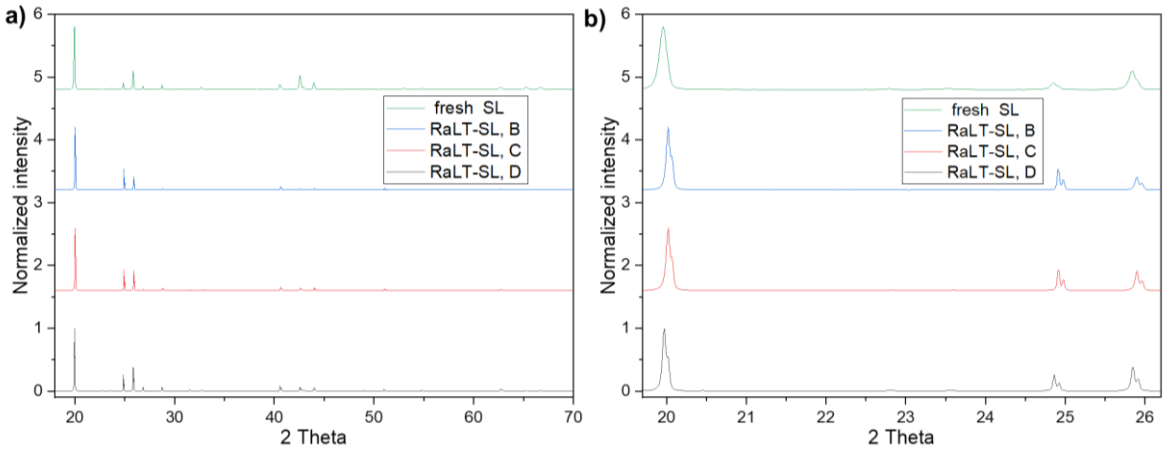

Figure 19. (a) shows XRD patterns and (b) a range chosen from (a) to show peaks of fresh SL displayed here as a baseline, sample from RaLT-SL series with lowest ^{226}Ra content, sample C with a higher ^{226}Ra content and sample D with highest ^{226}Ra content.

The XRD pattern for sample B, shows a notable reduction in peak broadening compared to the fresh SL sample. The XRD pattern for sample B shows a notable reduction in peak broadening compared to the fresh SL sample. This suggests an increase in crystallite size, indicating that the particles have undergone structural reorganization, leading to more stable crystalline domains (Heberling et al., 2018; Zhang et al., 2003). This internal restructuring likely occurred alongside the surface development during the dissolution-reprecipitation processes.

For the RaLT-SL sample C that was treated with a higher concentration of ^{226}Ra ($1.1 \pm 0.1 \cdot 10^{-09}$ mol/l), the SEM images (Figure 18.c) reveals more pronounced surface etching and restructuring compared sample B. Additionally, holes are visible on the particle

surfaces. These holes are indicative of internal restructuring, likely driven by the presence of ^{226}Ra, as suggested by Weber, J., 2017, who carried out internal investigations by FIB-SEM, on SL that were treated with ^{226}Ra for long time. The restructuring process involved coalescence of internal pores toward the outer surfaces, resulting in the observed holes (Weber, J., 2017).

The XRD pattern for this barite also shows a less broadened peaks compared to the fresh SL sample. This is in line with internal restructuring, as suggested by Weber et al., 2017. Similarly, Heberling et al. 2018, who treated the same particles for 4.08 years, observed a narrowing of the peaks and attributed it to the formation of more well-ordered crystals. This indicates that a similar internal restructure that was observed in sample B.

The SEM images of the RaLT-SL sample D treated with the highest concentration of ^{226}Ra ($11 \pm 0.1 \cdot 10^{-09}$ mol/l) show extensive effects as can be seen in Figure 18.e. The number of holes in the particle surfaces is significantly larger compared to samples B and C. This suggests a more effective internal restructuring process at higher ^{226}Ra concentrations, leading to more substantial coalescence of internal pores and resulting in a high abundancy of surface punctures.

The XRD pattern of RaLT-SL sample D shows sharper peaks compared to the fresh SL similar to the what is observed in the patterns of sample B and C (see Figure 19). Sample B and C already show peak shoulders due to Cu $K_{\alpha 2}$ that are not observed in fresh SL, for sample D these shoulders are even more pronounced. This suggests that that the highest Ra-226 concertation induces the most significant changes in the crystallite structure of barite, which confirms the influence of ^{226}Ra on barite internal restructuring suggested by Weber et al., 2017.

7.3 The reaction of barite cubes with carbonate solution

Raman spectroscopy and microscopic inspections

The AR and IB barite cubes contacted with carbonate solution with concentration (0.1 mol/L) and pH 11 at 60 °C resulted in the formation of witherite, as confirmed by Raman point-measurements as recorded on the cube surfaces, shown in Figure 20.a,c. The Raman spectra reveal that witherite peak intensity for both barite types increase with reaction time, while barite peak intensity diminishes as the reaction progresses. Images taken during the Raman measurements show aggregates of hexagonal witherite particles on the surfaces of both types

of barite, giving the surfaces a rough appearance (Figure 20.b,d). This rough texture is indicative of the surface replacement and the formation of porosity during to witherite formation.

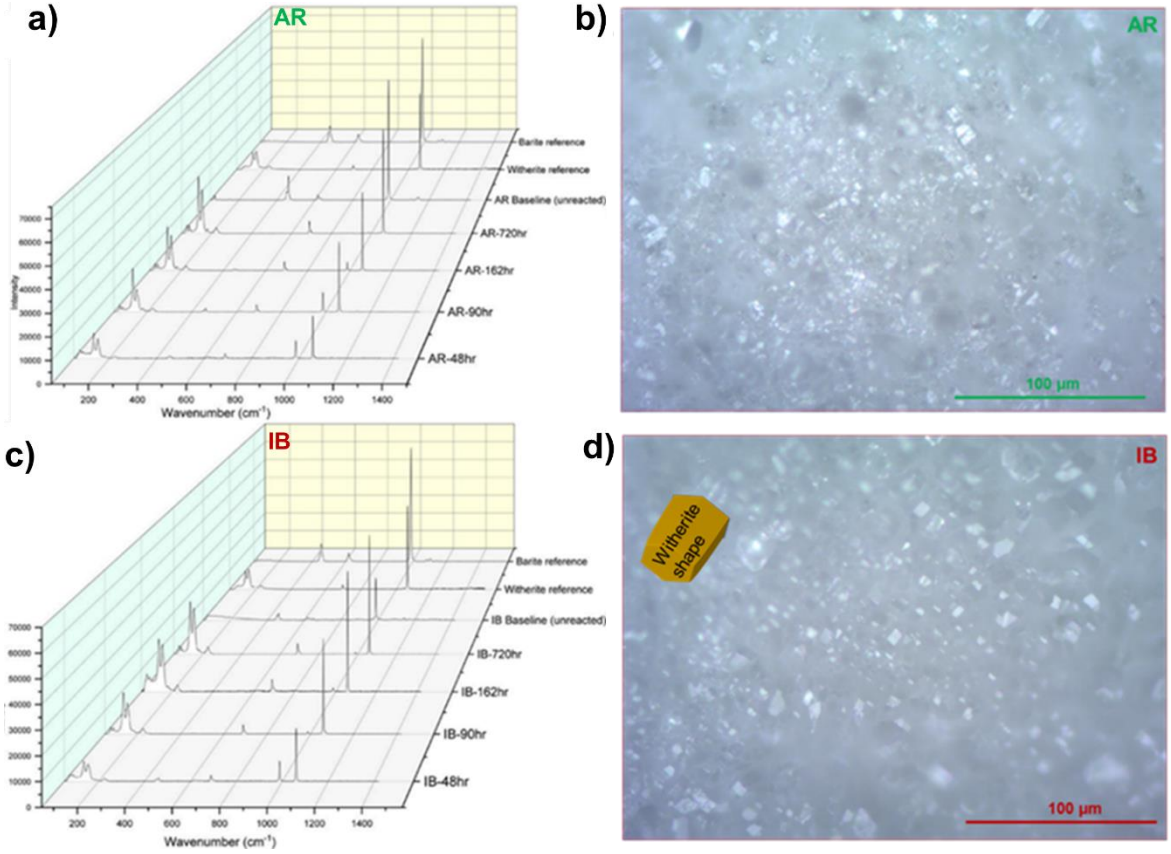

Figure 20. (a) shows spectra for from point measured using Raman technique on AR cube surfaces after reacting with carbonate solution for different time intervals, which show similarity with witherite reference spectrum(b) an image taken via a Raman instrument built in camera displays particles with hexagonal shape that is typical for witherite particles, (c) is similar to (a) but for IB cube and (d) is a similar image in of (b) but for IB cube.

Once the replacement of barite cubes into witherite for both AR and IB types was confirmed via Raman spectroscopy, the cubes were cut into halves and inspected using a digital microscope, as shown in Figure 21.a and Figure 21.b. The images clearly reveal two distinct textures or phases, with one forming a rim around the other, which appears as the parent phase. The rims of both types appear to be porous, whereas the inner parts are much more homogeneous. In the AR cube, the rim displays a relatively smooth texture, while the parent phase appears almost optically clear. In contrast, the IB cube shows a more uniform texture for the parent phase and the porous rim. These observations suggest a distinct replacement process occurring at the surface and making its way into the interior at a reaction front, leading to the formation of the witherite phase.

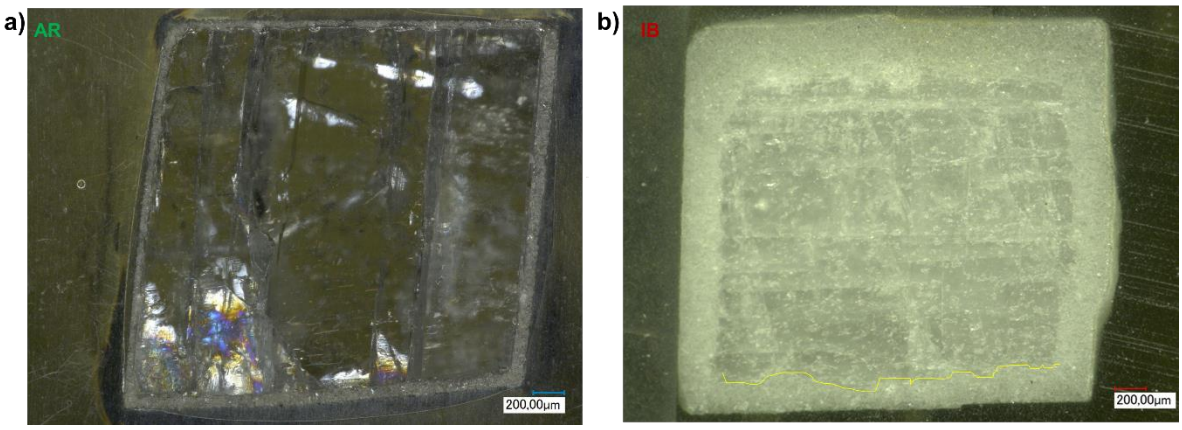

Figure 21. (a) shows a video-microscope image for an AR cube that was reacted with carbonate for a period of 502 hrs and (b) is for an IB cube that was reacted with carbonate for 840 hrs.

To confirm that the rim was indeed witherite and the core was barite, Raman measurement points were recorded, as shown in Figure 22.a and Figure 22.b. The multiple points that were measured in the rims around both barite types, as indicated in the images, confirmed that the rough texture was indeed witherite.

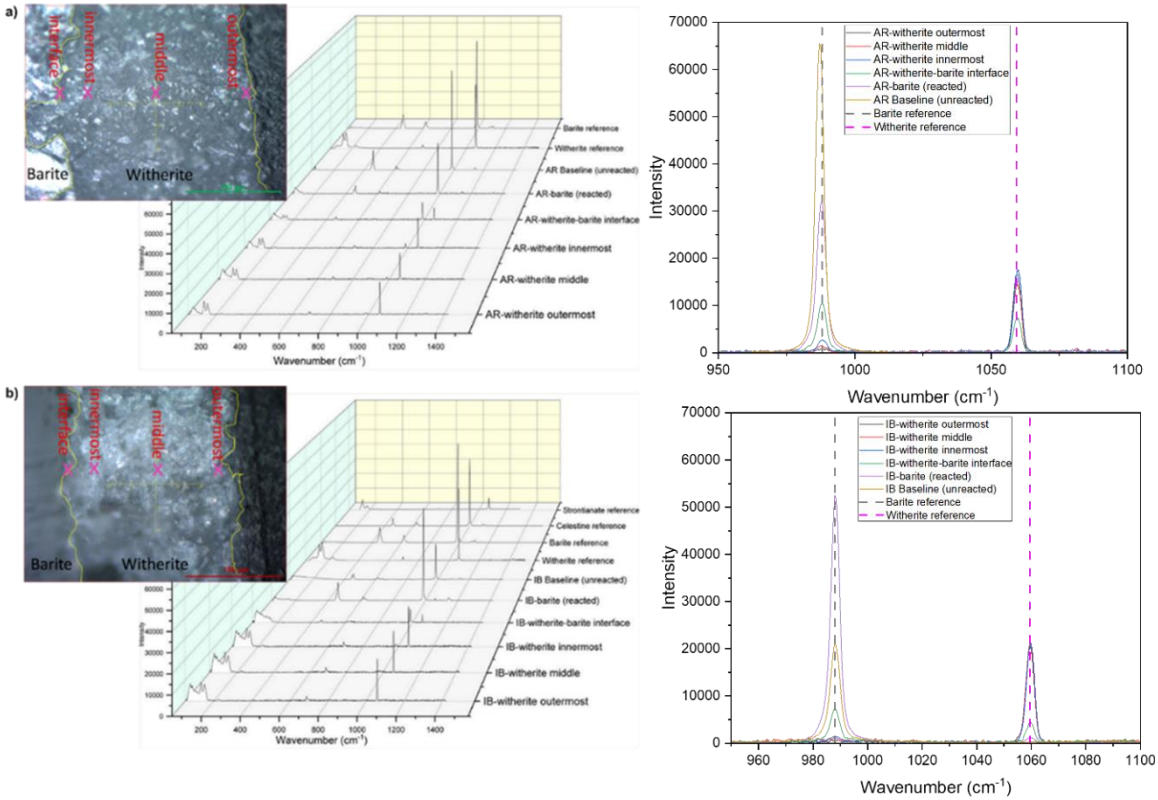

Figure 22. shows in (a) multiple points that were measured via Raman technique in the rim of type AR, which resulted in spectra that matched witherite reference spectrum confirming that the rough rim was newly formed witherite phase and (b) is the same but for IB type. References are obtained from Lafuente et al., 2015; Buzgar and Apopei, 2009.

To delve deeper into the physical features of the cut cubes, SEM images were recorded (Figure 23). The witherite phase rim formed in a way that preserved the shape of the barite bulk,

maintaining a distinct, square appearance. The sharp transition between the barite and witherite phases was clearly revealed, highlighting the distinct textural differences. The texture that was observed in the optical images of the witherite phase (Figure 21) could now be clearly revealed to originate from the porosity that develops in the rims on both barite types. The barite bulk for type AR showed what appeared to be cracks along cleavage planes and some internal porosity, whereas the IB barite bulk exhibited much more internal porosity some pores seem to be concentrated along cleavage planes. These SEM observations provide further insights into microstructural features which may be important for the barite-to-witherite replacement. SEM images emphasize the porosity and surface irregularities introduced in the witherite phase.

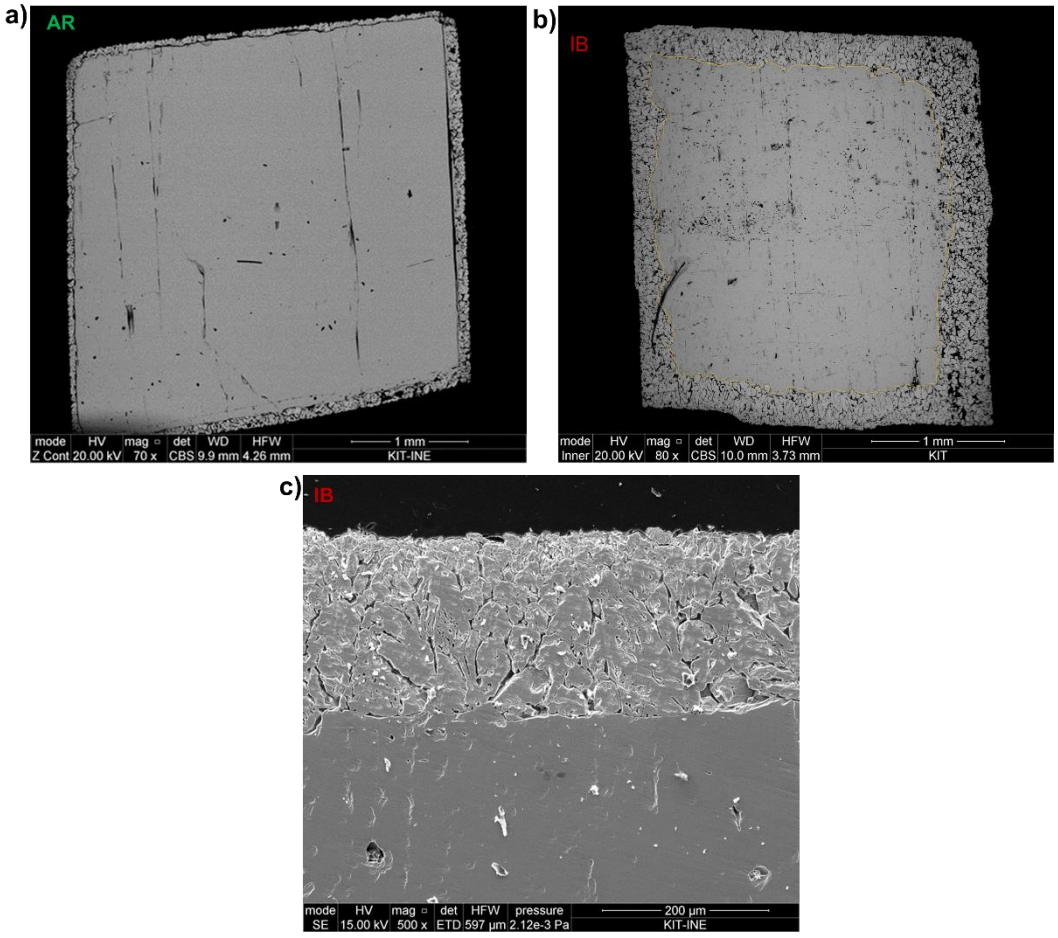

Figure 23. SEM images obtained for cut cubes inspected by SEM, (a) shows AR type with witherite rim layer with pores being revealed clearly. Cracks that are possibly cleavage planes appear clearly in the barite bulk for AR. (b) is similar to (a) but IB type with what appears to be internal porosity. (c) shows a magnified image for IB witherite rim that exhibits interconnected pores and a sharp boundary between the two phases.

For more detailed information on the witherite particles in the rim layer, the magnified SEM image of Figure 23.c revealed several key features regarding their morphology and orientation. The witherite particles in the rim exhibited a highly porous and interconnected structure. The

witherite particles show an orientation perpendicular to the barite-witherite interface, suggesting a particular growth pattern during the replacement process.

The morphology of the witherite particles is irregular. The interconnected pores formed continuous pathways that extended from the surface of the rim all the way to the interface with the barite bulk. This interconnected porosity not only impacted the mechanical properties of the witherite rim but also suggested potential pathways for solution migration during the replacement process.

Additionally, the witherite rim inner part details mimicked the details of the barite bulk surfaces details. This led to the formation of a well-defined sharp boundary between the witherite rim and the barite bulk, resulting in the distinct separation between the two phases.

Growth of the witherite layer and the evolution of porosity

The witherite layer thickness increased over time for both types, as shown in the SEM images of the cubes that reacted with carbonate solution for different periods in Figure 24.

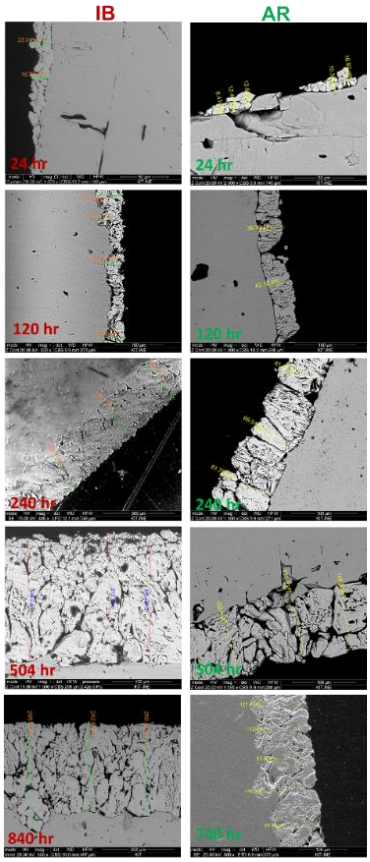

Figure 24. shows the subsequent growth of witherite layers during different time intervals for type IB and AR

The thickness of the witherite layers was converted into witherite formation percentage as a function of time, as illustrated in Figure 25. The rate of witherite layer formation was rapid in the early reaction stages for both AR and IB until about 240 hours. This rapid formation was

followed by a slowdown after about 500 hours. Type IB exhibited a higher reaction rate in both early and later stages, as seen in Figure 25.

The theoretical calculation using PHREEQC (Parkhurst and Appelo 1999) and the Nagra/PSI thermodynamic database (Hummel et al., 2002) predicted that about 40% of the barite should be replaced by witherite under similar experimental conditions. However, in the current study, IB witherite was about 16% after 840 hours, while AR was about 7% after about 740 hours.

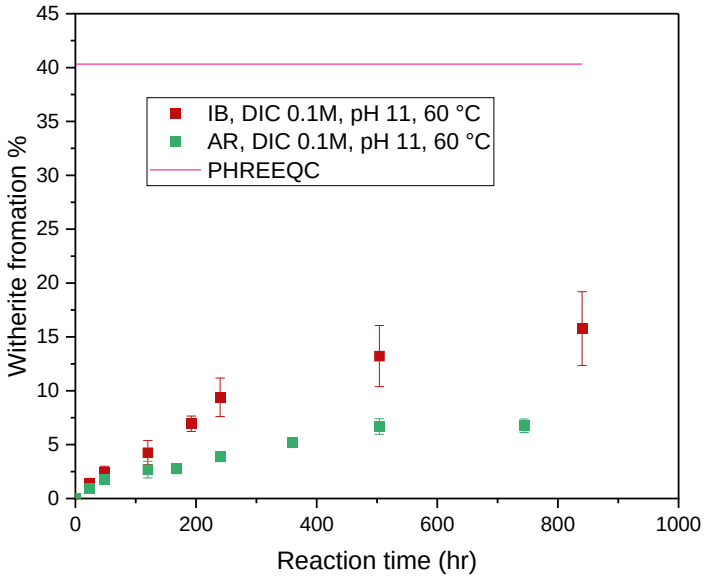

Figure 25. shows the precentage of witherite formed as layers on barite surfaces for both barite types, AR and IB. The replacement reactions are rapid in early stages then it slows down for both types. IB show higher witherite formation. In both types, the formation precent is much less than what's expected.

The compositional analysis of solid and solution phases

The sharp boundary that the cubes exhibited after reaction with carbonate, as seen in Figure 23.c, separates the two phases texturally and compositionally. Elemental maps via SEM-EDX for types IB and AR showed that the two different textures also exhibited two different compositions, one sulfur-dominated and the other carbon-dominated, as shown in Figure 26. The mapping indicated that Ba was present in both textures, signifying that the phase with S was barite and the phase with C was witherite. Additionally, Sr was observed in both phases for type IB, highlighting an important aspect of trace element dissolution from one phase and incorporation into the other during the recrystallization process.

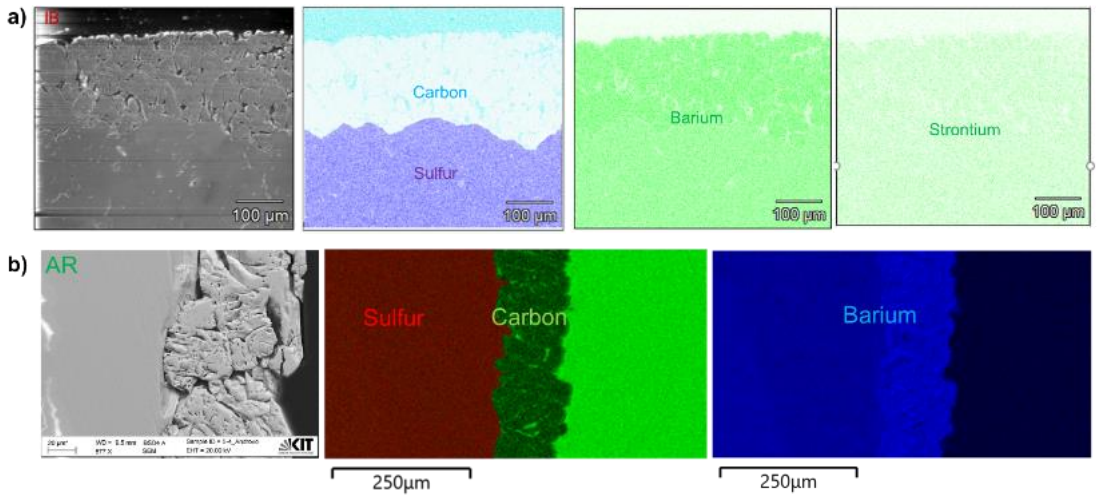

Figure 26. shows SEM-EDX mapping for the two different textures of both types, IB and AR. Both types show a sharp change at the interface of the two textures for sulfur and carbon contents. The Barium content increases slightly in the witherite layer. This due is due to the difference in oxygen content between ($BaSO_4$) and ($BaCO_3$; witherite has fewer oxygen atoms per formula unit). Strontium is equally found in both phases

Furthermore, SEM-EDX scanlines from points in the AR and IB barite bulks throughout the replacement front to the outermost part of the witherite layer revealed changes in composition across the two phases, as seen in Figure 27. The profile of S concentrations for both types dropped sharply at the replacement front, marking the end of the parent barite phase and the start of the witherite overgrowth.

The scanlines for the IB type showed the presence of Sr in both phases, with a small but noticeable increase in the witherite phase (Figure 27). This showed clearly that Sr reprecipitated in the witherite, maintaining a constant level of incorporation throughout the recrystallization process. The Ba profile also showed an increase in the witherite phase compared to the barite phase in both AR and IB, which is due to the change in stoichiometry (i.e. oxygen content) between the phases ($BaSO_4$ → $BaCO_3$). The scanline measurement for C in IB showed an increase in barite region, which could be due surface contamination from sample preparation.

The Sr/Ba ratio, remained constant throughout the two phases, shedding light on the behavior of this trace element during the recrystallization process. This constancy in the Sr/Ba ratio suggested a proportional release and uptake of these elements during the phase transformation.

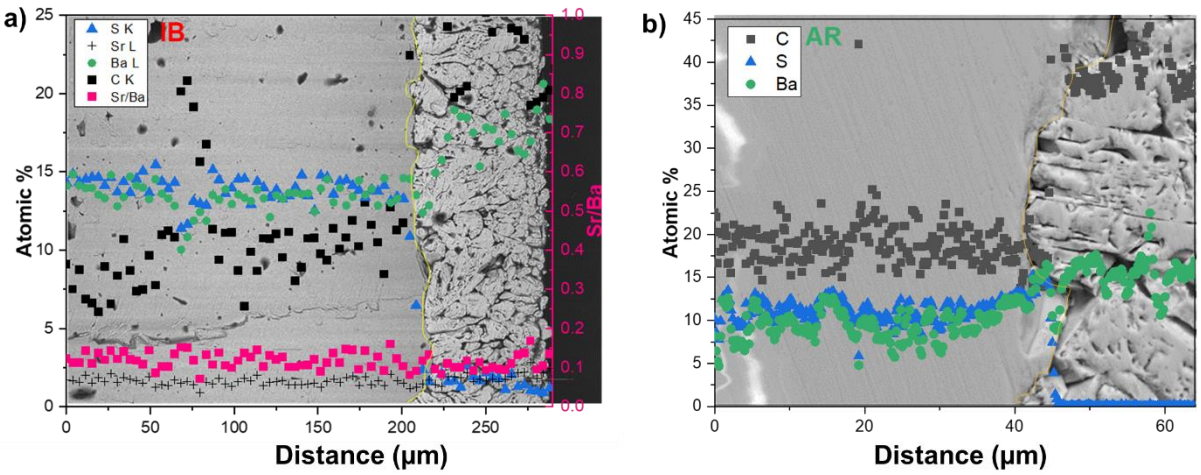

Figure 27. (a) and (b) show SEM-EDX scanlines across the barite witherite interface. The measurements show the sharp transition in composition and the constant Sr/Ba-ratio throughout the two phases cbm IB.

The solution elemental analysis via ICP-OES showed that the Ba concentrations of AR and IB solutions differed where IB concentrations were slightly less than concentrations of AR in early reaction stages, however, Ba in solutions with IB increased around 390 hr of reaction time to be become more than in solutions containing AR as shown in Figure *28*.a. The Ba concentrations for AR leveled off after 200 hr of reaction time, whereas Ba concentrations showed s continues increase. The evolution of Sr concentrations in IB solutions showed an increase seemingly connected with the increase of Ba for IB.

The Sr/Ba ratio (Figure 28.b) obtained from concentrations of Sr and Ba in the solutions over 600 hr reaction time was found to be high as in the first 24 hr of reaction, then decreased sharply afterwards and continued to decrease. Comparing the Sr/Ba ratio in the solid phases for barite and witherite shown in Figure 27, the Sr/Ba in solution was much higher in early stages, but the value became similar to the solid ratio in the very later stages of reaction.

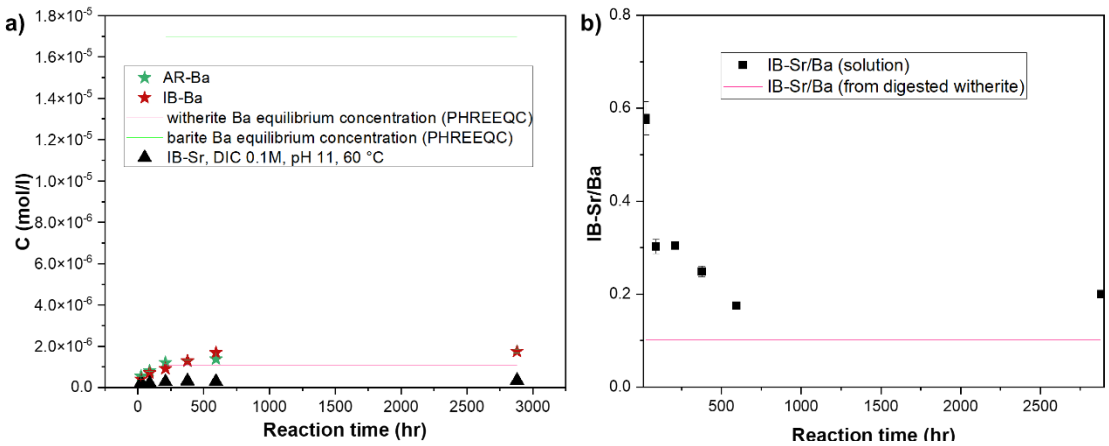

Figure 28. (a) shows ICP-OES analysis for Ba and Sr concentrations in supernatant solutions from the cube experiments. (b) The Sr/Ba-ratio in the solution is higher than the ratio in the solid phase. equilibrium concentrations (obtained via PHREEQC computer code and the PHRREQC.DAT database (Parkhurst and Appelo, 1999))

7.4 The transformation of barite powder into witherite

The five barite types (P, SL, LT-SL, AR, and IB) were reacted with carbonate solutions of varying concentrations (0.01, 0.05, and 0.1 M) and pH levels (9.5, 10, 11, and 11.30 for LT-SL) at 25°C. This reaction resulted in diffractogram patterns with peaks consistent with reference witherite peaks, as shown in Figure 29. Although there was a consistency in the resultant peaks, a shift to higher angles was observed compared to the witherite references. The greatest shift was observed in the IB peaks (Figure 29.d), while the least shift was noted in the AR peaks (Figure 29.c). It is noteworthy that the raw IB barite exhibited a considerable shift in its peaks compared to the reference barite and other barite types (see Figure 16).

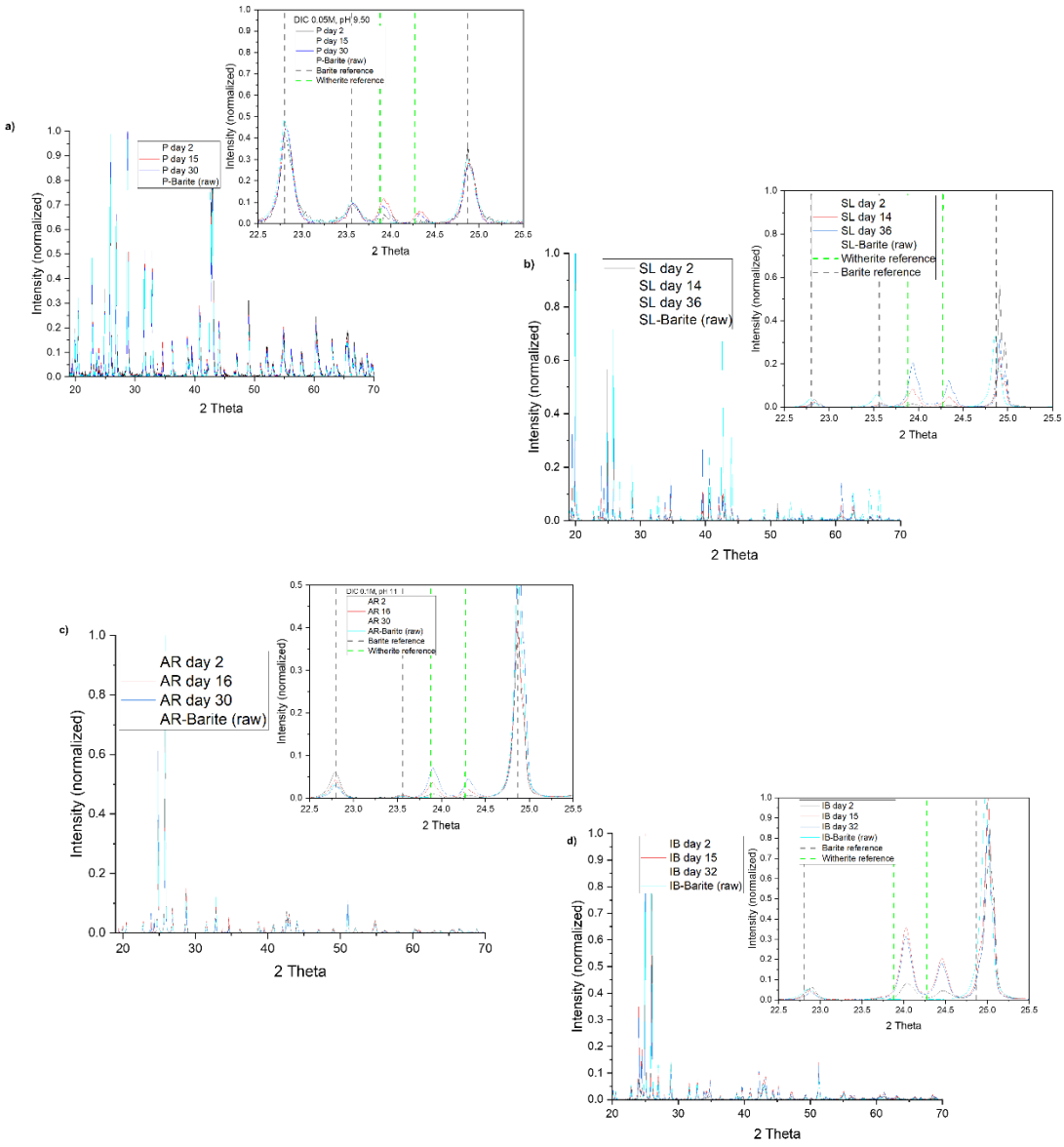

Figure 29. XRD Diffractograms of the different types of barites that were reacted with carbonate solutions of concentration (0.1M) and pH (11) for selected time intervals. In addition, raw (unreacted) barite of each type is shown for comparison. IB shows witherite patterns shift to a higher angle. Reference diffractograms for phases

involved in the reactions (witherite and strontianite references were obtained from Ye, Y., Smyth and Boni 2012, whereas barite and celestine from Antao,

The solid analysis for particles after the reaction with carbonate solution

SEM images for P, SL, LT-SL, AR, and IB particles measured with XRD, displayed in Figure 29, are presented in Figure 30. The reacted P particles exhibited hexagonal shapes with well-defined pyramidal prisms (Figure 30.a), consistent with witherite particle structural shape (see1.3). SL particles also showed hexagonal shapes with pyramidal prisms, but with additional rough layers covering what appeared to be barite particles, and such layer obscured some of the crystallographic features (Figure 30.b). The image shown in Figure 30.c is for SL, but after only 7 days reaction with carbonate and it showed similar hexagonal particles and rough layers observed in Figure 30.b. However, a particle that appeared to hexagonal indicated could have grown underneath the rough layer. The LT-SL particles were similar to the SL particles, displaying hexagonal shapes with pyramidal prisms and rough surface layers that masked the underlying particles structures.

The reacted AR particles maintained hexagonal shapes with pyramidal prisms, with signs of surface dissolution were observed for what appeared to be barite particles, suggesting partial alteration of such particles (Figure 30.e). The reacted IB particles displayed hexagonal bipyramidal shapes, with individual particles attaching to each other in a tip-to-tip pyramid fashion, forming aggregated structures (Figure 30.f). The other IB particles exhibited significant surface dissolution, more pronounced than in AR witherite particles, indicating a higher degree of reactivity with the carbonate solution as highlighted in Figure 30.f.

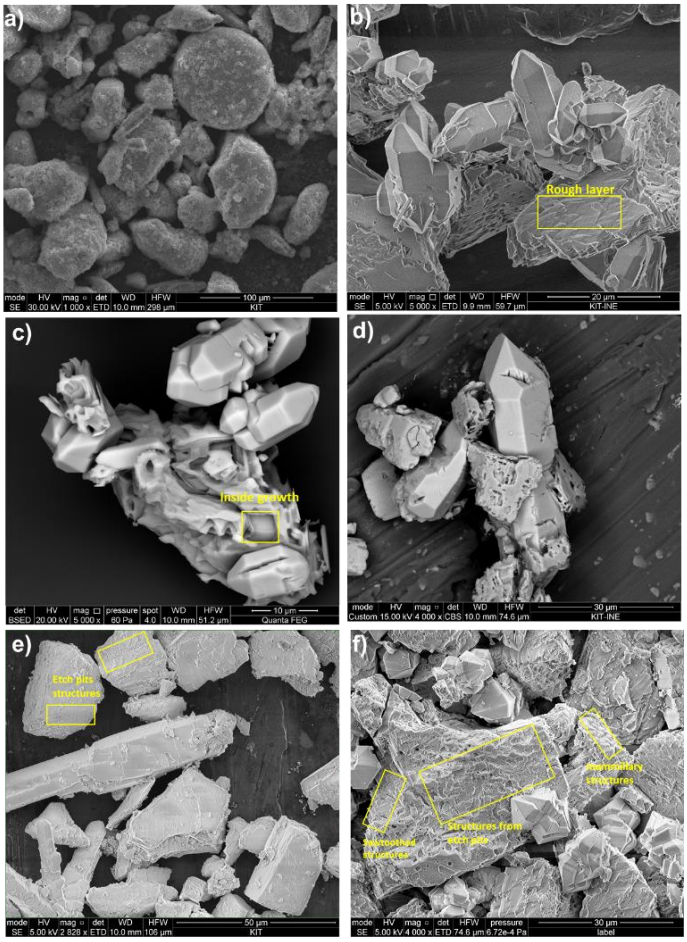

Figure 30. shows SEM images for barite types that were reacted with carbonate solution (0.1M for SL, AR, IB and 0.05M for type P) and pH 11 for SL, AR, IB and 9.50 for P. (a) P type particles after 30 days reaction, where several hexagonal particles were observed, whereas the rest appeared large particles made out of agglomerates of small ones (b) for SL after 36 days reaction with carbonate showing hexagonal particles with smooth surfaces grew very close to other particles that showed rough layers, (c) SL but after 7 days reaction with carbonate that showed what appeared to be an inside growth for a hexagonal particle into the rough layer, (e) and (f) for AR and IB after reacting for 30 and 32 days, respectively; surfaces of both types showed signs of dissolution, with IB being much more sever.

The size distributions of P, SL, AR and IB for the resulted hexagonal particles were obtained from SEM images. They are displayed in Figure 31. The particle size distribution for witherite from type P barite showed distinct distributions in length and width with peaks around 15 µm and 40 µm, respectively, which demonstrates the rod like nature of the particles.

For reacted SL type barite particles, the length distribution was broad, with a maximum between 25 and 30 µm. The width distribution exhibited narrower range around 5 to 20 µm, peaking between 10-15 µm. In comparison with type P resulted particles, SL resulted particles showed in general smaller sizes.

The length distribution of IB resulted particles shows narrow and more evenly distributed compared to other types, with a peak around 14-17 µm. The width distribution showed a peak

around 10-12 µm. The witherite from IB showed the smallest particle size among all experiments.

The particle size distribution for type AR particles shown in Figure 31.d displayed a wide range of particle lengths, most of them were falling between with peaks between 80-90 µm. The width of the particles showed a narrow distribution peaking between 10-20 µm. The particles size for type AR was the largest among all types and the length to with ratio indicates a strong rod-like character.

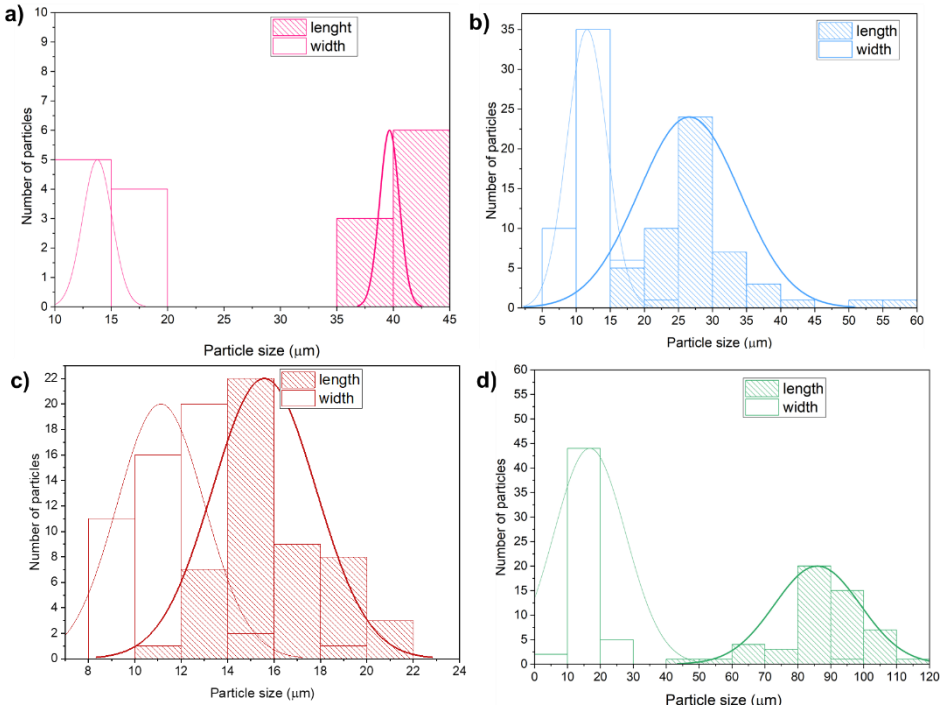

Figure 31. shows the size distributions of the resulted particles obtained from SEM images in Figure 30.a for type P, Figure 30.b for type SL, Figure 30.e for type IB and Figure 30.f for type AR. The figures show the difference between length and width of SL and IB is smaller than P and AR, and that AR has longest particles.

The solid elemental analysis for the particles after the reaction with carbonate solution

SEM-EDX analysis shown in Figure 32 provided elemental information about the particles displayed in Figure 30. Point measurements on hexagonal particles from experiments with types P barite and with LT-SL barite revealed high C counts, as seen in the spectra below Figure 32.a and Figure 32.c, respectively.

The elemental information for types SL, AR, and IB was obtained through elemental mappings. For SL (Figure 32.b), S in red dominated in what appeared to be a barite particle, while C in green dominated in a hexagonal particle. The mapping analysis also indicated significant C presence along the edge of the barite particle, as highlighted in Figure 32.c. Additionally, the mappings showed that the two different mineral phases appear spatially closely attached to each other. The red spot towards the middle of the witherite rod may even be a remnant of the

barite particle from which the witherite started growing. For types AR (Figure 32.d) and IB (Figure 32.e), the mappings revealed a predominance of C (in purple) for hexagonal particles and S (in pink) for other particles.

Based on the XRD patterns (Figure 29), SEM images (Figure 30), and SEM-EDX elemental analysis (Figure 32), it can be concluded that witherite formed after the reaction of barite particles of different types with carbonate solutions. This transformation was evidenced by the similar resultant phase patterns to XRD witherite reference patterns, similar particles structure changes seen in SEM images to known witherite structure, and elemental information of S and C revealed by SEM-EDX mappings.

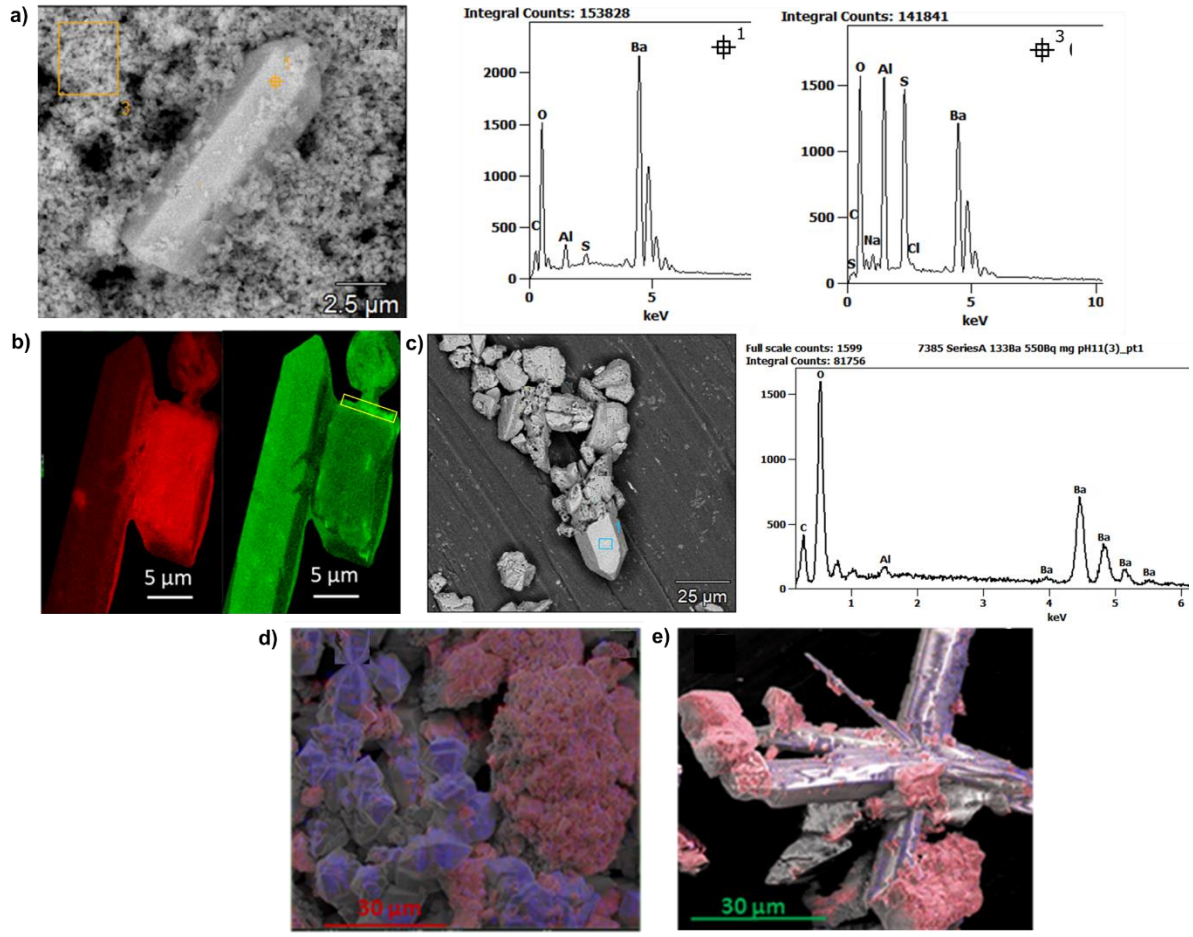

Figure 32. show SEM-EDX elemental analysis for different types of barite that were reacted with carbonate (0.1M) and pH 11 where in (a) besides the image of particles after the experiment with type P barite point measurements were performed at the hexagonal particle as well as at aggregates of the nano-particles. The spectra showed higher C and higher S content, respectively, indicating witherite and barite; (b) was a mapping analysis on powder from experiments with type SL barite. S is indicated in red whereas C is indicated in green. The elongated hexagonal rod showed high content of C whereas the other particle was S rich; (c) was a similar measurement to (a) but after the experiments with LT-SL type barite where a hexagonal particle showed high C content and no S; (d) and (e) were mappings similar to (b) for type AR and IB, respectively, where C was indicated with purple whereas S was in pink.

The FIB-SEM and SEM-EDX analysis for SL witherite particles and rough layer resulted from carbonate reaction

The type SL particles that were reacted with carbonate (0.1M) and pH 11 for 36 days were investigated via FIB-SEM (Figure 33) in order to closer examine growth features that were observed in the resultant particles exhibited as shown in Figure 30.b, Figure 30.c and Figure 30.d . The FIB-SEM cuts were selected at areas which were expected to reveal information on: the rough layer, the growth closeness of witherite particles to the rough layer barite particles and the possible growth of witherite withing barite particle bulks.

A number of witherite particles that appeared to grow attached to barite (Figure 33.a) were undergone FIB cutting polishing segments of the rough layers (Figure 30.b) as well as parts witherite particles (Figure 33.b). The cutting process revealed that there was gap underneath the rough layer all the way to the witherite particles. In addition, it revealed that the witherite particles grew grouped as cluster and possess rather solid surfaces with no observable porosity. The cuts also showed that the witherite particles were in a direct contact with what appeared to be remaining barite. This possibly could be the reason for the observed gap as witherite was consuming dissolving barite.

A direct contact between the witherite and barite particles was also found in a second cut, displayed in Figure 33.c, which showed in elemental mapping analysis (Figure 33.d) what appeared to be a witherite particle (C dominated indicated in purple) growing on top of a barite particle (S dominated indicated in red).

The third cut was for a barite particle covered by a rough surface layer and without separate apparent witherite particles and (Figure 33.e). The removal of the rough layer shown in Figure 33.f revealed what seemed to be a particle with a hexagonal shape, which could suggest that some of the witherite particle grew inside pores within barite particle bulks. Another finding was the revealing of internal porosities appearing as distinct layers within the particle structure, suggesting variations in density and possibly different phases of crystal growth or dissolution events. Such porosities were also found by Weber, J., at el., 2016 who carried FIB-SEM cuts for SL barite particles.

The presence of these internal layers and porosities could be attributed to differential growth rates, where certain layers experienced more rapid crystal growth to others. Additionally, these porosities might have formed due to trapped gases or fluids during the crystal growth phase, leading to the creation of voids within the structure (Weber, J., et al., 2016). The interconnectivity between external and internal porosities (Weber, J., et al., 2017) could be a

mean that facilitated an in-diffusion for carbonate solution into the barite particle that led to the witherite inside growth.

Another observation is that no gap between witherite and barite was found after the removal of the rough layer contrary to what was observed while cutting the particle in Figure 33.b. This could indicate the role witherite played during growth as it led to significant barite bulk consumption, leading to a spatial replacement of barite by witherite.

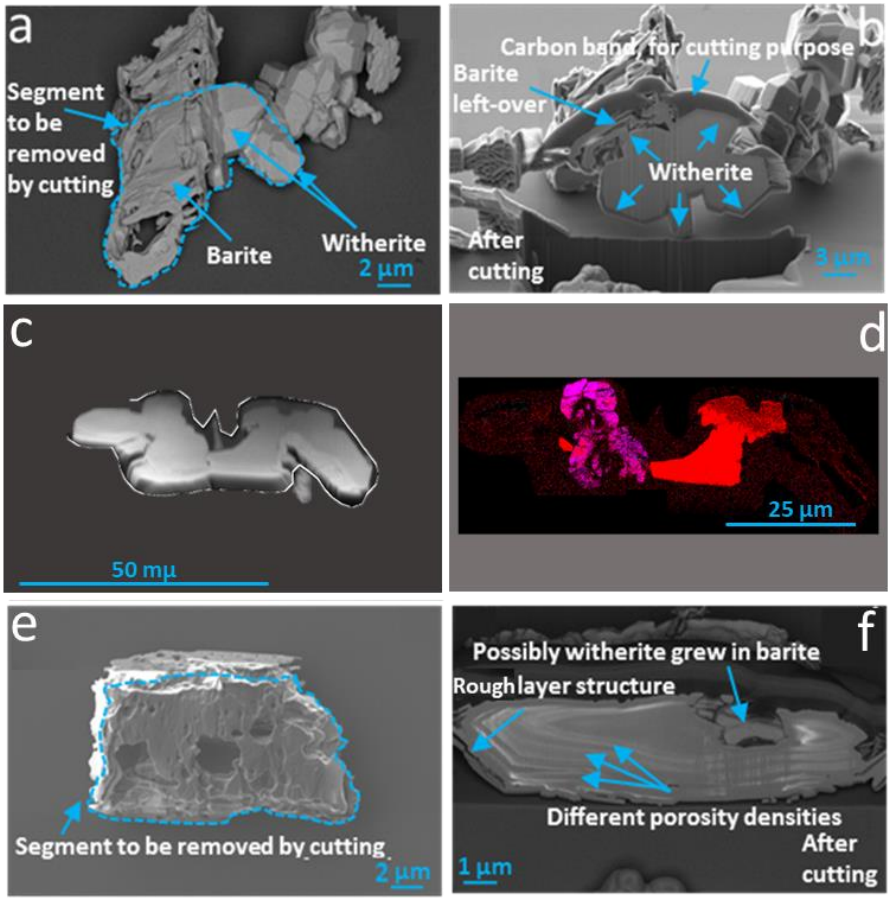

Figure 33. (a) FIB-SEM-ESB image showing a barite SL particle covered with the rough layer and witherite particles underneath it. (b) FIB-SEM-SE2 image of (a) after being cut showing a group of witherite particles and possible remnants of barite. (c) SEM-FSD for a witherite particle adjacent to a barite particle after FIB cutting and (d) SEM-EDX mapping for (c) showed clearly how the witherite particle (red indicates C) grew attached to the barite particle (purple indicates S). (e) FIB-SEM-SE2 for a barite particle covered with a possible witherite rough layer and with holes covering different surfaces of the particle. (f) SIB-SEM-InLens image for (e) post cutting showing a possible witherite growth inside barite, effect of porosity densities and a structure of the rough layer.

The amount of witherite formation was obtained from the diffractograms shown in Figure 29 via the Rietveld Refinement analysis. The amount of witherite formation of each type under different conditions are plotted as a function of time in Figure 34 for carbonate concentrations (0.1M) at pH 10 and 11. The plots of data obtained for experiments under other conditions are shown in Figure A.2.

Witherite formation rates for the different barite types

The amount of witherite formation was obtained from the diffractograms shown in Figure 29 via the Rietveld Refinement analysis. The amounts of witherite forming from each barite type under different conditions were plotted as a function of time as shown in Figure 34 for carbonate concentration (0.1M) and pH 11 for type SL, IB and AR as well as (0.05M) and pH 9.50 for type P. The plots of the rest of the conditions are shown in Figure A.2.

It is clearly seen that rates of witherite formation were influenced by the barite type reacted with carbonate. Among all four types of barites, SL showed the highest transformation to witherite for the different experimental conditions. This could be attributed to the distinct morphological and structural features such as the particle size, the intergrown particulates, external and internal porosities that were shown in 7.2.1 and in Figure 33.f.

The IB type barite reveals the second highest witherite formation for different experimental conditions (except for 0.05M and pH 9.50) after the SL type barite as can be seen in Figure 34 and Figure A.2. The high witherite formation observed for the IB barite, being higher than that for AR, could be due to the relatively small particles and to the roughness and the presence of Sr (see 7.2.1) which could also play a role for the dissolution of IB barite particles.

The witherite formation rates found for AR barite were the lowest among all the types as seen in Figure 34 and Figure A.2. This could be the result of the low dissolution rate of AR barite particles since AR appears to be the most stable solid phase among all other types due to its high crystallinity according to the findings shown in 7.2.1. In addition, the AR barite has the largest particle size (Figure 17) and thus a low specific surface area, which will be also responsible for a slow barite dissolution.

For only experimental condition of carbonate concentration (0.05M) and pH 9.50, The P barite transformation was only investigated at only one carbonate concentration (0.05M) and pH 9.50, and for this condition it showed the second highest witherite forming rate after that found for SL barite. The small, nano-sized particles of the P barite (Figure 15) and its poor crystallinity (Figure 16) is certainly responsible for reactivity and in turn for the increase of dissolution rates.

The effect of carbonate concentrations and pH values on witherite formation

Increasing the carbonate concentration results in increasing transformation rates for all barite types as Figure 34 shows. The high transformation and growth rates resulted from higher supersaturation levels at high carbonate concentrations. In addition, the high concentrations of

dissolved CO_3^{2-} can create steeper concentration gradients that enhanced witherite formation by increasing mass transfer. The high carbonate concentrations shift the reaction equilibrium towards more consumption of $Ba^{2+}$and the formation of witherite. Notably in the case of the large AR barite particles no witherite formed at the lowest carbonate concentration (0.01 M) due to low barite dissolution rates and thus local undersaturation conditions with regard to witherite.

The effect of pH on the transformation rates was clearly observed in Figure 34. The higher the pH value, the higher was the transformation rate because the CO_3^{2-} ion concentration (increasing with increasing pH) were the main contributor to the transformation reactions.

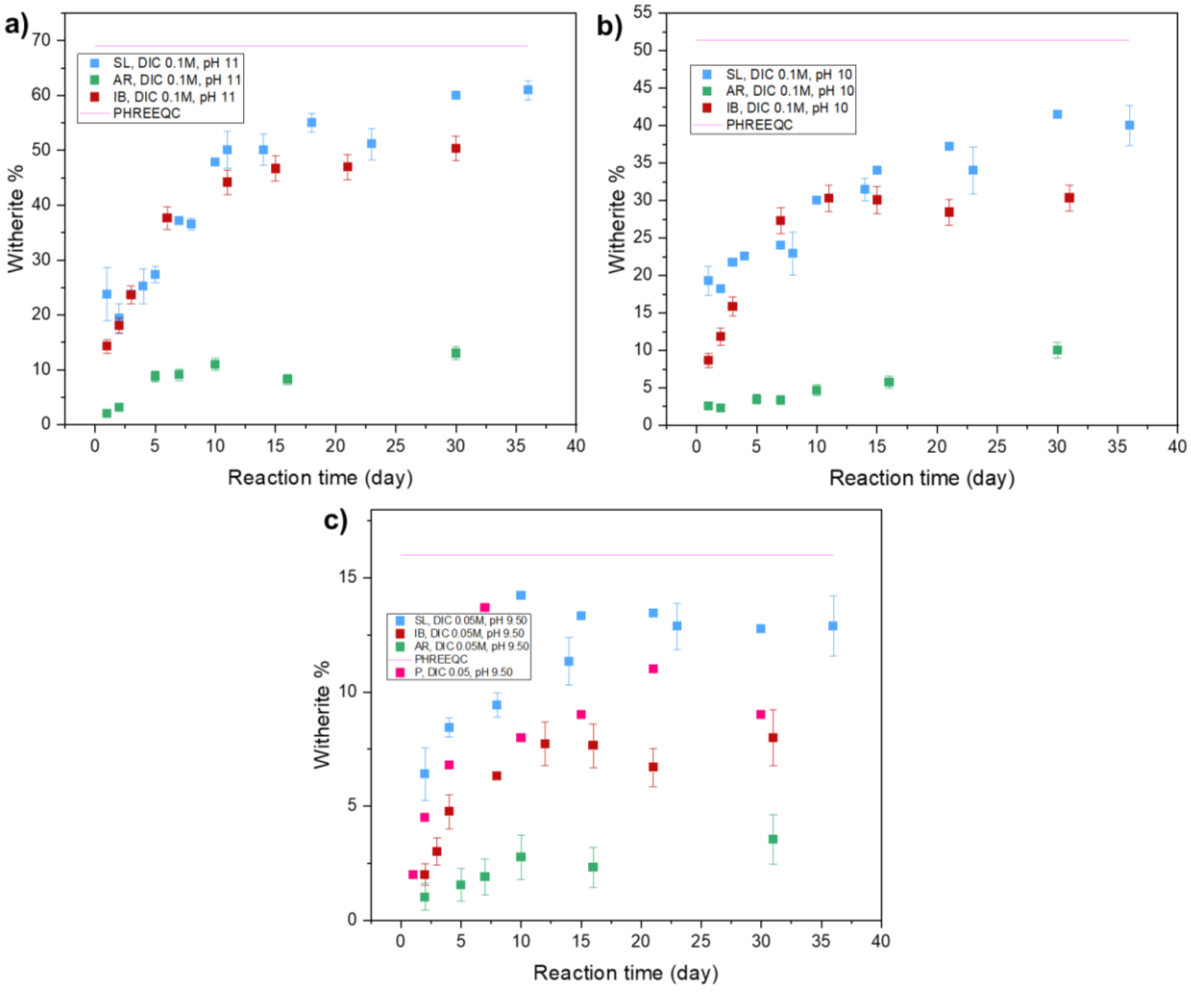

Figure 34. shows the witherite formation percentages that resulted from reacting different types of barites with carbonate solutions (0.1M) at pH 10 and 11, and carbonate concentration (0.05M) at pH 9.50. The percentages were obtained via Rietveld refinement analysis from diffractograms, whereas theoretical witherite formations for the different conditions was calculated via PHREEQC (Parkhurst, D. L., & Appelo, C. A. J. 1999). The witherite formation for SL type is consistently the highest / fastest, while AR consistently shows the lowest reactivity. The witherite formation for all types and conditions did not reach the theoretical formation limit.

The solution analysis in carbonate reaction experiments

The Ba concentration in solutions containing barite types SL, IB at 0.1 M carbonate and at pH 11 decreased gradually over the reaction time approaching the equilibrium with witherite as shown in Figure 35.a.

The Ba concentration for type IB was higher than type Ba concentration of AR throughout the reaction time, leading AR to attend equilibrium with witherite more rapidly. This is in line with solid observations as IB particle surfaces showed more sever dissolution effects compared to AR surfaces (Figure 30.e and Figure 30.f). In addition, it is in line pointed with higher witherite formation IB showed compared to AR (Figure 34) as more Ba abundancy could allow for more witherite formation.

The SL type showed higher witherite formation than AR, which was expected due to the difference barite particle characteristics between the two (see 7.2.1). This higher Ba concentrations for SL compared to AR allowed for more Ba becoming available for witherite formation reaction as can be seen in (Figure 34). However, the Ba concentration in experiments with SL barite was found to be lower than in presence of IB though more witherite formation was found in samples with SL barite . This could point towards the role of the rough surface layer observed by SEM possibly hindering Ba from being released fully into the bulk solution.

The Ba concentration for type LT-SL was rather low throughout reaction time, though it showed a slight increase in later stages. This could be attributed to fact type was treated for long time, which negativity affected its particle reactivity as can be seen in 7.2.1 that contains details on intimal LT-SL characteristics.

The evolution trend of Sr for IB type was rather similar to Ba trend as can be observed in Figure 35.a. This led to similar Sr/Ba ratios in the solutions during reaction time as exhibited in Figure 35.b. These ratios were compared with Sr/Ba ratios that were obtained via SEM-EDX elemental analysis point measurements for initial IB barite (Figure 15.e) and for the IB resultant witherite particle (Figure 30.f). The Sr/Ba solution ratios were found to be in line with Sr/Ba witherite ratios and the upper value for Sr/Ba initial IB barite ratios.

Unlike Sr/Ba solution ratios in IB cubes, Sr/Ba ratio in the solution was rather close to the ratio in witherite particles as well as the unreacted IB barite. This indeed indicated a factor that led to similar Sr/Ba ratios between solids and solutions for IB particles or a factor that led to the discrepancy between the two ratios for IB cubes.

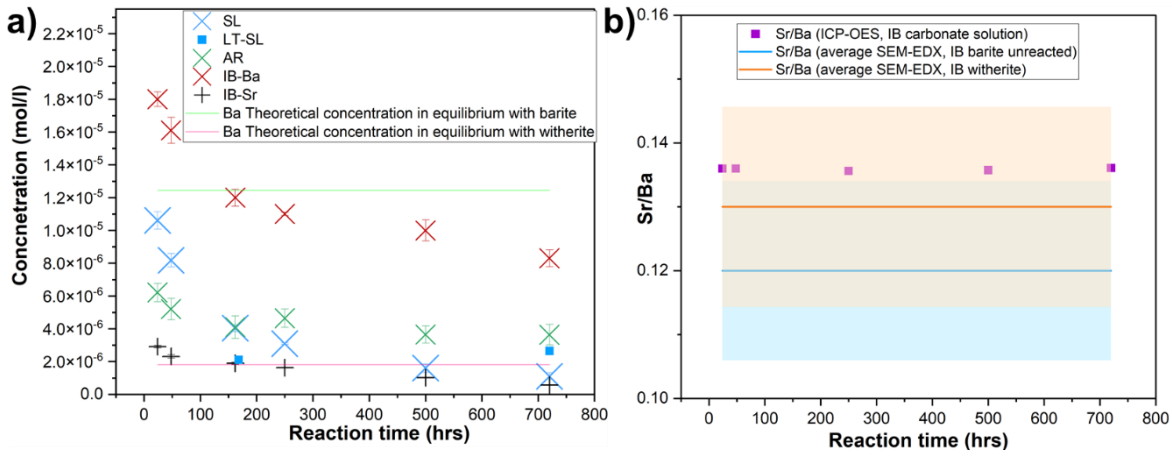

Figure 35. shows ICP-OES results for Ba concentration evolution over different reaction time intervals for different barite types and Sr for IB type to reveal Sr/Ba ration and compare it with ratios obtained from SEM-EDX results. Ba concentration for SL type drops even below Ba equilibrium concentration, whereas IB and AR are decreasing in the same manner but IB Ba concertation is much than AR. The Sr concentration is changing by decreasing over time following similar to the trend of Ba if IB type. (b) shows that the Sr/Ba in the solution is very close to the ratio in the solids.

7.5 The reaction of barite powder with carbonate in the presence of ^{226}Ra

Transformation of Ra containing SL barite into witherite

The reaction of carbonate solutions with concentration (0.1M) and pH 10 and 11 with long treated SL-Ra particles with different ^{226}Ra concentrations did not result in witherite formations as SEM analysis in Figure 36 revealed. The inspection of the SEM images showed no hexagonal shapes that is associated with witherite particles observed before (see Figure 30.b). In addition, the rough layer that was found before to be associated with the formation of witherite particles, covering barite particles for SL type (Figure 30.b) did not form here. The particles for all batches did not show significant changes in terms of morphology, preserving to a great extent their features that they possessed before reacting with carbonate (see Figure 18). The absence of witherite formation could be due to the influence of the long time treatment with ^{226}Ra on particles reactivity. As already shown before (see 7.2.2), the long treated particles showed significant changes in terms of morphology and most likely the internal structures compared to the fresh SL, which could be the reason for no witherite formation to be observed.

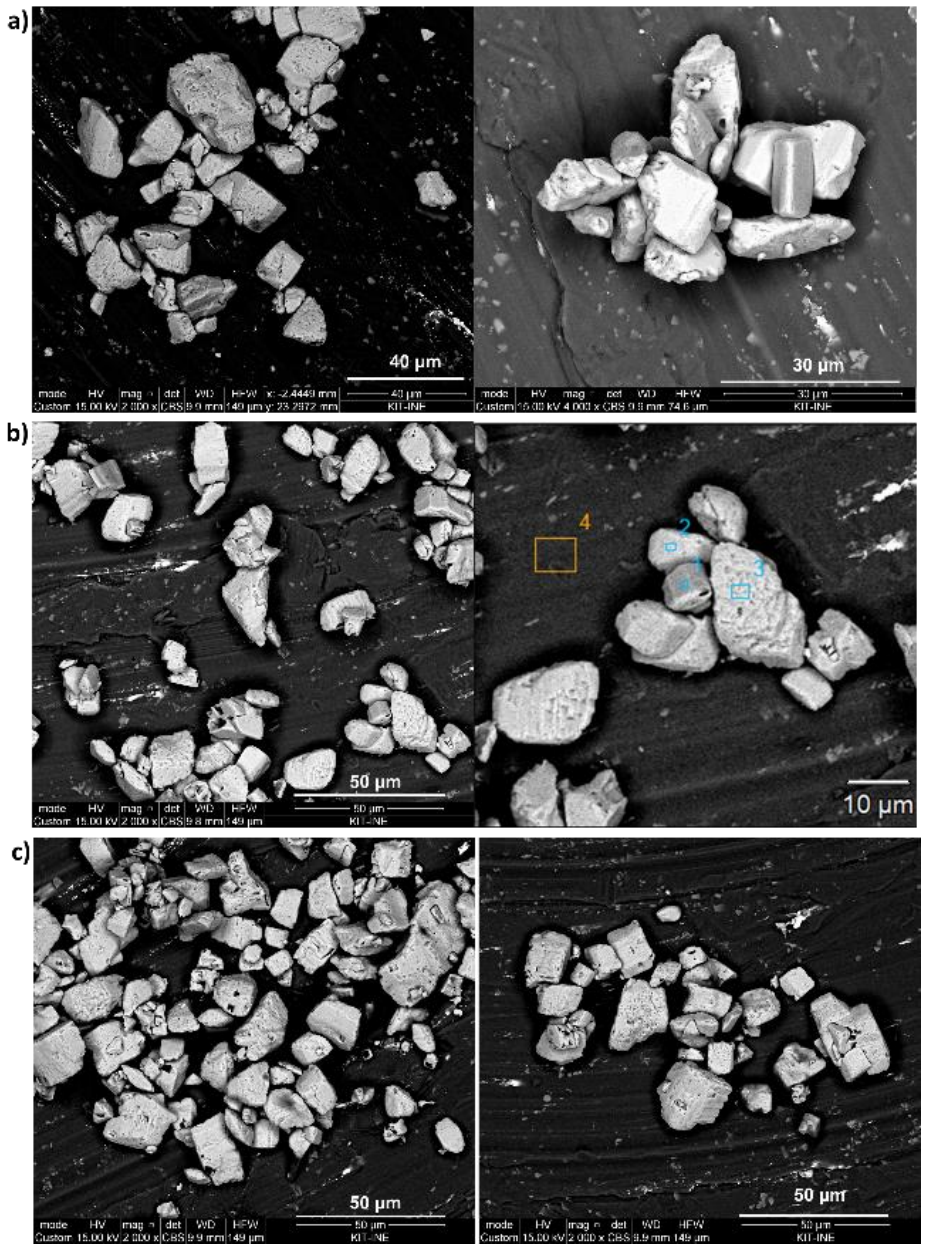

Figure 36. shows particles after reacting with carbonate for 30 days where (a) particles from batch D1, (b) particles from batch E1 and (c) particles from batch F1.

The XRD analysis confirmed the absence of witherite formation (Figure 37). The diffractogram peak intensities for solids of the E2 and F1 batches shown in Figure 37.b and Figure 37.c exhibited less intensities compared to non-carbonated particles. This decrease of peak intensities of carbonated barite particles could be attributed to an initiation of a dissolution process that affected the order of the crystals as they reacted with carbonate solution.

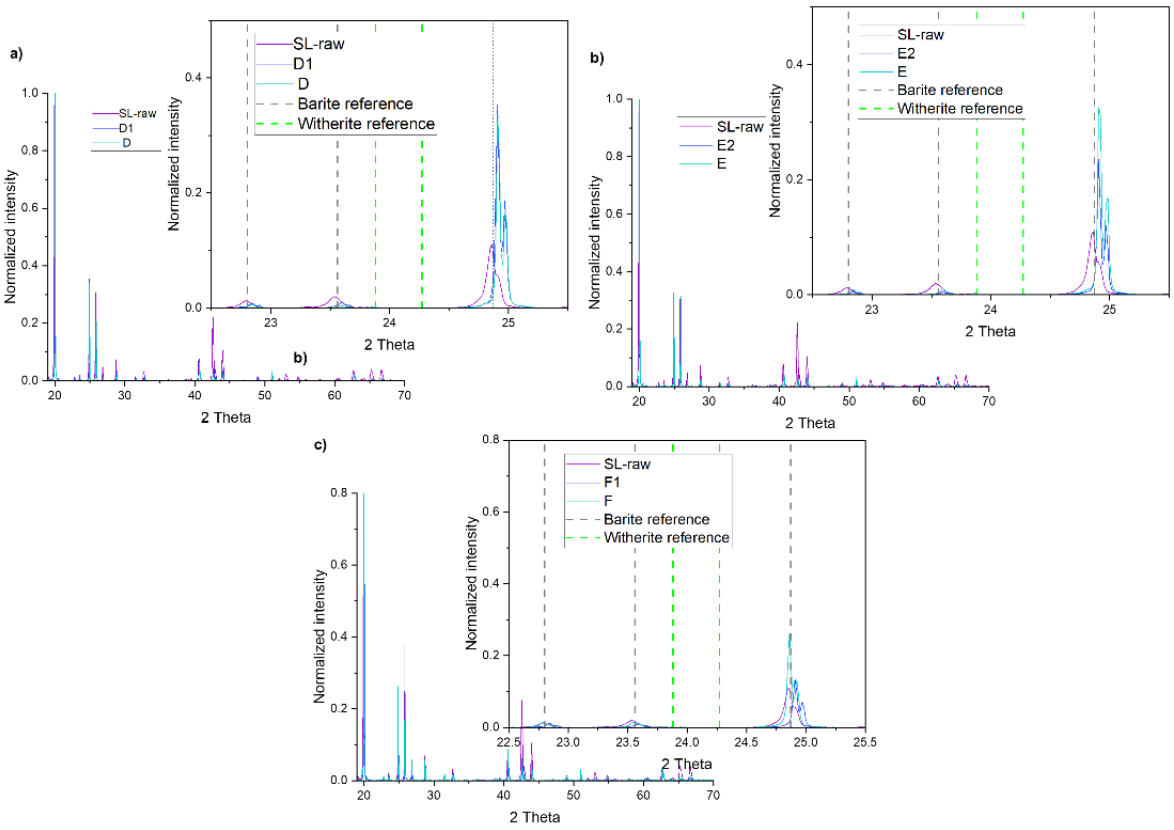

Figure 37. XRD Diffractograms for batches of ^{226}Ra long treated particles after 30 days reaction with carbonate. The particles Diffractograms before carbonations are shown as well. Witherite phase reference was shown here was obtained from Ye, Y., Smyth, J. R., & Boni, P., 2012.

The attribution of the particles XRD peak intensity decrease to particle dissolution is supported by the evolution of Ba concentration in solution displayed in Figure 38. The Ba concentration increased over the course of the four week reaction time, indicating that dissolution reactions were ongoing during this period. However, this increase in Ba concentration was relatively slow, remaining approximately one order of magnitude below the equilibrium concentration for Ba in equilibrium with barite, even after four weeks of reaction time. This slow release of Ba into the solution suggests a low reactivity of the particles, which likely contributed to the absence of witherite formation.

For comparison, a similar Ba concentration trend was observed in the previously shown LT-SL barite sample (and shown in Figure 38), yet witherite formation occurred despite the comparable conditions. It is important to note that the Ba concentrations in both experiments approached the equilibrium concentration for witherite. However, the presence of ^{226}Ra in the current experiment seems to have played a significant role in negatively affecting the reactivity of the SL barite particles, preventing witherite formation.

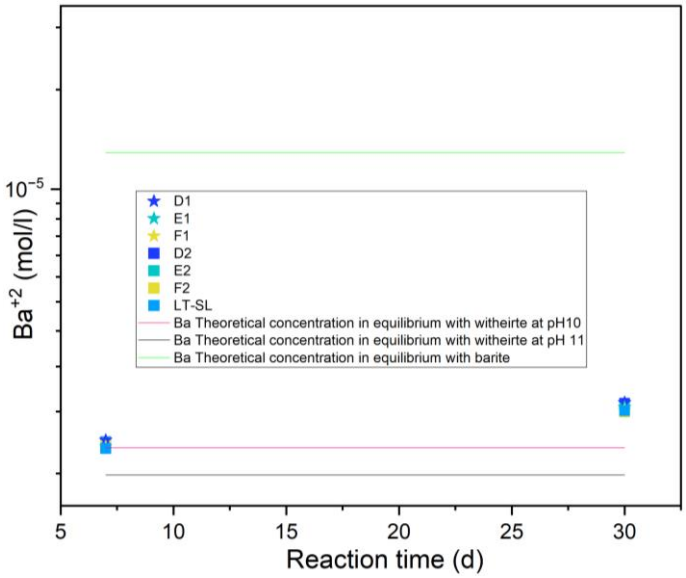

Figure 38. shows the evolution Ba for long ^{226}Ra-treated particles during carbonation process. The concentrations of Ba for all the particles reacted with carbonate for pH values (10 and 11) are showing an increase over the course of the reaction. The Ba concentrations for all batches with pH (10 and 11) are below equilibrium concentrations (obtained via PHREEQC computer code and the PHRREQC.DAT database (Parkhurst and Appelo, 1999)). LT-SL that was treated as same as D, E and F but with absnce of ^{226}Ra that resutled in 7% witherite is shown here for compersion.

7.6 Barite precipitation in the presence of ^{226}Ra

The addition of sulfate carrying solution to the barium solution and Ba/^{226}Ra solution of RB series batches at 60°C resulted in the production of particles with dendritic morphology as shown in Figure 39. The dendritic morphology of particles appeared not to be affected by the presence ^{226}Ra as particle shapes in Figure 39.b and Figure 39.a are very similar.

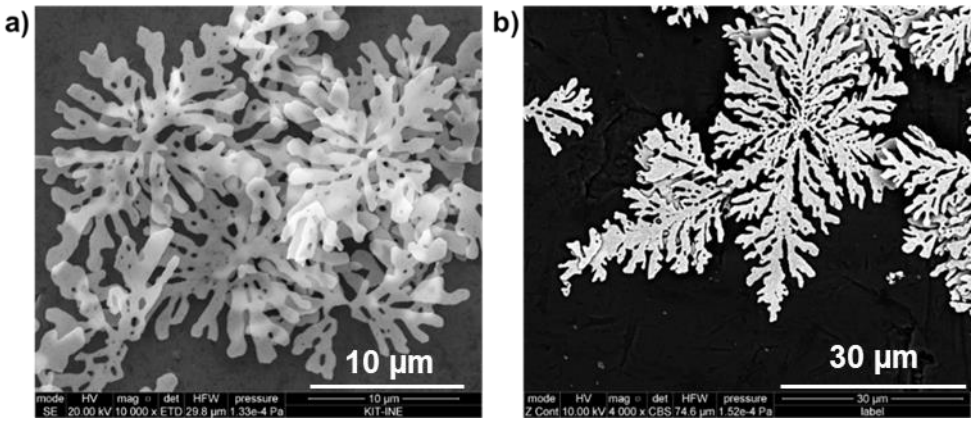

Figure 39. SEM images show the formation dendritic particles after the addition of Na_2SO_4 solution (0.1M) to $BaCl_2$ solution in (a) the absence ^{226}Ra and (b) the presence of ^{226}Ra.

To examine the nature of these particles, elemental SEM-EDX point measurements were performed and revealed that they consist of barite as the atomic ratios of barium and sulfur were rather close as can be seen in shown in Figure 40.

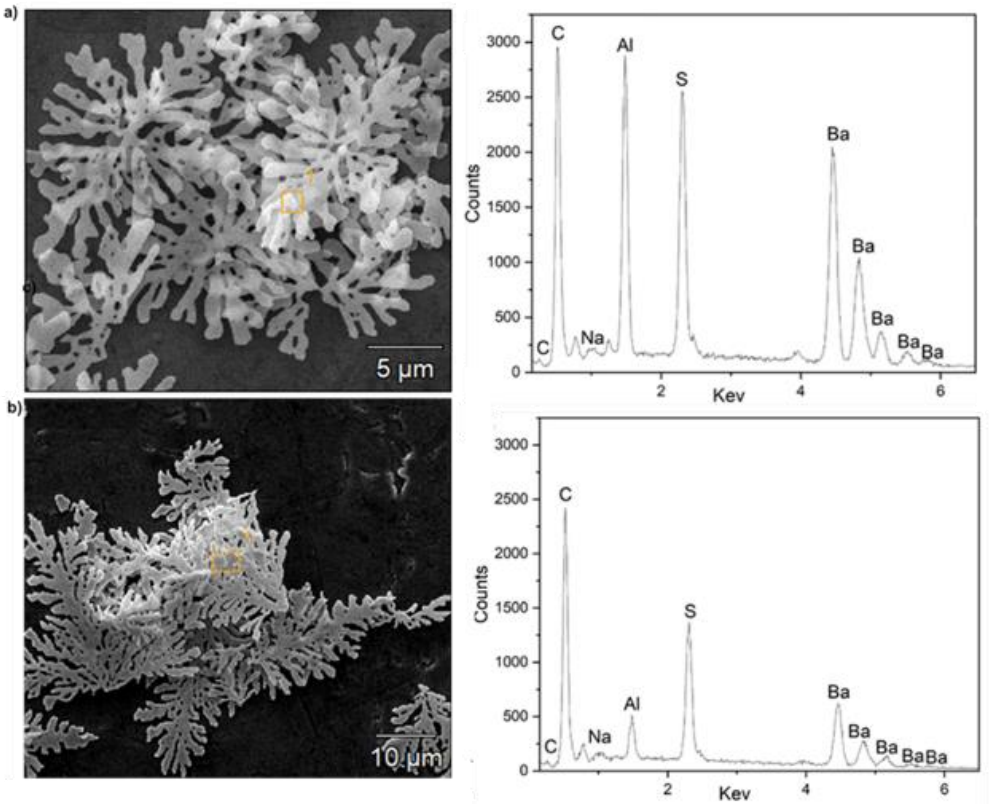

Figure 40. (a) and (b) show points of SEM-EDX elemental analysis for precipitated barite in (a) the absence of ^{226}Ra and (b) the presence ^{226}Ra and their corresponding spectra, which revealed that the phase of the dendritic particles was barite as the sum of the counts of sulfur and barium were rather close. The peak of Al was most likely from the aluminum sample wafers as the dendritic particles were thin with lots of porosity that allowed to measure Al underneath them.

The saturation index with respect to barite for the given conditions shown in the experimental details (see 5.2.2) was 7.65 as calculated via PHREEQC code (Parkhurst, D.L., & Appelo, C.A.J., 1999) and the Nagra/PSI thermodynamic database (Hummel, W., et al., 2002). This corresponds to a high supersaturation level with respect to barite, which could lead along the elevated temperature (60°C) to the formation of particles with dendritic shapes. The dendritic particles showed a high degree of porosity, indicating a rapid formation due to high supersaturation level. It is evident that the composition of a solution being in contact with such a solid phase does not correspond to that of crystalline barite.

The diffractograms of barite and Ra-barite dendritic particles (Figure 41) revealed that while some XRD patterns of the dendritic particles exhibited relatively low peak intensities, the 2 Theta positions remained consistent with reference barite. This confirms the formation of barite, with the variation in peak intensities likely due to preferential crystallographic orientations influenced by the high supersaturation levels during particle formation.

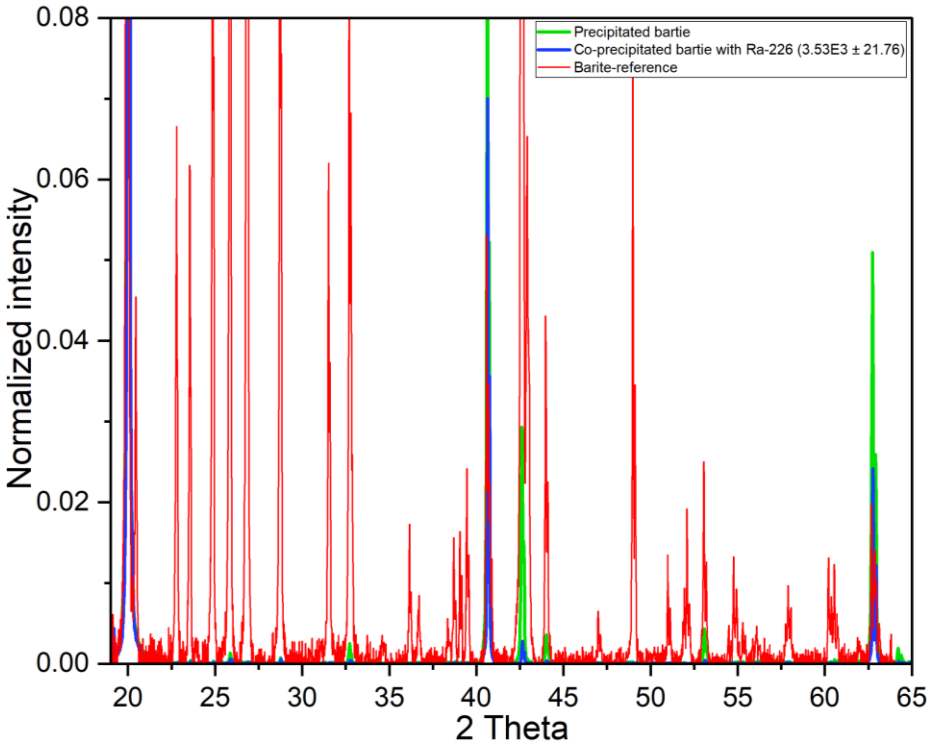

Figure 41. XRD patterns for precipitated barite, barite precipitated in the presence of ^{226}Ra, and a barite reference (Antao, S. M. 2012).

The analysis of the of solutions from the different RB series showed considerable ^{226}Ra removal from the solution after 25 days reaction time (Figure 42), indicating ^{226}Ra uptake in $(Ba, Ra)SO_4$ solid solutions in the precipitated solids of batches RB1-RB5.

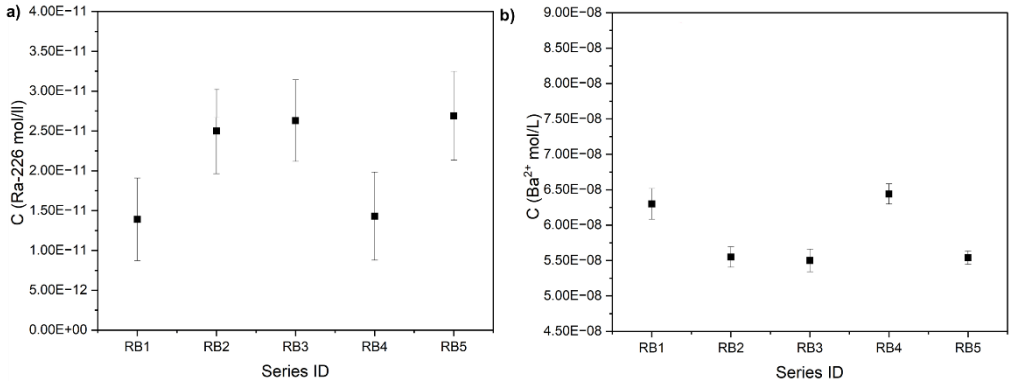

Figure 42. final concentrations of ^{226}Ra and Ba in for barite precipitation batches. Initial spiked ^{226}Ra concentration was ($4.28 \cdot 10^{-7}$ mol/L), whereas Ba concentration was ($8.56 \cdot 10^{-7}$ mol/L)

The removal of ^{226}Ra from the solution during precipitation was accompanied by a decrease of Ba concentration in solution as shown in Fig. 47.b.

The experimental partition coefficient ($D_{exp.}$) for Ra into barite was obtained using Equation 24, and was found to be (0.34 ± 0.14). This shows that ^{226}Ra under current study condition has a preference to be in the solution rather than being incorporated into the solid barite phase. This

value of the partition coefficient is consistent with thermodynamic expectations considering the experimental conditions during the first 6 days of the reaction time where the solution was heated to at (60^0C).

7.7 $(Ba, Ra)SO_4$ barite transformation into witherite

The addition of the carbonate solution (0.15M) and pH 11 to dendritic ^{226}Ra-barite particles in the RB series showed formation of witherite, but in a rather slow pace. As can be seen in the diffractogram patterns in Figure 43, some witherite peaks were observed in the batch that was terminated 21 days after the start of the reaction. After 44 days of reaction, the witherite peaks were still about the same intensity that was observed on the day 21. This could hint at the slow kinetics of witherite formation under these conditions, suggesting that the recrystallization process is not significantly progressing beyond the initial stages within the given timeframe.

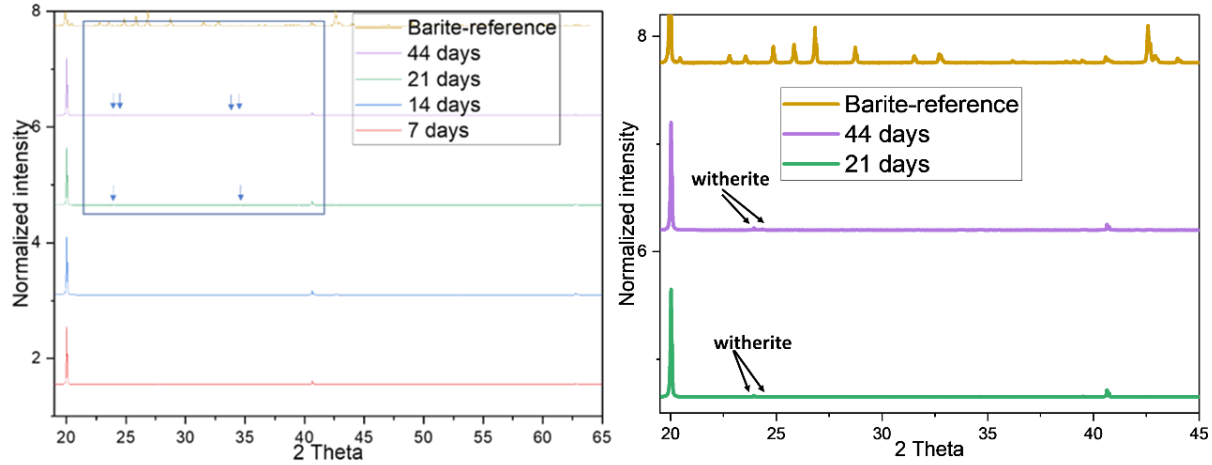

Figure 43. XRD patterns for dendritic barite that was precipitated in the presence of ^{226}Ra are shown here after reacting with carbonate solution (0.15M) and pH 11 for different time intervals over 44 days. Witherite started forming after 21 days of reaction with carbonate and continued to grow throughout 44 days reaction time as pointed out with arrows. Due to witherite insignificant peaks, they are magnified for better visualization. Barite reference was obtained from Antao, 2012, whereas witherite reference is from Ye, Y., Smyth and Boni, 2012.

The SEM-EDX point measurement analysis in Figure 44 for the 21 days and 44 days batches on hexagonal particles revealed that such particles contained no S but C as well as Ba, further confirming the XRD results by indicating witherite formation.

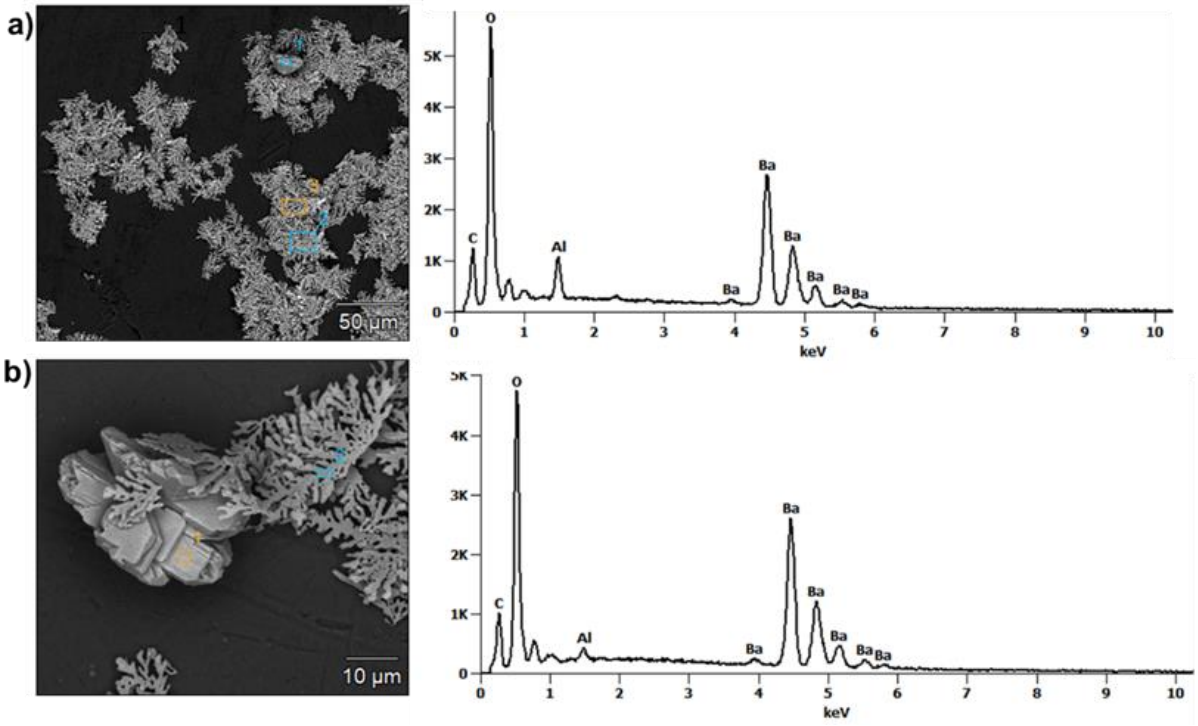

Figure 44. SEM-EDX elemental analysis of point measurements for hexagonal particles of (a) batch RBC 3 (21 reaction time) and (b) batch RBC4 (44 day reaction time). The spectra of (a) and (b) showed carbon, oxygen and barium with the absence of sulfur in the spectra confirming formation of witherite. The peak of Al was most likely from the aluminum sample wafers.

The SEM images at various time intervals reveal witherite growth (Figure 44). After 14 days of carbonation, the sample exhibits only dendritic barite particles with no significant morphological change from the initial ^{226}Ra precipitated barite shown in Figure 43, suggesting that witherite formation did not yet substantially start.

After 21 days of carbonation, the SEM images showed the presence of both dendritic barite particles and a few hexagonal shaped witherite particles (Figure 45.c). These hexagonal witherite particles appeared to have remnants of dendritic barite structures, which could suggest that witherite was forming on the surfaces or within the existing barite dendrites. This combined morphology could point towards the slow transformation process pointed put before, where witherite formation likely was occurring within the pre-existing barite proximity.

At 44 days of carbonation, SEM images continued to show a mix of dendritic barite particles and more pronounced hexagonal witherite particles (Figure 45.d). The hexagonal witherite particles in this batch display a different morphology than usual typical witherite forms. They appeared to grow in a layered or sheet like manner by overlapping and stacking upon one another. This unusual growth pattern may be indicative of the extended interaction time of barite particles with the carbonate solution, potentially leading to secondary growth processes of witherite.

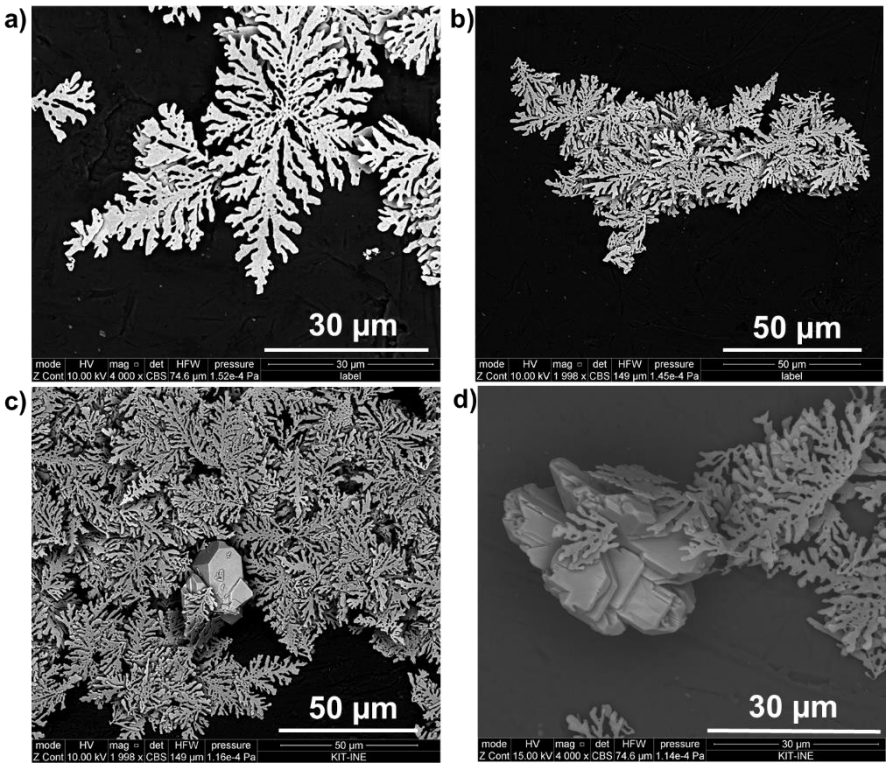

Figure 45. SEM images for dendritic barite after reacting with carbonate solution (0.15M) and pH 11 for different reaction periods where (a) and (b) for batches RBC1 (7 days reaction time) and RBC2 (14 days reaction time) showing no witherite particles. Witherite formation started to be observed after 3 weeks reaction time as in (c)and after 44 days as in (d). (c) clearly showed what seemed to be dendritic particles left over at the surface of a witherite particle and (d) showed what seemed to be witherite particles growing over a barite dendritic particle.

The solution concentration of ^{226}Ra in the batches of series RBC shows insignificant changes over the course of reaction time, as demonstrated in Figure 46.a. The average activity of ^{226}Ra released from barite into the solution after the reaction with carbonate is (12.6±0.8 Bq/ml) for the different batches. This release is minimal compared to the specific activity of ^{226}Ra in the barite (342 ± 21 Bq/mg), which indicates the stability of ^{226}Ra in barite. This is consistent with the results obtained from the solid analysis using XRD and SEM, which showed insignificant witherite formation even in the later stages of the reaction time.

The analysis of Ba concentrations in the solutions further indicates the existence of an equilibrium, as the concentrations show no significant change over the course of the reaction time (Figure 46.b). The Ba concentrations are more than an order of magnitude lower than the barite equilibrium concentration calculated via the PHREEQC code (Parkhurst and Appel,1999) and ThermoChimie-TDB database (Grivé, Mireia, et al., 2015), suggesting that the barite dissolution is rather slow. The ^{226}Ra / Ba solution ratio of different RBC series batches for the given reaction time remains relatively constant as Figure 46.c shows. This

consistency could be indicative for a congruent dissolution of ^{226}Ra/$BaSO_4$ during the reaction with carbonate solution.

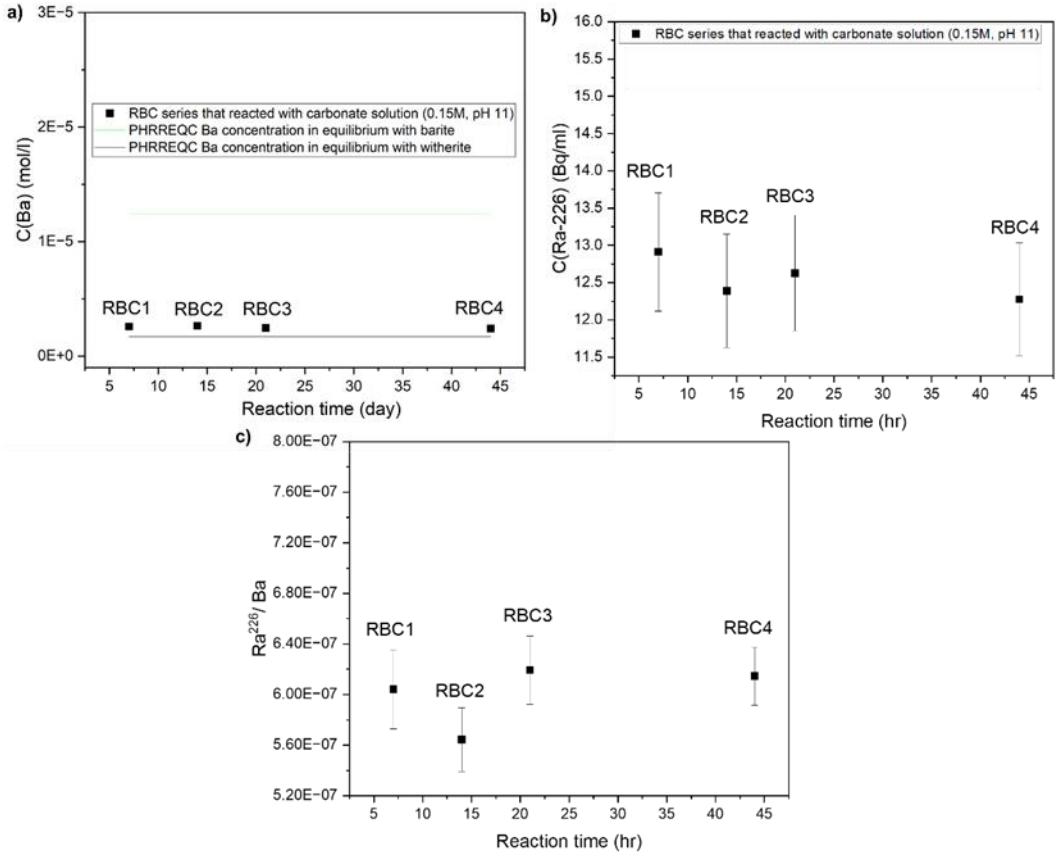

Figure 46. (a) shows the concentration of Ba in solutions for the given timeframe, which is almost constant to , lower than Ba equilibrium concentration with barite and a bit higher than Ba equilibrium concentration with witherite, (b) shows activity of radium for different time intervals over 44 days reaction time, which appear to constant as well and (c) shows similar ^{226}Ra / Ba ratios throughout the 44 day reaction time. Theoretical Ba concentration obtained via PHREEQC calculation (Parkhurst and Appelo, 1999) and ThermoChimie-TDB database ((Grivé, Mireia, et al., 2015).

7.8 The precipitation of witherite in the presence of ^{226}Ra

The RW series of the precipitation of witherite and witherite in the presence of ^{226}Ra, experiments that were carried out through the addition of carbonate carrying solution to the barium-radium solutions, resulted in XRD patterns with peaks that were consistent with witherite reference pattern peaks Figure 47.

The XRD analysis of witherite and $(Ba, Ra)CO_3$ reveals distinct yet subtle differences in the crystallographic properties of the resultant solids. The diffraction patterns of both $(Ba, Ra)CO_3$ and witherite display similar peak positions, indicating that the incorporation of ^{226}Ra does not significantly alter the basic crystal structure of witherite (Figure 47).

While the overall peak positions remained consistent, variations in peak intensities are observed, particularly at higher diffraction angles. The pattern of W exhibited greater peaks

intensities compared to RWs peaks, likely due to the lower amount of solid measured for safety precautions. Despite this, the peaks at lower angles (19.48^0 and 19.89^0) showed comparable intensities between W and RWs. Furthermore, solid phases in RW1 and RW2 experiments showed increased peak intensities at angles (19.48^0 and 24.24^0) compared to both RW3 and RW4 as well as W solids, suggesting possible influence of ^{226}Ra on witherite structure.

Comparisons with reference witherite patterns show that both RWs and W had diffraction patterns that are largely similar to the reference, with minor reductions in peak intensities at angles (27.67^0 and 34.08^0). These minor deviations could hint at a possible slight crystallographic orientation differences.

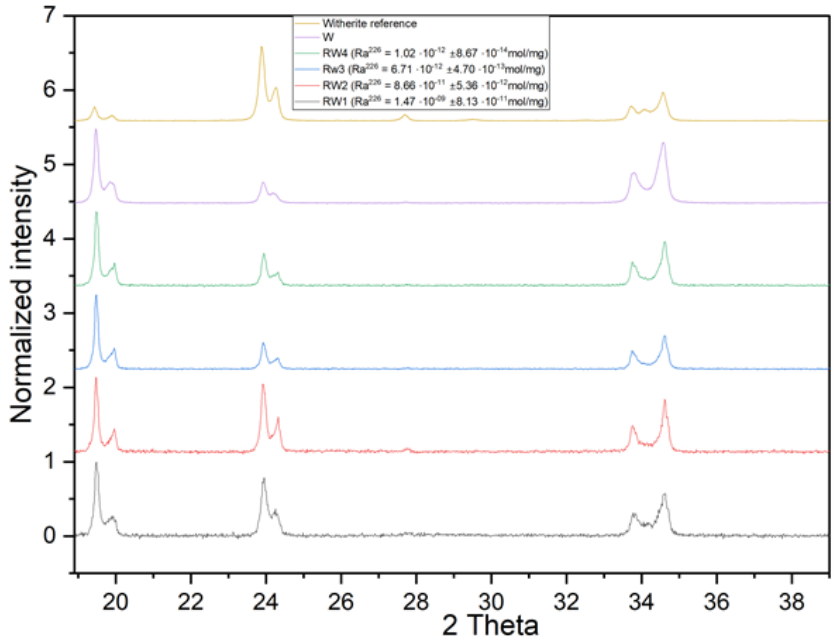

Figure 47. XRD patterns for precipitation of witherite in the presence and absence of radium compared with a witherite reference from Ye, Smyth and Boni, 2012.

The SEM images (Figure 48) showed larger particles with a size of some micrometers that clearly exhibited hexagonal prismatic structures; the large particle exhibit tiny particles loosely associated with their surfaces.

The other particles were nanometers in size and showed prismatic features as well though not as clear as the large ones; this shape unclarity was related to the fact that these small particles were attached to one another and to the large ones, in a back-to-back attachment style leading to masking the bipyramidal ends that revealed the distinct shapes of witherite and other analogues aragonite mineral types. The back-to-back attachment led to the formation of rod like shapes. A close inspection into these rods revealed the following: though rods were mostly formed of small particles, the large particles contributed to these rods by locating mostly at the

ends of the rods. In addition, rods appeared to have grown independent from one another, meaning that there was no observable side attachment between the rods.

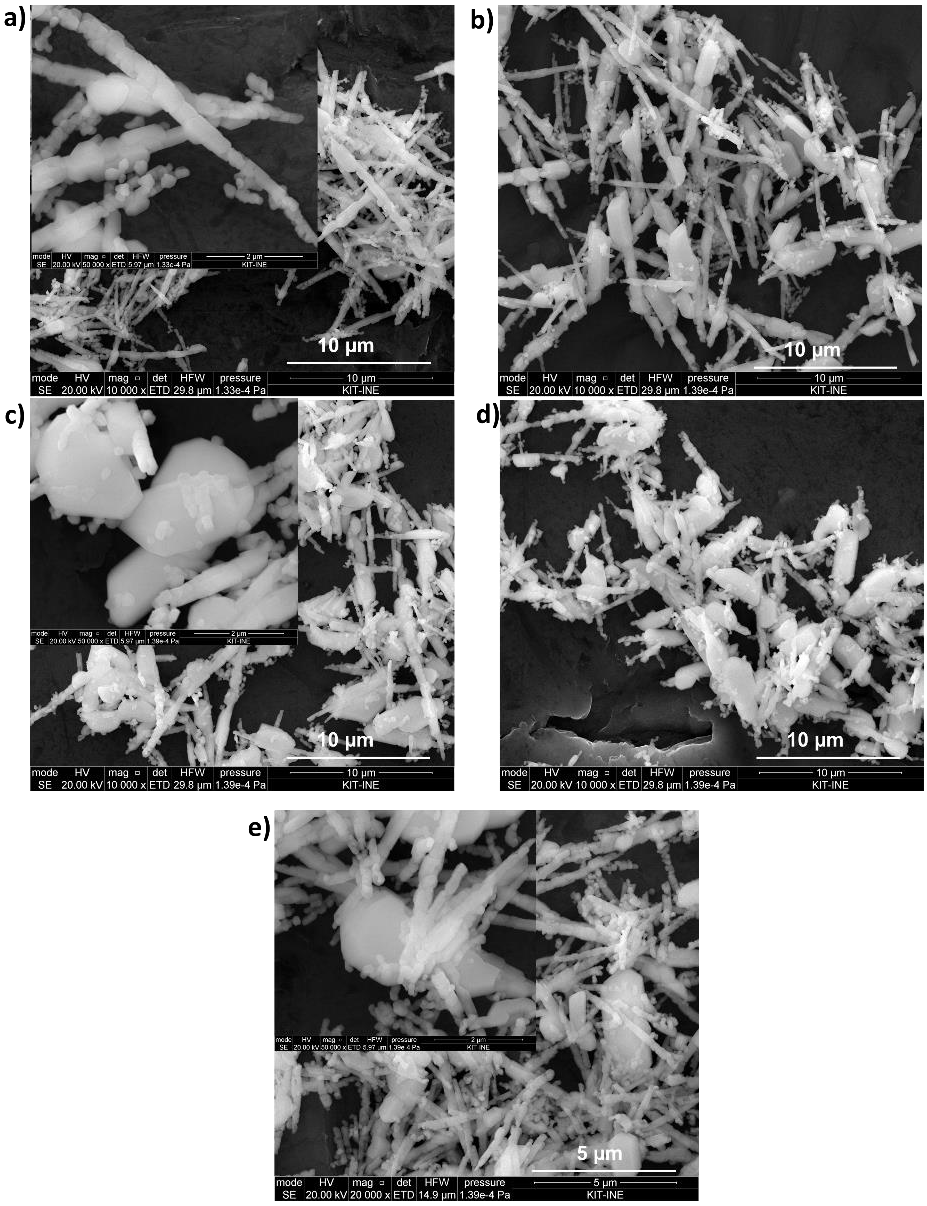

Figure 48. SEM images for witherite precipitated in the absence and presence of radium, which both show witherite particles with the typical hexagonal feature, but large and small particles. In addition, the back-to-back attachment the particles with each is observed.

Further particles are nano-sized and show prismatic features and the distinct shape of witherite and other aragonite type minerals. The difference in size for witherite particles in both experiments $(Ba, Ra)CO_3$ and pure witherite could be due to different reaction stages with small needles forming initially at high supersaturation while the more blocky hexagonal particles form at later stages and lower supersaturation.

The analysis of solutions after the (co-)precipitation experiments show that incorporation occurred for all radium concentrations as shown in Figure 49.

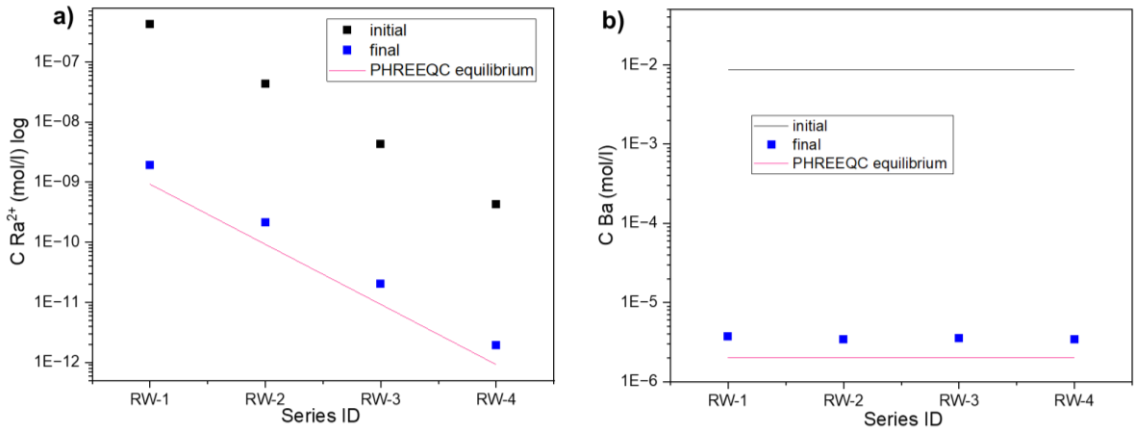

Figure 49. (a) shows Radium concentrations for series of batches of witherite precipitation in the presence of radium. Initial spiked radium is compared with concentrations at the end and the concentrations excepted at equilibrium (obtained via PHREEQC calculations). (b) shows Ba concentration for witherite batches that were precipitated in the presence of radium compared against the initial Ba concentrations and concentrations obtained via PHREEQC.

Measured radium concentrations are higher than calculated ones. Ba^{2+} concentrations obtained experimentally are higher than suggested by PHREEQC calculations for equilibrium conditions (Figure 49.b).

The solid-liquid partition coefficient for $^{226}Ra\ at$ different ^{226}Ra concentrations was (0.15 ± 0.05). This is an indication on the limitation of ^{226}Ra incorporation into witherite structure.

8 Discussion

8.1 The transformation of barite cubes into witherite

Witherite phase growth onto barite surfaces via CDP processes

The contact of AR and IB barite cubes with carbonate solutions led to the initiation of CDP processes that resulted in formation of witherite phase as layers riming the barite cubes as can be seen in Figure 20, Figure 21 and Figure 23. Witherite formation observed in the present study confirms previous studies that found witherite formation replacing barite square plates under hydrothermal conditions, conducted by Rendón-Angeles, J.C., et al., 2008 and Suarez-Orduña et al., 2009. For the replacement processes to be initiated, the system ought to obey CDP reaction mechanisms, where barite dissolution has to occur first, then followed by witherite precipitation as detailed before (see 2.1). The chemical reactions for CDP of the current system can be written as follows:

$$BaSO_4(s) + CO_3^{-2}(aq) \rightarrow Ba^{+2}(aq) + SO_4^{-2}(aq) + CO_3^{-2}(aq)$$

Equation 28

$$Ba^{+2}(aq) + CO_3^{-2}(aq) \rightarrow BaCO_3(s)$$

Equation 29

However, for witherite to start forming, a supersaturated solution with respect to witherite has to form. Thermodynamic calculations show that high supersaturation levels can occur under the present experimental conditions (Figure 50).

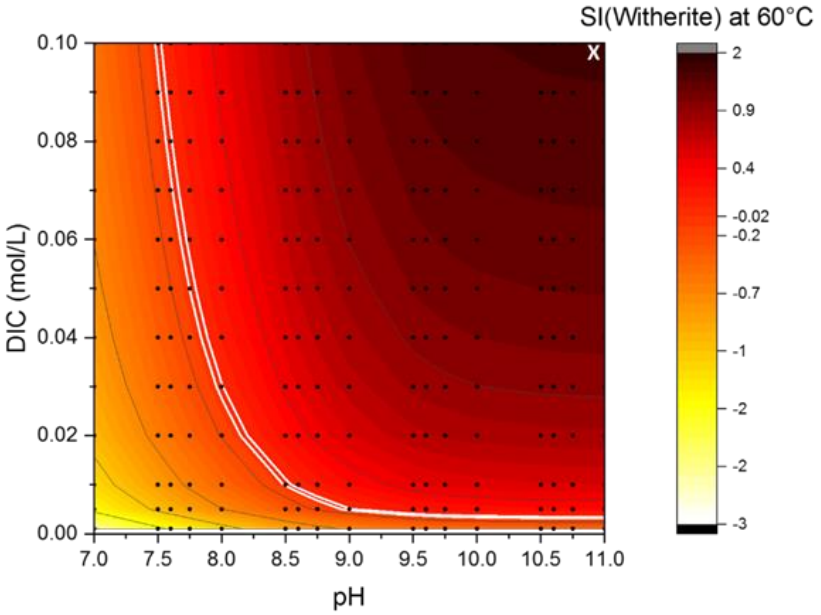

Figure 50. shows the calculations for the superstaturation levels of the solution with respect to witherite. Note the high superstaturation level for Na_2CO_3 concentrations of 0.1M, pH value of 11 at 60 °C (white X marks the present conditions in the figure), which was the condition in the experiments with barite cubes. The white lines show the equilibrium states for the systems with different carbonate and pH values. The calculations were carried out using PHREEQC (Parkhurst and Appelo, 1999) and the PHRREQC.DAT database (Parkhurst and Appelo, 2000).

Furthermore, the amount of barite needed to be dissolved to cause supersaturations for solution with respect to witherite is not necessarily to be significant, but monolayers of barite would be sufficient for the interfacial layer (displayed in Figure 3) to be supersaturated, leading to CDP reactions in the replacement front (displayed in Figure 3) as known from previous studies (Putnis, 2015; Rendon-Angeles, et al., 2000) in 2.4. Therefore, it is highly likely that the cubes of this study had highly supersaturated interfacial layers that led to development of replacement fronts at the IB and AR barite surfaces, resulting in witherite layer formations.

Witherite formation mechanism on barite

The small gap between barite and witherite phases (Figure 23.c) clearly indicates the occurrence of CDP processes with high supersaturation states with respect to witherite in the interfacial layers.

The witherite layer thickness increases as time evolves (Figure 24 and Figure 25) for both IB and AR barite. The witherite layers initially grow at barite surface as can be seen clearly in IB and AR cubes that reacted for 24 hr . These initial particles are then followed by other particles that keep building up, leading to thickening the witherite layers as can be observed on cubes with longer reaction times. Simultaneously barite peaks in Raman spectra decrease over the reaction time as shown in Figure 20.a and Figure 20.b for AR and IB barites. This is due to the masking of barite surfaces by witherite layers that inhibits scattered Raman laser signals coming from barite surfaces (see chapter 4 for details on Raman spectroscopy). As layers continue to grow, the masking effect becomes more profounder, leading to further weakening of the Raman signals.

The formation rates of witherite layers

Reaction rates for witherite layer formation are rapid in the early reaction stages as Figure 25 shows. Later, the reactions slow down at around 240 hr, where the transformation to witherite is slower in the case of the AR barite as compared to the rate for the IB barite.

Decreasing reaction rates could be attributed to the effect of witherite layer thickness on supersaturation levels with respect to witherite. In early stages at which the witherite layer is not thick, it is easy for fresh carbonate solution to diffuse through the layers, to reach the barite surfaces and react with them. As time goes by and layers thicken, the diffusion of carbonate through the layers is hindered and the replacement front supply with carbonate is limited, hence the reactions slow down after 240 hr for AR and IB barite types. The limited supply of carbonate to the replacement front implies that supersaturation levels are decreasing leading slow down of reactions. The influence of the witherite layer thickness on the supersaturation levels can be shown in the results of PHREEQC diffusion model with PHRREQC.DAT (Parkhurst and Appelo, 1999) as displayed in Figure 51. As the distance from the model barite cell to bulk solution increases, simulating the increase of the witherite layer, the saturation indices decrease and witherite formation rates decrease.

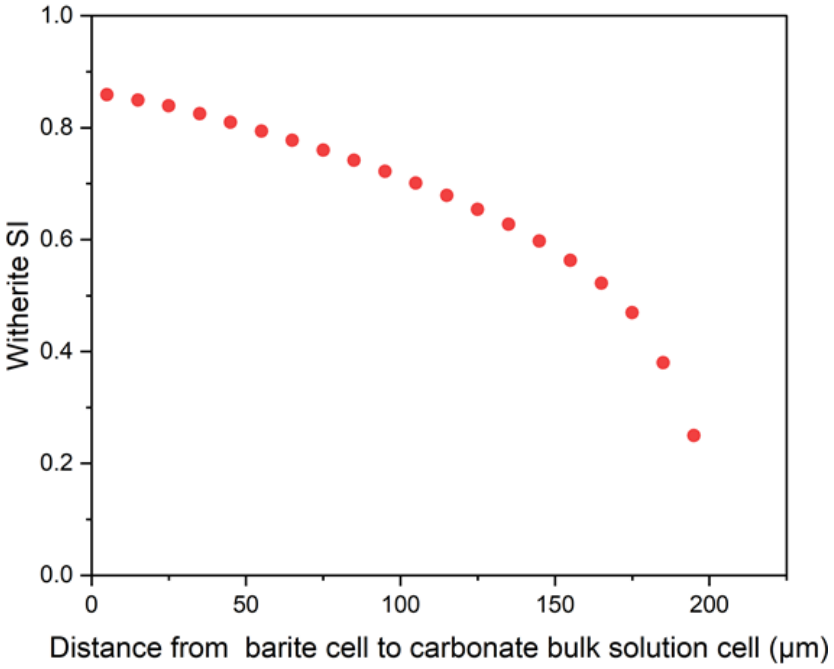

Figure 51. PHREEQC diffusion model calculation results that show the effect of witherite layer thickness increase on the supersaturation levels with respect to witherite.

The higher witherite formation rate of IB barite compared to that seen for AR barite is most likely due to the characteristic rough and amorphous nature of type IB crystals (Figure 13.a). This implies higher surface areas of IB as compared to AR barite that shows much more smoother surfaces and clear crystallinity. The rough property for IB type is due to milling the crystals into particles with micron size (Figure 18.d) while AR barite milled particles show smooth surfaces indicating the formation of cleaved surfaces when milled (Figure 18.e). The dissolution rate is rather critical for the formation of witherite and is positively correlated with the surface area, which can be described by the Noyes-Whitney equation as follows (Li, Shoujiang, et al., 2009):

$$\frac{dm}{dt} = VM\,\frac{dc}{dt} = \frac{MDS_a}{h}(C_s - C)$$

Equation 30

where dm/dt is the dissolution rate, S_a is the surface area of the crystal, D is the diffusion coefficient, C and C_s are the concentrations of the solute in the solution at a certain time (t) and solubility, respectively, and M and h are the relative molecular mass and diffusion layer thickness of the solute, respectively. When the surface area increases, the dissolution rate increases as well as Equation 30 dictates. Therefore, the roughness of IB barite allows for more interactions between the carbonate solution and IB surface, leading to more chemical bond breaking and release of Ba into the reaction front. Consequently, the supersaturation levels with

respect to witherite are higher in the experiments with IB type barite than with AB barite, leading to the higher witherite formation rate for IB barite.

Another important property is the crystalline size of the two barite types shown in Figure 16. The type IB barite has a smaller crystalline size than AR barite, which could be due to the presence of Sr in barite as $(Ba,Sr)SO_4$ solid solution as Sr was found to contribute to the diminishment of crystalline size of barite (Brower and Renault, 1971) (see section 7.2.1). The crystallite size can influence the dissolution rate of a crystal, which was found by N.J. Welham and Llewellyn (1998) who studied the leaching of ilmenite and found a correlation between higher dissolution rate and smaller crystallite size. The effect of crystallite size on surface can explained as follows: as the size of crystallites decreases, a larger percentage of atoms are present at the mineral surface and this results in an increase in both specific surface area and surface free energy (Wang, et al., 2013), that leads to high Ba concentrations in the interfacial layer and eventually contributes to higher witherite formation rates for IB barite.

The generation of porosity within witherite layers

The traveling of the carbonate solution through the witherite layers to the reaction front requires pathways to be formed within the layer, regardless of the layer thickness. These pores can be seen clearly within the witherite layers in SEM images of Figure 23. Furthermore, a close inspection at Figure 23.c shows that pores are interconnected and forming networks from the outer part of witherite layers to surfaces of barite cubes. These networks were functioning as pathways for the carbonate solutions during the replacement reactions from the bulk solution to the replacement front at barite surfaces. Without these pores in the product phase, carbonate solutions cannot travel through the witherite layers and CDP reactions cease. For details on porosity generation mechanisms during CDP, the reader is referred to sections 2.2.1 and 2.2.2.

Barite shape preservation during witherite formation

The growth of witherite layers at barite cubes resulted in preservation of the cube shapes as witherite layers appear to form squares (Figure *21*.a, Figure *21*.b, Figure *23*.a and Figure *23*.b). This is line with results of Rendón-Angeles et al., 2008 who show a preservation of barite shape while witherite forms as well as with studies for sulfate-carbonate systems such Suárez-Orduña et al., 2004 and Pina, 2019 who both conducted studies on the recrystallization of celestine into strontianite.

A closer inspection of Figure 23.c reveals that the preservation of barite morphology during witherite formation is not limited to the cube shape, but also to topographical details of barite surfaces. Witherite apparently mimics the terraces, vacancies and other barite surface features.

This decent perseveration for details of barite surface is due to the fact that the crystal form of both phases is orthorhombic (see chapter 1), which allows for a structural matching between the barite and witherite. Since the two phases have different crystal habits, this imposes limitations to have a perfect structural matching between barite and witherite, which otherwise can lead to armoring barite by witherite layer in early reaction stages and ceasing CDP processes (see 2.3 for details and examples).

The inspection of Figure 23.c also reveals that the gap between the barite and witherite is rather insignificant. This feature reflects the structural similarity between barite and witherite elaborated above, and most importantly it reflects that barite dissolution being the rate limiting step during the CDP processes. For a process to be the rate limiting, it should be slower than the other processes. Slower dissolution processes were observed and elaborated in previous CDP studies such as by Fernandez-Díaz et al., 2009. Altree-Williams et al., 2015, González-Illanes et al., 2017., Pina, 2019. If the barite dissolution would be faster than witherite precipitation, the witherite precipitation would have been the rate limiting step, leading to witherite formation spatially independent from cubes.

The fact that both barite and witherite are orthorhombic and cube surfaces details are well preserved indicates that the CDP process observed in the present study is to some degree epitaxial. This led to the preservation of the barite crystallographic orientation and eventually to the preservation of the overall cube shape, indicating that the barite cubes replacement by witherite is pseudomorphic (see section 2.2.3 and subchapter 2.3 for details and examples on preservation, epitaxy and pseudomorphsim).

The elemental compositions in barite and witherite phases

The elemental analysis via SEM-EDX shows different effects that provide insight into the dynamics of ions dissolution and precipitation during CDP processes. One important effect is changes of elemental concentrations between the two phases as can be seen in Figure 26. These changes show important aspects confirming that the two different textures seen in Figure 21 and Figure 23 are two different phases as S and C drops and increases significantly as can be seen in Figure 27.a and Figure 27.b for type IB and AR.

Interestingly only insignificant gaps between barite and witherite are seen at the boundary between the two phases, which further assures the preservation of cube surface details and shape as well as the epitaxy and pseudomorphism by witherite formation (Rendón-Angeles et al., 2008). The sharp boundary could indicate minimal diffusion or mixing between the phases, suggesting that the replacement occurred under conditions that prevented significant ion

exchange beyond the immediate replacement front. This phenomenon underscores the efficiency of the replacement processes, resulting in the preservation of the cubic morphology of barite in the newly formed witherite layer.

The abrupt change in S and C content could indicate the rapidness of replacement process at the boundary. This reflects the different reaction rates for the dissolution of barite and precipitation of witherite, by which precipitation rate was rapid compared to the dissolution rate. Such precipitation rapidness was facilitated by supersaturated conditions in the interfacial layer, where carbonate ions were readily available to react with Ba ions released from barite dissolution.

The sharp elemental changes observed at the boundary between barite and witherite have significant industrial implications. A sharp boundary indicates different textures and phase purity, which are crucial for understanding and optimizing mineral replacements in industrial settings. In the context of the petroleum and gas industry, these findings suggest a potential method for managing barite scaling in pipes (see introduction for details). The efficient and rapid replacement from barite to witherite, as evidenced by the sharp elemental changes, indicates that witherite can be formed with minimal intermediate phases or mixed zones. This replacement process could be of great benefit to mitigate barite scaling. By promoting the replacement of barite with witherite, it may be possible to develop strategies for scale management that improve the longevity and efficiency of pipeline systems. Additionally, understanding the conditions that favor such witherite phase purity replacement can aid in the design of more effective scale inhibitors and treatment protocols, ultimately benefiting the petroleum and gas industry by reducing maintenance costs and improving operational efficiency.

The scanline measurements in Figure 27.a and Figure 27.b show the presence of sulfur in witherite layers. Similar findings are also documented by Suárez-Orduña et al., 2004 and Pina, 2019 who both conducted studies on the conversion of celestine into strontinite. This led Pina, 2019 to suggest $Sr(CO_3,SO_4)$ solid solution as a possible explanation for the presence of sulfur. Correspondingly, DFT-SDM calculations were performed in the present study for insightful understanding of the thermodynamics of CO_3-SO_4 solid solutions, in particular the mixing properties of $Sr(CO_3,SO_4)$ solid solution systems. The calculations showed that degree of non-ideality, indicated by the Guggenheim parameter, was rather high (see 7.1). The high degree of non-ideality implies that there is a high contribution from the enthalpy (ΔH_E) and this is due the significant molar volume difference between CO_3 and SO_4, which is $\Delta V_m = 7.55\ cm^3 / mol$

(Table 1). The fact that ΔV_m is much greater than zero indicates that the phase separation is favored and that the formation of Sr(CO_3,SO_4) solid solution is highly unlikely. The presence of sulfur in the witherite phase could be associated with kinetics rather than with thermodynamics since CDP reactions can be fast and not allowing for a complete equilibration to occur, which may lead to the entrapment of S within the crystal lattice of witherite or in witherite layer microstructures.

The analysis via SEM-EDX mapping in Figure 26.a for IB type shows a Sr presence in both barite and witherite solid phases. Such presence depicts Sr as an equally distributed element between the two phases. Furthermore, the SEM-EDX scanline for IB type barite in Figure 27 shows that the Sr elemental concentration is rather similar in both phases and no effect at the boundary between the two phases is seen for the Sr distribution. The Sr/Ba ratio is rather constant (0.12±0.02) throughout the two phases. The presence of Sr in IB was suggested in 7.2.1 to be most likely in the form $(Ba, Sr)SO_4$ solid solution, therefore, the consistency of the Sr/Ba ratio in both solid phases suggests the formation of a solid solution between barium carbonate $BaCO_3$ and strontium carbonate $SrCO_3$, $(Ba, Sr)CO_3$, within the witherite crystal structure.

The consistent Sr/Ba ratio in barite and witherite shows that the processes involved in the barite dissolution and witherite formation are most likely congruent. In addition, the consistent Sr/Ba ratio shows how witherite can efficiently maintain Sr after being released from barite by incorporating it into its structure. Studies in the past such as by Baldasari and Speer 1979 and Prieto et at., 1997 pointed out such Sr/Ba ratio maintenance by witherite, which can have different implications in geological and industrial settings. The Sr uptake by witherite and Sr/Ba ratio preservation between the two phases will be explored further when discussing the same effects, but for IB barite particles that transformed into witherite (see 8.2).

The evolution of ion concentrations in the carbonate reaction solution

The evolution of Ba and Sr ions in the carbonate solutions during different reaction interval times show that Ba and Sr are considerably present in the bulk solution (Figure 28.a). Though it is true that the supersaturated replacement front accommodates during CDP reactions, most of the Ba and Sr ions released from barite are reacting immediately with carbonate in replacement front, whereas the bulk solution is to a good extent isolated from reaction. This is indicated by the one order of magnitude difference between Ba concentrations in solutions and the higher Ba equilibrium concentration of barite (Figure 28.a) though witherite replaced considerable part of barite cubes (Figure 24). However, the escape of ions from the reaction front to the bulk

solution cannot be completely excluded. The analysis of the solution show that Ba and Sr concentrations increase with time. This aspect is shown by previous studies such as Hövelmann et al., 2012; Putnis, C.V., et al., 2005 as they observed that ions involved in the replacement reaction could make their way out of the front to the bulk solution via diffusion. Though the amount of the escaping ions during CDP processes is most likely minimal compared to what is being consumed in the replacement front, it can possibly have a considerable effect on bulk solution in terms causing the solution to have imbalanced ionic compositions. One potential reason behind the escape of the ions to the bulk solution is possibly due to the difference of local dissolution rates in the reaction front due to local surface topographies as found by Hövelmann et al., 2012. This means that Ba and Sr are overpopulated in the interfacial layer in particular areas and not all being consumed in the replacement reactions, leading some to find their way out to the bulk solution.

The evolution of Ba concentration in solution in presence of IB and AR barite show similar and different behaviors as can be seen in Figure 28.a. Both types Ba evolution trends are the same in early reaction stages as they increase linearly. Later, Ba concentrations for both type level off become constant after about 600 hrs reaction time. This could be due to the increase of the witherite layer that affects the already limited escape of Ba ions from the replacement front to the bulk solution.

The evolution of Sr in the IB carbonate solution is overall constant over the different reaction times as can be seen in Figure 28.a. However, the solution Sr/Ba ratio is about five times higher than in the solid (0.12±0.02, see Figure 27.a) in the very early reaction period, then it decreases to reach a value closer to that in the solid after 600 hr. This poses a discrepancy between in the solid and solution Sr/Ba ratios as the constant solid ratio suggests a congruent CDP process.

This discrepancy between the solution and solid phases might seem counterintuitive at first, given the established strong affinity of Sr for incorporation into the witherite phase. Under typical conditions, we would expect the Sr/Ba ratio in the solution to decrease as Sr preferentially incorporates into the forming witherite phase, especially considering that D_{theo} coefficient for Sr is significantly higher for witherite (0.17) than for barite (0.0002); D_{theo} for witherite and barite are obtained using Equation 23 with the nonideality parameter from Vinograd et al., 2013 for Sr into witherite (1.47) and from Heberling et al., 2017 for Sr incorporation into barite (1.6) along with solubility products ($Ksp, witherite = 10^{-8.66}$ at 60°C and $Ksp, strontianite = 10^{-8.49}$ at 65°C; $Ksp, barite = 10^{-9.65}$ and $Ksp, celestite = 10^{-6.75}$ at 60°C , obtained from Brown et al., 2019).

However, a mole balance reveals that the total moles of Sr and Ba in the solution are extremely small (~$2 \cdot 10^{-7}$ moles, obtained from Ba concentrations in Figure 28.a) compared to the moles present in the solid phases (~$5 \cdot 10^{-5}$ moles, obtained from weight of a cube ≅ 120 mg). This significant difference suggests that even substantial changes in the Sr/Ba ratio in the solution would not noticeably impact the Sr/Ba ratio in the solid phase, which may explain the observed consistency in the solid ratios despite fluctuations in the solution.

Given this context, the observed high Sr/Ba ratio in the solution at early reaction stages likely reflects a kinetic effect rather than an equilibrium state. As Sr begins to incorporate into the witherite, the solution Sr/Ba ratio decreases, gradually approaching the ratio observed in the solid phase. The initial high ratio could result from a temporary imbalance between the dissolution of Sr-barite and the precipitation of Sr-witherite, where the dissolution of barite releases Sr into the solution faster than it can be incorporated into witherite.

Further complicating the situation, the local environment at the interface between barite and witherite may introduce additional factors. Variations in local porosity within the witherite layer, for example, could affect the mass transfer rates of carbonate ions and, consequently, the dissolution rates of barite. This could lead to spatially heterogeneous dissolution rates, affecting the local ionic concentrations of Sr and Ba and ultimately contributing to the observed discrepancies between the solid and solution Sr/Ba ratios.

8.2 The transformation of barite powder into witherite

The five barite types P, SL, LT-SL, AR and IB underwent chemical reactions upon contacting with carbonate solution (0.01, 0.05 0.1 M, pH 9.5, 10, 11 and 11.30) similar to reactions in Equation 28 and Equation 29. As a result, barite transformation into witherite occurred, which were confirmed via XRD measurements, SEM images and SEM-EDX elemental analysis displayed in Figure 29, Figure 30 and Figure 32.

Although the chemical reactions for transformation processes are similar to the ones of CDP reactions, the mechanism of the witherite formation is different as witherite particles are clearly not forming at barite particle surfaces and not mimicking their morphological details nor preserving the overall particles shapes. This indicates the absence of the coupling effect between witherite and barite phases as its evident in Figure 30. Though it is true that the processes show the absence of coupling effects and preservation of barite particle features in witherite, witherite shows association to barite particle surfaces more in experiments with type SL and LT-SL barites than in others. Witherite formation rate is highest in experiments with SL and lowest in case of LT-SL (Figure 29.b).

The type IB barite powder exhibited a similar behavior as IB cubes in terms of forming more witherite than AR (Figure 29.c, Figure 29.d and Figure 34), reaffirming the role of IB characteristics positively influencing witherite formation. In addition, IB shows release of Sr during dissolution and its incorporation into witherite particles upon their formation (Figure 35), which similar to the cubes in terms of solid Sr/Ba ratio, but differs in terms of solution Sr/Ba ratio as it similar to solid ratio. The type P barite showed the second highest witherite formation rate (Figure 29.a) for carbonate concentration (0.05) and pH 9.50, indicating the role of its nano size particles in boosting the transformation process.

Moreover, the effect of variations of carbonate concentrations that contribute to barite dissolution and witherite precipitation by influencing the chemical equilibria and the different pH values that influence the presence of reactive carbonate species involved in the transformation reactions were observed.

SL barite dissolution processes

The witherite formation of SL barite type was highest among all types of barite (Figure 34 Figure A.2). These is due to the unique characteristics of the SL barite: small intergrown particulates attached to it surfaces, external surface porosity and internal structural porosity (see Figure 15.b). In addition, SL has the second smallest and the reader is referred to subchapter 5.1 for more details on such characteristics.

To assess the effect the above-mentioned characteristics of SL type dissolution processes, particles were reacted with solely 0.1M NaCl for different time intervals over five weeks. The results revealed the rapid dissolution of firstly the small particulates attached to large particles which started disappearing after one day reaction time, and almost completely dissolved after five weeks leaving behind pits (Figure 52.a and Figure 52.b).

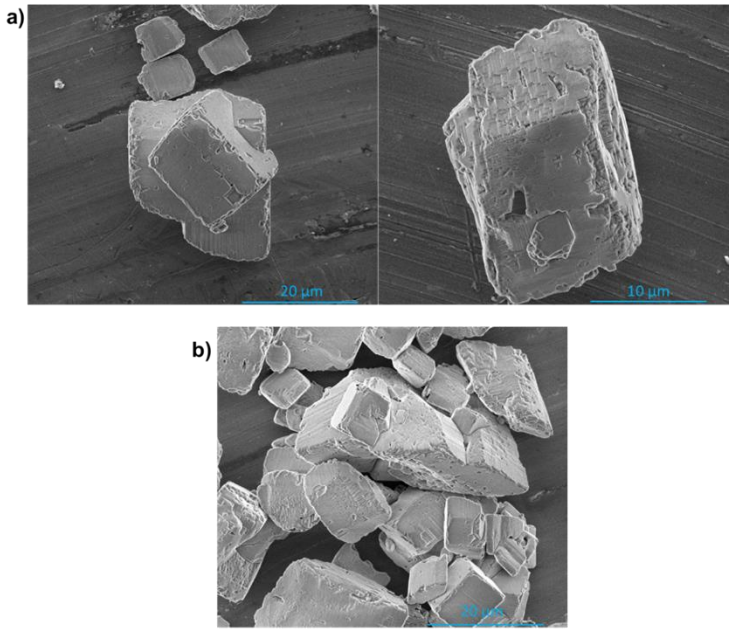

Figure 52. shows (a) SEM-SE images showing SL particles after one day reaction time with 0.1M NaCl by which the small intergrown particulates mostly vanished and (b) SEM-SE images for SL barite particles after 5 weeks reaction period with 0.1M NaCl where rather stepped irregular surfaces have developed.

The initial dissolution of the SL small particulates was also observed by Weber et al., 2017 and Heberling et at., 2018 after reacting with 0.1M NaCl for 0.35 years and 0.8 years, respectively. This dissolution is due to known effect that smaller particulates have higher surface specific area that in turn leads to higher exposure to the solution, which corelates with dissolution positively as Equation 30 dictates.

In addition to the dissolution of the small particulates, irregularities in the form of steps in the SL large particle surfaces were observed here as well as by Heberling et at., 2018. They attributed it to the development of pits created after the dissolution of the small particulates. The pits cannot be recognized clearly in SEM images of Heberling et al., 2018 since irregularities completely invaded the surfaces of the large particles possibly due to the long pre-equilibration time (0.8 year). However, the SL particles in the present study were reacted for much shorter time and pits still can be observed in Figure 52, which can further support the suggestion of Heberling et al., 2018. In addition, the relevance of the appearance of such irregularities seems to differ for different barite types. Those differences can be due to different barite surfaces planes resulting in different reactivities.

The irregularities in SL particles observed in the present study appear as steps that spread over most of SL surfaces. These steps might possibly act as reaction fronts, meaning were functioning as means for solution reactants to induce local dissolution. Therefore, these steps like-reaction fronts were advanceing as reactions processed similar to cube replacement fronts.

The steps and their advancement due to dissolution can be supported by the fact that SEM images of Heberling et al., 2018 do not clearly exhibit the pits of dissolved particulates and that is due to the movement of steps as a result of dissolution during the pre-equilibration period (0.8 year), leading to a wide spread surface dissolution and a decrease in pits depth.

The small SL particle size enhances dissolution according to Equation 30. In addition, the average L/W of the SL barite its relatively small (1.45 ± 0.41).

The moderate L/W ratio allows for moderate distribution of reactive sites at the particle surfaces such as small particulates and pores, and that offers the solution good accessibility to such sites, contributing to SL dissolution.

The external and internal porosities can play a critical role during the dissolution processes of the SL type. These layers of nano-pores were studied in depth by Weber et al., 2016 and showed unstable behavior upon reacting with Ra carrying solutions of different concentrations over different reaction intervals up to 3.84 years. The nano-pore layers were merging into macropores as indicated by Weber et al., 2016 due to surface energy minimization during Ra uptake reaction until all layers disappeared and only macropores created by merging layer remined besides the originally existing macropores.

The aforementioned internal evolution within the SL barite led possibly to the growth of an outer coherent rim with a high density of the $(Ba,Ra)SO_4$ solid solution, which possesses internal nano-layer pores which was already reported by Weber, J., et al., 2016. This stability effect was also observed by Heberling et al., 2018 who found a decrease in Debye-Waller parameters obtained from XRD measurements, which they attributed to a more well-ordered crystal structure after pre-equilibration period (0.8 years). In addition, Heberling et al., 2018 observed a continuity of crystallinity increase whereas specific surface area remained unchanged and no significant changes in SL particle surfaces appeared after the pre-equilibration period during 4 years of reaction with Ra carrying solution. This led then to a conclusion, similar to what Weber et al., 2016 had arrived to, that internal restructuring within SL barite was occurring. These observations regarding SL type internal reactivity are of importance for the present study as they shed light on process dynamics during reactions for this type that can affect the entire particle bulk.

The connectivity of surface and internal porosities is of significance as it can create fast pathways for the solution to diffuse inside the internal structure of the particle. The presence of the such connectivity can be observed in Figure 33.f where internal porosity layers are seen spreading across the SL particle bulk and reaching the outer surfaces of the particles. The

investigations of SL internal structures by Weber et al., 2016, who provided 3D-reconstructing multiple FIB-SEM cuts, showed clearly that the external and internal pores are connected.
This interconnected porosity can play a positive role during the dissolution process when SL particles are in contact with carbonate solution. The connected pores allow for more efficient penetration and distribution of the solution throughout the particle. This enhanced diffusion can lead to a more uniform and rapid dissolution, as the solution can access and react with a larger surface area within the internal structure. Additionally, the increased surface area exposed to the solution can accelerate the overall reaction rate, facilitating faster and dissolution processes.
The aforementioned aspects underscore the unique characteristics of SL type barite, which significantly enhance its dissolution process. The presence of small intergrown particulates, extensive external and internal porosity, and the connectivity between these porosities facilitate rapid and efficient penetration of the carbonate solution. These characteristics not only increase the surface area available for reaction but also ensure uniform dissolution throughout the particle.

SL witherite formation processes

The unique external and internal characteristics features for SL barite type not only lead to the exhibition of distinguished dissolution processes, but also to a diversity in witherite formation mechanisms upon the contact with carbonate solution that are shown in Figure 30.b, Figure 30.c and Figure 32.f that can be summarized as follows:

1. The formation of permeable and highly rough layers on barite particles.
2. The association of witherite particles growth with rough layer.
3. The possible witherite growth inside the barite bulk.

The inspection of Figure 30.b and Figure 30.c shows a rough layer growing at barite particles being associated with growth of witherite, and no witherite formation was found without the exitance of the rough layer (Figure 18). The inspection of structural apparency of the rough layer reveals that it is different to the dense Ra-barite outer rim mentioned earlier by Weber et al., 2016, as the rough layer contains large pores. In addition, the rough layer is not showing the stepped irregular features that Heberling et al., 2018 found in SL particles after long barite pre-equilibration period with 0.1M NaCl. Theses observation could indicate that the rough layer is not a barite composed layer.
The analysis of the layer via SEM-EDX via elemental mapping (Figure 32.b) shows carbon content presence with some spots appearing to have high contents compared to others. This

could support the hypothesis that such layer consists of witherite, but such hypothesis needs further confirmation. FIB-SEM cuts with careful elemental analysis should obtain elemental maps with high precision that can reveal the exact nature of the layer.

The rough layer appears to grow rather close to the SL barite particles as indicated in the FIB-SEM cut displayed in Figure 33.f. This suggests that the rough layer growth mechanism is governed by coupled processes, similar to the way witherite layers grow on barite cubes. The growth mechanism of the rough layer could be suggested as the following: (1) the dissolution of SL particles, which led to (2) the creation of pits that caused surface irregularities in the form of steps spreading over the surface and (3) the retreat of the barite steps and the formation of advancing witherite layers. The inspection of the rough layers (Figure 30.c, Figure 33.a and Figure 33.e) shows that it contains voids in its surface. The voids could function as pathways to solutions to diffuse in and out, and this signifies a rather crucial aspect since it means that such layer is not a completely isolating the barite bulk from solution. The permeability of the layer can help in unveiling the processes related to the formation of witherite particles.

The witherite particles grow close to the rough layer at the SL barite surface, as shown in the SL SEM, SEM-EDX, and FIB-SEM images. This rough layer likely acts as an armoring structure around the underlying barite particle, hindering the diffusion of Ba ions through its large pores. As a result, the Ba ion diffusion is slowed, therefore, reaction with carbonate leads to the fast formation of witherite particles on the rough layer, which serves as a substrate for these particles.

The diffusion through the rough layer is not limited to Ba ions; carbonate ions can also diffuse in and travel through to the barite bulk. This implies that carbonate could react with Ba within the witherite bulk to form witherite particles. Figure 33.f shows what appears to be a small witherite particle that grew into one of the internal pores. This suggests that witherite growth could continue as long as carbonate diffuses through the layer, feeding the witherite formation reaction.

On the other hand, the dissolution of the barite bulk needs to continue to provide Ba for the witherite formation reaction. As a result, witherite formation beneath the rough layer could consume a significant portion of the barite bulk if the reaction persists long enough. This could explain the gap found beneath the rough layer during the removal of the segment of the particle shown in Figure 33.a. This gap was discovered during the cutting procedure, revealing a cluster of witherite particles as shown in Figure 33.b.

In other words, witherite particles likely started forming in a pore or pores within the barite bulk. Over the reaction course, barite was consumed, and witherite formed until no more barite

was available for the reaction to proceed. The cluster of witherite particles beneath the rough layer could have grown by filling all the gaps, spatially replacing the barite bulk.

However, the barite bulk also contributes to the formation of witherite particles on the rough layer exterior, meaning both internal and external witherite growth processes are fed by the same barite bulk. Consequently, the space beneath the rough layer was found to be partially hollow, with the rest occupied by witherite.

The cutting investigations demonstrate the stability of the rough layer, even though ions were diffusing in and out through it and reactions were occurring beneath it. Its structure remained intact, which could indicate that the layer is a witherite phase formed in the early reaction stages, thus not contributing to the later stages and remaining observable by microscopic techniques.

This close association of rough layer and witherite particles with the barite particles can be explained by considering the formation of supersaturated interfacial zones near the barite particles where the dissolution and precipitation processes occur. The rough layer might form first, limiting the diffusion of dissolved Ba ions to the immediate vicinity of the barite particles and creating local supersaturation zones with respect to witherite that lead to formation of witherite particles. These zones then engage predominantly in the processes, with minimal equilibration with the bulk solution.

This concept is supported by King et al. 2010, who observed a similar phenomenon when olivine reacted with carbonate solution. They reported that the formation of an amorphous layer and particles closely associated with the olivine surface was due to local interfacial supersaturated zones controlling the dissolution and precipitation processes. In their study, bulk solution measurements could not reliably indicate the supersaturation state of the solution with respect to the new phase.

Additionally, examining the Ba evolution in the SL solution over different time intervals, as shown in Figure 35.a, helps clarifying this explanation. The Ba concentration declines exponentially more sharply than in presence of the the other barite types, which could indicate that while the bulk solution is not entirely isolated from the dissolution and precipitation processes, the rough layer limits its involvement. Local supersaturation zones near the barite particles are the primary areas of activity, leading to witherite formation.

The characteristics of type P, IB and AR barite dissolution and witherite formation

The type P barite was experimented with only the condition carbonate concentration (0.05M) and pH 9.50 (Figure 34.c) and showed the second highest witherite formation after the

SL type. This is due to the synthesis by fresh precipitation, which resulted in in the smallest particle size as well as the smallest crystallite size (see Figure 15.a and Figure 16). The small particle size and the small crystalline size correlate positively with dissolution as discussed earlier (see *SL barite dissolution processes* in subchapter 8.2 and *the formation rates of witherite layers* in subchapter 8.1), leading to high Ba^{2+} presence in bulk solution and, consequently, high supersaturation level with respect to witherite.

For all the experimental conditions except carbonate concentration (0.05M) and pH 9.50, the type IB barite resulted in witherite growth that is the second highest after type SL (Figure 34 and Figure A.2). This is most likely related IB barite characteristics shown in subchapter 7.2 that affect positivity this type dissolution, which are discussed in subchapter 8.1.

The dissolution features for IB barite are clearly observed on particle surfaces after reaction with carbonate for 31 days (Figure 30.f). The surfaces exhibit etch-pitting effects where pits form through a process that most likely started with nucleation, followed by growth and intersection, eventually leading to the etching away of the surfaces (Brantley, 2008). The IB barite surfaces also show other dissolution features known as sawtoothed and mammillary structures (Figure 30.f).

The mammillary structures are suggested to result from dissolution and are associated with specific surfaces, indicating crystallographic dependence and anisotropic dissolution processes (Grandstaff,1978; King et al., 2010 and references therein). The sawtoothed structures are thought to be generated from the parallel merging of lenticular etch pits (King et al., 2010). These dissolution features are similar to those found by King et al., 2010 and references therein, who suggested that dissolution is particle- solution interface-limited.

However, the present study shows that IB witherite particles grow in a manner not directly associated with the barite surfaces, as they appear to form unattached to the barite surface (Figure 30.f). As discussed earlier, the association of the resulting phase to the surface of the original phase requires the processes to occur in interfacial supersaturated zones near the original phase.

Ba concentrations are high in the early reaction stages associated with rapid witherite formation (Figure 34a). In later stages, Ba concentration decreases, reaching a steady state due to a balance between barite dissolution, which witherite formation shows as well.

Therefore, it can be said that processes of IB barite transformation are not limited to interfacial solution zones but involve the bulk solution as well. The study by King et al., 2010 suggests that the bulk solution is not part of the processes, which may be due to the formation of the

amorphous layer on olivine during reaction with carbonate, restricting bulk solution involvement.

These dissolution features indicate the ability of IB barite to supply a considerable amount of Ba ions to the solution, reacting with carbonate and achieving high supersaturation levels. This is the reason that IB shows the second highest witherite formation among all types. The high dissolution rate of IB barite is also reflected by the Ba concentration in the bulk solution, which is much higher than that in experiments with AR, which shows the least witherite-formation.

The high abundance of Ba in the solution and the high supersaturation state with regard to witherite leads to the smallest IB witherite particles forming among all experiments (Figure 31.c), as predicted by classical nucleation theory (Yuan et al. 2021).

Theoretically, this should result in the highest witherite formation for the IB barite and not for the SL barite, where larger particles form on average (Figure 40.b, c). One way to reconcile this is by considering the effect of Sr incorporation into witherite particles, which can inhibit growth.

This growth inhibition, reported by Weber et al. 2018 and Yuan et al. 2021, occurs when Sr is present at step or kink sites, restricting steps advancement. The incorporation of Sr by IB witherite is observed in SEM-EDX analysis of witherite layers, showing Sr presence (Figure 26.a and Figure 27.a). The SL barite on the other hand does not contain Sr.

The shift of XRD peaks to higher angles (Figure 29.d) indicates Sr incorporation into witherite structures. Sr has a smaller ionic radius (1.31 Å, Liang, Y., et al., 2020) compared to Ba (1.47 Å, Yoshida et al., 2014), resulting in reduced lattice spacing (d) in Bragg's Law (Equation 25). According to Bragg's Law, reduced d-spacing leads to higher 2θ values, hence the shift seen in Figure 29.d

The AR barite type exhibits the lowest witherite formation rate, as indicated by the Rietveld refinement analysis shown in Figure 34 and Figure A.2. This low formation rate is likely related to the characteristics of AR barite discussed in subchapter 7.2, which negatively impact its dissolution as elaborated in subchapter 8.1. Upon inspecting Figure 30.e, it becomes evident that the particles of AR barite exhibit low reactivity. The surfaces of these particles appear largely intact, showing limited signs of dissolution. Etch pit formation is minimal and does not propagate widely over the surfaces, especially when compared to the surfaces of IB barite.

The evolution of Ba concentration over the reaction time (Figure 35.a) further indicates the limited dissolution of AR barite. The Ba concentration starts at much lower levels than in case of IB barite and decreases moderately before reaching a steady state that persists until the end

of the reaction period. The witherite particles formed from AR barite are the largest, as shown in Figure 31.d. This is not surprising given the slow dissolution rate of AR barite.

The large size of AR witherite particles is most likely due to the low supersaturation levels with respect to witherite, resulting from the limited dissolution of AR barite. This slower dissolution process allows for longer nucleation and growth periods for the particles. This can be observed in the moderate decrease in Ba concentration, followed by a steady state (Figure 35a). This provides the particles more time to grow before reaching saturation.

The different stages of Ba concentration clearly reflect the growth of witherite in Figure 34. The decrease in Ba concentration indicates ongoing witherite formation, which continues to increase until the Ba concentration reaches a steady state. At this point, equilibrium is achieved, and witherite growth becomes almost constant.

The uncoupled effect for P, IB and AR types during transformation processes

The growth of witherite as a result of the transformation processes for P, IB, and AR barite types due the absence of coupling effect between the barite and the resultant witherite. This uncoupled effect is linked to the precipitation of witherite being the rate-limiting step in the transformation reaction. Unlike coupled dissolution-precipitation (CDP) processes, uncoupled processes are less common in natural rock textures and experimental reactions, as noted by Putnis, 2015. Consequently, they receive less attention in the literature compared to CDP processes.

To clarify the uncoupled effect, Putnis, 2021 describes it through the evolution of supersaturation (Ω) in a system with a dissolving phase and a growing phase. If there is a significant time difference between the supersaturation state ($\Omega 1$) at the onset of dissolution and the state ($\Omega 2$) marking equilibrium between dissolution and precipitation rates, then the dissolution-precipitation (DP) process is spatially uncoupled. This results in the product phase growing in open space rather than on the parent surface (see Figure 53). In other words, when the precipitation rate is slower than the dissolution rate, the precipitation process becomes rate-limiting, and coupling between the two phases is absent (Altree-Williams et al., 2015; Qian et al., 2010). This scenario is observed in the current study for the transformation of barite powder in the P, IB, and AR barites.

The dissolution rate of barite cubes is likely slower overall compared to powdered barites, which have larger surface areas and thus faster dissolution rates (see Equation 30). While higher barite dissolution rates lead to higher supersaturation levels with respect to witherite, it is probable that witherite precipitation can better keep pace with a slower dissolution rate. The

slower rate allows more time for dissolved carbonate to react with Ba to form witherite on the barite cube surface. This aligns with the suggestion by Putnis, 2015 and findings by Putnis, C.V., et al., 2005 that even small amounts of dissolved material can supersaturate the reaction front in CDP processes. In contrast, uncoupled processes likely release much larger amounts of Ba.

The spatial arrangement of barite plays a crucial role in uncoupled processes, influencing the interaction between particles and mass transfer during dissolution and precipitation. This, in turn, affects the spatial precipitation of witherite. Thus, the relationship between dissolution and precipitation rates is closely linked to the spatial arrangement of barite, with significant implications for the transformation processes observed in this study.

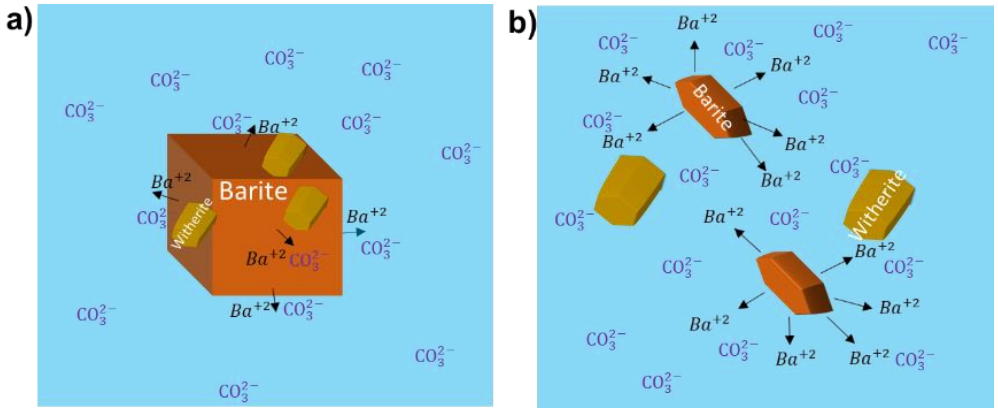

Figure 53. shows depictions that illustrate the difference between dissolution and precipitation processes that lead to coupled and uncoupled effects. (a) shows that Ba^{+2} is not diffusing away from barite and by reacting with dissolved CO_3^{2-}, witherite forms on barite cube. Ba^{+2} concentrations in the bulk solution are lower in (a) than in (b) that shows Ba2+ ions diffusing away from barite particles and reacting with CO_3^{2-}, forming witherite in the open space rather at barite particle surfaces.

The influence of P, IB, AR barite particles arrangement on the DP process

The distance of witherite formation sites from barite particles and cubes differ most likely due to the mobility of dissolved Ba into the bulk solution as discussed earlier, and such distances can be closely related to the barite spatial arrangement in the solution. For barite particles, discrete nature between particles exists since there is a void space between them compared to the cubes, which are in the form of packed barite units. This perspective was highlighted by Altree-Willams et al., 2015 as they indicate a short path for the ions released to the solution via dissolution of packed units before they react to form a new phase.

The discrete nature of particles makes the contact between them limited, leading to slower rates of interaction between dissolved Ba and the particle surfaces. The cubes, however, do not suffer from this effect due to the large surface contact, meaning that the dissolved Ba finds no

discontinuity like what exists between particles to travel through, therefore, it can react shortly with CO_3^{2-} on cube surface close proximity (see Figure 53). Therefore, it is fair to say that there is a diffusion barrier in the uncoupled processes that hinders the mass transfer of Ba between the particles due to the void space, though it is initially high compared to coupled processes since particles have larger surface area (A. Altree-Williams et al., 2015).

The diffusion barrier leads likely to the creation of localized supersaturations with respect to witherite between the barite particles as dissolved CO_3^{2-} has more time to react with Ba to form witherite in the open space. One the other hand, dissolved Ba from cubes encounters no such barrier as barite in this case is packed units, and that creates a continuous and interconnected network of supersaturated zones or as known as the reaction front in proximity of barite cube surfaces, leading to formation of witherite at the surfaces as discussed earlier.

The type IB barite has strontium content in its structure, which was found also in the witherite phase for cubes and particles as shown earlier. The spatial arrangement differences between barite particles and barite cubes can help in shedding light on aspects related to the evolution of Sr^{2+} in the solution during the processes.

The influence of spatial arrangement difference between the barite particles and barite cubes on the evolution Sr in the solution phase for IB type

The evolution of ions in the reaction medium is of importance specially in the context of the uptake of certain targeted ions such as Sr. The analysis via SEM-EDX (Figure *35*.a,b) for barite and witherite solid phases forming in an uncoupled DP process shows that the Sr/Ba ratio is consistent as well as in the solution phase. The consistency of the ratio in the solid phases suggests the formation of a solid solution between barium carbonate ($BaCO_3$) and strontium carbonate ($SrCO_3$) within the witherite crystal structure.

The fact that the Sr/Ba ratio remains relatively constant in both phases in the uncoupled DP indicates that the replacement of Ba by Sr during the transformation from barite to witherite occurs in a balanced manner, preserving the overall ratio. Such a preservation is a rather important aspect for strontium cycles in geological settings and factors leading to such a preservation will be dealt with in following sections. A similarly invariant Sr/Ba ratio was observed as well between the barite and witherite phases in CDP processes (Figure 27.a). However, there was a discrepancy found between Sr/Ba ratio in of the solid phases and the ratio of Sr/Ba in solution for cubes as it is initially about five times higher than the solid phases (Figure 28.b), whereas Sr/Ba ratio for IB particle solution is in consistent with solid phases ratio.

The factors that likely led to such discrepancy between Sr/Ba ratios of solid phases and solutions for cubes are discussed in detail in chapter 8.1.

The composition of the bulk solution in contact with barite particles plays a more relevant role in uncoupled DP processes since witherite formation occurs in the open space of the bulk solution and not in a spatially limited interfacial zone adjacent to barite particles as for the case of the cubes. This means the dissolution of ions from the barite particles whether from regular or enhanced dissolution sites can all simultaneously diffuse to a great extent into the bulk solution. As a consequence, the ion composition of solution and solid phase have almost the same stichometry. Therefore, the Sr/Ba ratio can be maintained in the bulk solution similar to solid phases ratio. In addition, the porosity effect on the mass transfer of dissolved carbonate is absent since the process is uncoupled. Therefore, the dissolved carbonate ions are supplied without any hindering with a constant rate leading to congruent processes of barite dissolution and witherite precipitation that contribute to the preservation of Sr/Ba ratio in the solution.

The spatial aspect, therefore, can be of importance when dealing with barite particles and barite cubes as it can play a crucial role in influencing processes such as mass transfer and local dissolution, which can directly impact ionic compositions and ratios within the bulk solution; such impact can lead to imbalances in the bulk solution, ultimately affecting the observed Sr/Ba ratio.

Exploring the potential possibilities for Sr distribution within witherite crystals

The incorporation of Sr in witherite is of topic interest since different studies were carried out for a better understanding as it can be involved in witherite formation from the carbonate recrystallization of Sr-barite in different geochemical settings. One of the earliest reported investigations of the (Ba,Sr)CO_3 solid solution was conducted by Chang, 1971 that uncovered a complete solid solution between $BaCO_3$ and $SrCO_3$ via precipitation of a wide range of Ba and Sr molar fractions by using mixtures of $BaCO_3$ and $SrCO_3$ as starting materials over a temperature range (350-750°C). This means that $BaCO_3$ and $SrCO_3$ can substitute for each other over the entire compositional range, creating a (Ba,Sr)CO_3 homogenous crystal.

Later, Baldasari and Speer, 1979 studied specimens of natural witherite solid solutions with microprobe analysis. Based on their results, Baldasari and Speer, 1979 revealed limited substitution of strontium in the witherite lattice (a mean of 3.3 mole percent), which they attributed to the presence of a miscibility gap between witherite and strontianite. Consequently, Baldasari and Speer, 1979 suggested an unevenly distributional behavior of (Ba,Sr)CO_3, meaning that the (Ba,Sr)CO_3 crystal can during the formation have $BaCO_3$ and $SrCO_3$ as

distinct phases within a (Ba,Sr)CO_3 single crystal, which implies the crystal is heterogeneous and its compositions show oscillatory zoning effect. However, this creates a clear discrepancy to the observations of Chang, 1971. One way to explain such discrepancy by Baldasari and Speer, 1979 was to suggest a mimical behavior for (Ba,Sr)CO_3, meaning that Sr distribution in witherite lattice mimics its counterpart distribution in the pre-existing barite, which is known to have uneven compositional distribution.

To investigate this matter further, Prieto et at., 1997 took a different approach by synthesizing crystals comprising (Ba,Sr)CO_3 and (Ba,Sr)SO_4 solid solutions using a counterdiffusion technique through a column of porous silica hydrogel and analyzed them via electron microprobe to examine the effect of supersaturation on the distribution of materials between solid and aqueous phases. The results of Prieto et al., 1997 showed that for the case of (Ba,Sr)SO_4 solid solution where the solubility products of the endmembers vary significantly ($K_{sp,barite} = 10^{-9.605}$ and $K_{sp,celestite} = 10^{-6.63}$), nucleation from aqueous solutions tends to occur in a bimodal manner. In this system, there is a strong tendency for Sr partitioning into the solid phase, resulting in only a narrow range of aqueous-phase compositions that can coexist in equilibrium with intermediate solid solutions. Despite a wider range of aqueous solutions capable of nucleating intermediate solid solutions at high supersaturations, the bimodal effect persists. On the other hand, the (Ba,Sr)CO_3 solid solution, with closer endmember solubility product values ($K_{sp,witherite} = 10^{-8.67}$ and $K_{sp,strontianite} = 10^{-9.27}$), prefers to nucleate evenly, which leads to a great deal of fluid compositions to be in equilibrium with intermediate solid solution. Even during high supersaturation, (Ba,Sr)CO_3 nucleation was occurring in a stoichiometric style where substituting ions incorporate in the solid phase nearly with the same ratio in the aqueous phase, resulting in partition coefficients approaching unity.Prieto et al., 1997 suggested that natural (Ba,Sr)CO_3 that was formed from a carbonate medium alteration for (Ba,Sr)SO_4 could indeed lead to copying the compositional distribution of the precursor (Ba,Sr)SO_4 into the resultant (Ba,Sr)CO_3.

Though the aforementioned works provide excellent highlights onto the behaviors of the (Ba,Sr)CO_3 solid solutions in experimental and natural conditions that led to valuable insights into the different behaviors such solid solutions, the current study sheds light on this system with a different perspective through a distinct experimental approach. The present study allows for an a direct observation of the effect of a natural precursor barite with incorporated Sr on the resulting (Ba,Sr)CO_3 solid solution.

The atomic percent values obtained by SEM-EDX analysis for Sr in barite and witherite phases for particles and cubes were remarkably close (Figure 27.a and Figure 35.b), which supports the suggestion that there is a precursory effect during the dissolution and precipitation of Sr-barite and Sr-witherite. This means that barite was dissolving in an uneven ionic style for Sr and Ba, which was maintained in the solution lead witherite to form Sr/Ba ratio similar to copy the solution ratio. This eventually resulted in witherite formation that mirrored the compositional distribution of Sr in barite, that is known to be uneven (Baldasari and Speer, 1979; Prieto et at., 1997; Weber et al., 2018; Poonoosamy et al., 2021). Though SEM-EDX results for the current study show an even distribution, there is a possibility that the uneven distribution nature of strontium within barite structures is unrevealed in the present study possibly due to spatial limitations in SEM-EDX analysis, which prevents the detection of uneven Sr distribution in IB. A study in this regard by Weber et al., 2018 shows that even at rather low Sr/Ba ratio, the uneven distributary nature was shown to persist by using the Atom Probe Tomography (APT) technique.

The geochemical fate of Sr upon (Ba,Sr)SO_4 dissolution and (Ba,Sr)CO_3 formation: Kinetic and thermodynamic perspectives

The geochemical cycling of Sr between (Ba,Sr)SO_4 and (Ba,Sr)CO_3 in different settings is quite interesting due to the environments witherite mostly forms in. Typically, witherite is believed to form in carbonate media via barite alteration in different natural environments, a process that is pointed out by Baldasari and Speer, 1979 to be the most common for witherite formation as it was documented to be the case in various studies (Weller et al., 1952; Helz and Holland, 1965). This alteration process was suggested by Hancox, 1934 to be the prevalent mean of numerous occurrences of witherite formation in Great Britain.

Baldasari and Speer (1979) observed that the natural distributions of Ba-Sr sulfates and carbonates are similar, suggesting that Ba and Sr tend to separate in nature. This separation is maintained during the transformation of barite to witherite when carbonate is introduced. The ability for Ba and Sr to react and form distinct solid phases, regardless of the carbonate-to-sulfate ratio in the reaction medium, as noted by Barton (1957) and Gundlach (1959), ensures that this separation is preserved.

This means that when barite recrystallizes into witherite, the geochemical separation of Ba and Sr that occurred in the sulfate system before the transformation is maintained. As a result, the Sr content in the witherite will be similar to that in the original barite. The process prevents

equilibration between the carbonate-sulfate or carbonate-carbonate phases, meaning that Ba and Sr do not mix between these phases during carbonation.

The preservation of this Ba-Sr separation is also confirmed by Baldasari and Speer (1979) in their study of various natural samples, where they found that this separation was consistently maintained across different deposits.

The results of present study would support the preservation of Sr content in disequilibrium systems since an alteration of natural IB barite containing Sr was carried in a disequilibrium condition where supersaturation level was high (see Figure 50) and the Sr content in both phases was found to be preserved as shown earlier (Figure 27.a, Figure 35.a and Figure 35.b). However, the current study suggests an additional possibility for the process through which Sr content is preserved by considering the congruent effect as discussed before.

To obtain an understanding of the fate of Sr under equilibrium conditions, Baldasari and Speer, 1979 preformed thermodynamic calculations considering the following exchange reaction:

$$BaSO_4 + SrCO_3 \rightleftharpoons SrSO_4 + BaCO_3$$

Equation 31

The calculations showed that the recrystallization of (Ba,Sr)SO_4 to (Ba,Sr)CO_3 leads to a considerable difference in Sr content between the two phases. The difference is indicated by the equilibrium constant for the exchange reaction between barite and witherite, which shows a strong tendency for strontium to preferentially associate with the carbonate phase during the alteration process. The results of calculations indicate that as witherite becomes richer in Ba, it consumes more Sr until the whole barite bulk is recrystallized into witherite with a composition that is similar to the initial barite composition.

One of the samples that Baldasari and Speer, 1979 studied was a barite-witherite coexisting sample, meaning that the process of barite dissolution and witherite precipitation was coupled, similar to the effect of CDP seen in the cubes of the present study. The barite was found to be replaced greatly by witherite and the Sr content was less than 0.02 mole % for barite, whereas witherite exhibited a significantly higher strontium content of 11 mole percent. If such system is to be considered closed with respect to Ba and Sr. Such difference in Sr content between barite and witherite suggests that Sr was preferentially released from the barite during the coupled dissolution and precipitation process, likely due to the interaction with the carbonate solution. This selective release of Sr indicates that equilibrium conditions were reached between the phases as system behaved similar to the calculated-equilibrated systems shown in Equation 31 in terms of the Sr depletion from barite and preferential partitioning into witherite.

The above-mentioned discussion indicates that the pathwy of Sr in a system where Sr containing barite is recrystallized into witherite to escape incorporation into witherite is minimal, regardless of whether the system is governed by kinetics or thermodynamics. An important observation by Baldasari and Speer, 1979 underscores this point, highlighting the significance of ionic radii for Ba (1.47 Å, Yoshida et al., 2014) and Sr (1.31Å, Liang, et al., 2020). The similarity in ionic radii between these ions facilitates easier substitution of Sr into the crystal lattice of witherite, regardless of whether the system is in equilibrium or not. The recrystallization of Sr-barite into Sr-witherite with considerations and perspectives discussed above is of importance as it can assist in a broader understanding of the fate of other cations such as Ra in geological settings during the recrystallization of sulfate systems into carbonates. This will be further explored when discussing the transformation of barite into witherite in the presence of Ra.

The effects of different carbonate concentrations on the transformation processes

The transformation processes are clearly carbonate concentrations dependent as Figure 29 , Figure *34*, Figure A.1 and Figure A.2 show. The increase of carbonate concentration leads to an increase in witherite formation regardless of the type of barite and pH value. This effect of the different carbonate concentrations on transformation rates was observed in numbers of previous studies (Arai and Toguri, 1984; Gong et at., 1992; Castillejos and Uribe, 1996). These previous studies proposed the shrinking core model that includes diffusion rates to describe the correlation between the increase of carbonate concentration and the transformation rate since the growth processes were coupled. The shrinking core model would not be applicable for transformation of the barite particles into witherite since the process is uncoupled, however, the positive correlation between witherite formation rate and carbonate concentration can be generally described by Fick's first law of diffusion. The Fick's law as follows:

$$J\left(\frac{dc}{dt}\right) = -D\,\frac{\Delta c}{\Delta x}$$

Equation 32

where J is the diffusional flux that is the change of carbonate concentration (dc) over change of time (dt), D is the diffusion coefficient, representing the ability of carbonate ions to move through the solution, Δc is the difference in concentration between two points over a certain distance Δx.

This equation illustrates that as the concentration gradient ($\frac{\Delta c}{\Delta x}$) increases, indicating a higher difference in concentration over a given distance, the diffusion rate ($\frac{dc}{dt}$) of carbonate ions also increases, leading to more carbonate ions reaching the surface of the barite. In another word, when CO_3^{2-} concentration in the solution is 0.1M compared to when it's 0.01M, the concentration gradient ($\frac{\Delta c}{\Delta x}$) would likely be higher and this is because a higher concentration of CO_3^{2-} ions in the solution would create a steeper change in concentration over a given distance (Δx), leading to a faster rate of witherite formation during barite dissolution.

The effect of solution pH on the transformation processes

The transformation rate of barite to witherite exhibits a clear dependency on pH, as evidenced by Figure 34, which is consistent with prior studies on sulfate-minerals alteration into carbonate-minerals (Gong et al., 1992; Castillejos and Uribe, 1996). The investigation into pH variation impact on barite carbonation revealed that reducing pH through HCl addition led to diminished witherite transformation rates. This phenomenon is attributed to the protonation of carbonate ions, reducing the concentration of CO32- ions. These findings align with literature (Castillejos and Uribe, 1996), indicating that deviations from the natural pH range of carbonate solutions (11-12) can negatively influence the witherite transformation, which necessitates higher carbonate concentrations for efficient transformation, even at moderately reduced pH levels like 9.50. The addition of hydrochloric acid triggers protonation reactions, wherein HCl reacts with carbonate ions to form carbonic acid (H2CO3), which subsequently dissociates to produce bicarbonate ions (HCO_3^-) and hydrogen ions (H^+). As this process reduce pH, it favors the formation of less reactive bicarbonate ions and hindering the carbonation reaction of barite.

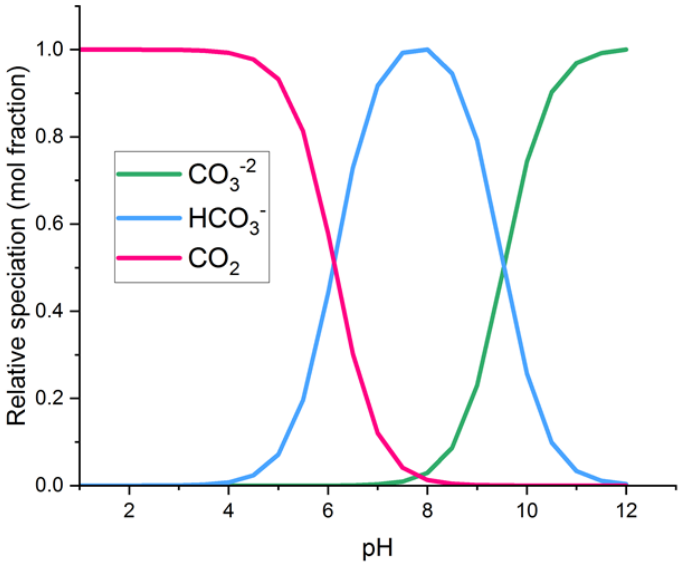

Figure 54. Carbonate species distribution at different pH values at 25 °C. The plot generated using PHREEQC code and the PHREEQC database (Parkhurst and Appelo, 1999).

8.3 Barite precipitation in the presence of ^{226}Ra

The barite particles that resulted from coprecipitation of Ba and ^{226}Ra with sulfate took dendritic barite morphologies. Such particles maintain the crystallographic information of the barite, however, there are clear orientation preferences shown by diffraction analysis.

The solution analysis show that ^{226}Ra was indeed removed from solution after 25 days reaction time. However, ^{226}Ra was found to preferably stay in solution rather than incorporate into barite as the experimental partition coefficient was found to be less than unity (0.34 ± 0.14).

The influence of temperature and supersaturation on the barite growth

Temperature is a crucial factor affecting the morphology of barite. Different morphologies are observed at various temperatures, even with all other reaction conditions remaining constant (Wang et al., 2021). At room temperature, barite tends to form simple granular or leaf-like structures (Wang et al., 2021; Wong, Jaworski and Nienow, 2001). Upon temperature elevation up to 200° C, barites exhibit a diverse range of forms, including rod, granular, plate, dendritic, X-shaped, and T-shaped crystals (Wang et al., 2021). These observations highlight that the morphology of barite is significantly influenced by temperature and are consistent with findings of the current study , showing that barite particles were dendritic at 60 ^{0} C (Figure 45), whereas at room temperature nano particles formed.

Supersaturation levels play a crucial role in determining the morphology of barite (Wang et al., 2021). Higher supersaturation ratios result in the formation of numerous small spherical nanoparticles, while lower supersaturation levels lead to the development of leaf-like structures (Li, Xu and Luo, 2007). At elevated temperatures, the solubility product of barite increases,

further influencing the degree of supersaturation and resulting in the formation of dendritic crystals from solutions with high barium chloride concentrations (Shikazono, 1994; Wang et al., 2021). This aligns with the present study findings, where the barite supersaturation level is high (7.65) and the solubility product increases at 60°C ($K_{sp,\ barite} = 10^{-9.65}$), which most likely contributed to the formation of dendritic particles. Figure 55 illustrates the different stages that lead to the formation of dendritic barite particles.

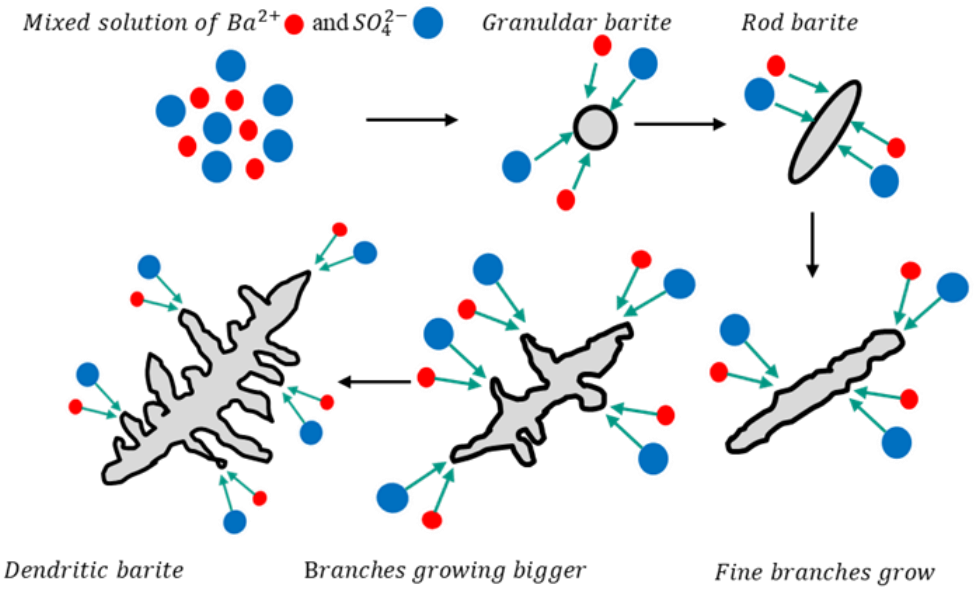

Figure 55. shows different stages of barite dendritic particle growth where it starts with granular and rod particles followed by random growth and abundant of defect points that result in lattice disturbance and random growth, which eventually leads to formation of dendritic barite (adopted from Wang et al., 2021).

On the uptake of ^{226}Ra during barite formation at 60° C

Barite has been suggested for long time to be an effective mineral in taking up radium into its structure. Multiple studies in the past showed the high ^{226}Ra uptake by barite via different approaches at 25° C. The easiest study was by Doerner and Hoskins, 1925 who arrived to an equilibrium partition coefficient (1.8 ± 0.1) via 6 days of barite precipitation in the presence of radium. Later, Heberling et al., 2018 derived a partition coefficient (2.1 ± 0.5) through recrystallizing barite in the presence of radium for 4.08 years.

The experimental partition coefficient obtained in the present study (0.34 ± 0.14) is much lower than those reported in by the previous studies. The temperature elevation can play a significant role in determining the partitioning of radium into barite. To illustrate such role, the non-ideality parameter that was calculated in this study (0.84) can be used along the barite and radium sulfate endmembers solubility at 60^0 C ($K_{sp,\ barite} = 10^{-9.65}$ and $K_{sp,\ RaSO4} = 10^{-9.66}$ by Krumgalz, 2018 and Langmuir and Melchior, 1985, respectively) to arrive to the

theoretical partition coefficient at 60^0 C, which is (0.42). When using barite and radium sulfate solubility products at 25^0 C ($K_{sp,\ barite} = 10^{-9.97}$ and $K_{sp,\ RaSO4} = 10^{-10.26}$ by Brown et al., 2019), the theoretical partition coefficient becomes (0.92). The theoretical partition coefficient at 60 °C is lower than the theoretically and experimentally obtained by previous studies, underscoring the impact the temperature on radium incorporation into barite. The experimental partition coefficients for the RB series is plotted in Figure *56* against the theoretical partition coefficients, showing the different aspects mentioned above.

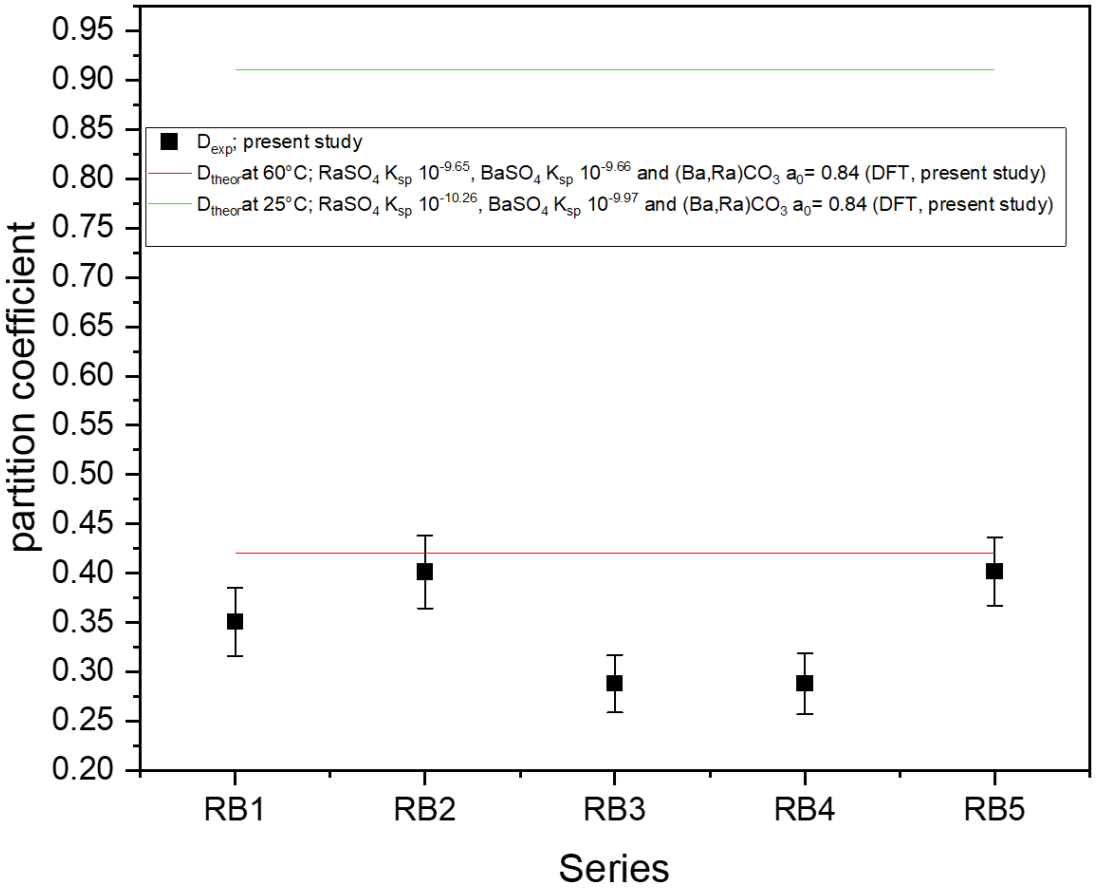

Figure 56. shows the experimental partition coefficients obtained in this study compared to the theoretical partition coefficients using the non-ideality parameter obtained in this study for radium incorporation into barite (0.84) and solubility products at 60°C ($K_{sp,\ barite} = 10^{-9.65}$ *and* $K_{sp,\ RaSO4} = 10^{-9.66}$ by Krumgalz, 2018 and Langmuir and Melchior, 1985, respectively) as well as solubility products at 25°C ($K_{sp,\ barite} = 10^{-9.97}$ *and* $K_{sp,\ RaSO4} = 10^{-10.26}$ by Brown et al., 2019).

The thermodynamic Lippmann and Rooseboom diagrams shown in Figure 57 can help in bringing forth visual illustrations on temperature elevation impact on radium uptake by barite. The Lippmann diagram can be constructed using Equation 9, Equation 10, Equation 11, Equation 12 and Equation 13 by superimposing radium activity fractions in the solution (Ra_s) and radium molar fractions in the solid (Ra_{aq}) on the x-axis, whereas the y-axis is total solubility product at equilibrium ($\log \sum\prod_{eq}$) for $(Ba, Ra)SO_4$ solid solution.

For the Lippmann diagram and upon temperature increase, the solutus and solidus curves move upwards, increasing the total solubility product at equilibrium. This reduces radium partitioning into barite, enriching the solution with radium. The Lippmann diagram shows that higher temperatures shrink the solutus and solidus curves, indicating a shift towards equilibrium where radium is less preferentially partitioned into the solid. This is preceded by an alyotropic point where radium concentrations in the solution and solid equalize. As temperature rises, this point moves closer to the radium sulfate endmember, causing the curves ahead of it to shrink and the solution to become richer in radium.

In the Roozeboom diagram, radium activity fractions in the solution on the in the x-axis correspond to different molar fractions of radium in the solid on the y-axis, which decrease with increasing temperature. The straight regions in these curves represent the shrinkages seen in the Lippmann diagrams, becoming more pronounced at higher temperatures. The alyotropic points, observed before the straight regions, show the equalization of radium fractions in the solution and solid.

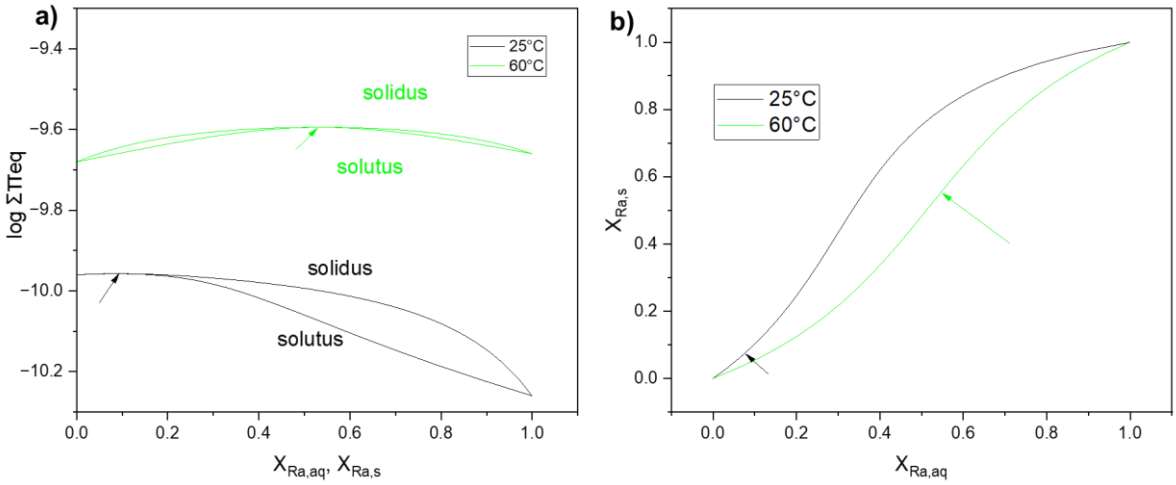

Figure 57. show (a) Lippmann diagram and (b) Roozeboom diagram total solubility product of the solid solution (Ba,Ra)SO4 at different temperatures. The solubility products of the endmembers change of temperatures, and these different solubility products were obtained from Brown et al., 2019.

8.4 The reaction of $(Ba, Ra)SO_4$ with carbonate solutions

The current study investigated the interaction of carbonate solutions with radium-containing barite under varying conditions. It was observed that SL barite particles that were pre-equilibrated with NaCl (0.1M) and equilibrated with ^{226}Ra in carbonate solution (0.1M) at pH levels (10 and 11) did not result in the formation of witherite. Conversely, barite precipitated in the presence of ^{226}Ra in carbonate solution (0.15M) at pH (11) showed witherite formation

at later stages of the reaction time. In both scenarios, the transformation process was notably slow, with minimal or no witherite formation, likely due to the stability of $(Ba, Ra)SO_4$.

The impact of ^{226}Ra on barite structural properties and stabilities:

1-The long term treated barite

The morphological changes the SL-Ra barite particles show externally and internally after the long transformation with ^{226}Ra points towards critical impacts of ^{226}Ra on barite structure and, therefore, on its reactivity. The fact that these particles show features, which were found to be preserved before and after the rection with carbonate solutions, similar to those that were observed in previous studies (Heberling et al., 2018 Weber et al., 2017) such as the increase of diffraction pattern peak intensities, surface feature changes, existence of deep holes and particles growth together (Figure 18, Figure 19,Figure 36 and Figure 37), indicates that particles highly likely possess the same structural properties that previous studies found as well. The sharper peaks of RaLT-SL $(Ba, Ra)SO_4$ particles after the 7.08 years treatment with ^{226}Ra in comparison with raw SL(Figure 37), which was found as well by Heberling et al., 2018 after 4.08 years reaction time, indicates the increase of crystallinity of such particles. The increase of the crystallinity leads to the stability of particles as crystallinity by definition means the reduction in surface energies. Such increase of $(Ba, Ra)SO_4$ particles crystallinity was suggested by Heberling et al, 2018 to be caused by internal restructuring of the $(Ba, Ra)SO_4$ particles.

The suggestion of Heberling et al, 2018 is valid when considering the study that was carried out by Weber et al., 2017 through investigations with transmission electron microscopy TEM-EDX combined with FIB-SEM on SL $(Ba, Ra)SO_4$ particles resulted from transformation of SL barite in the absence and presence of ^{226}Ra. The results of FIB-SEM cuts for $(Ba, Ra)SO_4$ particles showed internal nano pores in the form of layers due to different porosity densities similar to the ones found by the current study shown in Figure 33.c. These pores were found to be stable when barite particles were recrystallizing in the absence of ^{226}Ra for different reaction periods over 2.46 years. When ^{226}Ra of different concentrations was added to react with SL barite particles for different reaction intervals over 3.84 years, the pores started evolving by merging into each other to form macropores as a mean of surface energy minimization as suggested by Weber et al., 2017. The pore layers then disappeared and only macropores remained. The process of nano pores mergence into macropores were shown by Weber et al., 2017 to be occurring towards the outer surfaces of the particles, to which they attributed the

surface deep holes they found. These holes are rather similar to the surface deep holes that were found in the particles of the current study before and after carbonation (Figure 18 and Figure 36). This could be an indication that it is likely that $(Ba, Ra)SO_4$ particles, which were used as starting materials for the contact with carbonate solution, had undergone the same internal restructuring process during 7.08 years reaction period with ^{226}Ra.

These effects observed in $(Ba, Ra)SO_4$ particles by the current and previous studies, namely the increase of diffraction peaks intensities, the deep holes seen in the surfaces of the particles and the development of the massive layer shown by Weber et al., 2017, suggest that the reaction with ^{226}Ra led to the $(Ba, Ra)SO_4$ particles to be low in reactivity upon reacting with carbonate solution and hence, the absence of witherite formation for the given reaction timeframe.

2-The precipitated barite

Though barite that was principiated in the presence of ^{226}Ra resulted in dendritic particles that possess features which should increase their reactivity due to high surface area, surface defects and irregularities as well as porosity (Figure 39), the reaction of such particles with carbonate solutions (0.15M, higher than any carbonate solution concentration used with other barites in this study) and pH (11) did not show witherite formation until later stages of the reaction time. This indicates that reaction kinetics under the given condition are slow, therefore, transformation progress is limited within the given reaction time.

The hindrance of transformation progress is clearly revealed by predomination of dendritic particles that persisted even after witherite formation started at day 21 of the reaction (Figure 45). Moreover, the hexagonal witherite particles appeared to have remnants of dendritic barite structures, indicating that witherite was forming on the surfaces or within the existing barite dendrites. This combined morphology suggests a slow transformation process, with witherite formation likely occurring within the proximity of pre-existing barite. The witherite particles exhibit rather pronounced hexagonal particles with smooth surfaces as unprecedented sheet-like growth, which all could hint at the slow interaction between the dendritic barite particles and carbonate solution that resulted in the minimal witherite formation.

The slow witherite formation can be attributed to the structural stability imparted by ^{226}Ra to the dendritic barite particles. This stability likely results from internal restructuring to minimize surface energy, leading to less reactive surfaces. The ^{226}Ra incorporation into the barite structure creates a more ordered and stable crystalline lattice, which reduces the surface energy and, consequently, the reactivity of the particles. This internal restructuring aligns with

previous findings by Heberling et al., 2018 and Weber et al., 2017, where increased crystallinity and formation of stable rims were observed in ^{226}Ra-treated barite particles.

The slow kinetics of witherite formation in the presence of ^{226}Ra-treated barite particles suggest that ^{226}Ra plays a crucial role in enhancing the structural stability of barite. This enhanced stability hinders rapid mineral transformation processes, such as witherite formation, by creating a more stable and less reactive surface. The stability of ^{226}Ra-barite particles is particularly significant in environmental and industrial contexts, such as deep geological disposal. In these settings, the stability of these particles means that ^{226}Ra is less likely to dissolve and migrate into different environmental compartments.

The effect of long term ^{226}Ra treatment on Ba dissolution from $(Ba, Ra)SO_4$ particles in carbonate solutions

The fact that Ba solution concentrations in presence of long treated $(\mathrm{Ba, Ra})\mathrm{SO_4}$ RaLT-Ra batches are below barite equilibrium concentrations by one order of magnitude after 30 days of reaction with carbonate solutions (0.1M) at pH 10 and 11 (Figure 38) confirms the internal restructuring of $(\mathrm{Ba, Ra})\mathrm{SO_4}$ particles proposed by this study and previous ones as discussed before.

The comparison of Ba concentration evolution for long treated $(\mathrm{Ba, Ra})\mathrm{SO_4}$ against Ba evolution of the shortly treated SL barite in the absence of ^{226}Ra (Figure 35.a) shows a considerable difference between the two barite types. Ba concentration in experiments with long treated $(\mathrm{Ba, Ra})\mathrm{SO_4}$ is far below the equilibrium concentration, whereas the shortly treated barite started with Ba concentrations rather close to the Ba equilibrium concentration of barite. This strongly indicates that Ba is not easily dissociated or dissolved from the long treated $(\mathrm{Ba, Ra})\mathrm{SO_4}$, as Ba ions are more tightly associated with the crystal lattice.

When comparing the long treated $(\mathrm{Ba, Ra})\mathrm{SO_4}$ particles to the long treated LT-SL barite in the absence of ^{226}Ra, which resulted in the formation of witherite, the similarity between the two Ba evolutions can be attributed to two factors. Firstly, the morphology changes during the long time treatment likely affected the reactivity of the particles even in the absence of ^{226}Ra, though this change is most likely not as profound as in the presence of ^{226}Ra, since witherite was found to form in the absence of ^{226}Ra. Secondly, the formation of the rough layer that was found to develop on barite particles (Figure 30.d) can hinder Ba release into the bulk solution. These two factors could explain the observed similarity in Ba evolutions.

The slow pace of Ba concentration evolution in experiments with long treated $(Ba, Ra)SO_4$ can be explained by the modified homogeneous recrystallization model developed by Heberling et al., 2018. This model describes the slow ^{133}Ba uptake kinetics for the same $(Ba, Ra)SO_4$ particles used here but for a 4.08-year reaction period. Heberling et al., 2018 developed this model due to the lack of fitting encountered when employing homogeneous and heterogeneous models for ^{133}Ba uptake described by Curti et al., 2005, which account for much faster uptake. However, the modified model was suitable and showed good agreement between the experimental data and the model. This further indicates how differently Ba ions dissolve from $(Ba, Ra)SO_4$ particles upon contact with carbonate solution due to the reordering the particle structures occurring during the long treatment period with ^{226}Ra.

The evolution of Ba and ^{226}Ra concentrations in solution from precipitated barite

The reaction of RBC or barite precipitated in the presence of ^{226}Ra batches with carbonate solution (0.15M) at pH (11) resulted in a minimal release of Ba into the carbonate bulk solution, as shown in Figure 46.a. This minimal release is similar to the limited Ba release observed for the long treated $(Ba, Ra)SO_4$, further confirming the stabilizing effect of ^{226}Ra on barite.

A critical observation in the reaction of RBC batches with carbonate is the release of ^{226}Ra into the bulk solution, as displayed in Figure 46.b. This release of ^{226}Ra was not seen in any of the long treated $(Ba, Ra)SO_4$ batches that reacted with carbonate for 30 days, suggesting a difference in ^{226}Ra distribution within the structures of the two barite types.

Previous studies by Weber et al., 2017 investigated the distribution of ^{226}Ra within long-treated particles and the internal restructuring of SL barite with ^{226}Ra over 3.84 years. They suggested that ^{226}Ra homogeneity increased within the particles over time, eventually becoming completely homogenized at the later reaction stages. This likely applies to the ^{226}Ra distribution within the long-treated particles used in the current study, which were reacted with ^{226}Ra for an even longer period, leading to greater homogeneity. As a result, ^{226}Ra was likely strongly bound to the lattice of these particles, making its dissolution unlikely under the experimental conditions of this study.

On the other hand, the ^{226}Ra distribution within the precipitated $(Ba, Ra)SO_4$ particles appears to differ from that of the long treated particles. The dendritic morphology of the precipitated particles (Figure 45) suggests higher reactivity due to their large surface area relative to their bulk volume. Dendritic particles have a flat, branched structure with numerous surface pores, which increases their exposure to the carbonate solution. This high surface area-to-volume ratio

makes the ^{226}Ra in dendritic particles more accessible to the carbonate solution, facilitating its release.

Another significant difference between the long-treated and precipitated barite is the treatment time and the reaction mechanism. The long-treated particles underwent extensive internal restructuring over years, leading to a stable and homogeneous ^{226}Ra distribution. In contrast, the precipitated particles formed more quickly, with ^{226}Ra possibly remaining on the surface or within easily accessible pores. This surface-bound ^{226}Ra is more susceptible to dissolution when exposed to the carbonate solution.

Reaction dynamics of precipitated $(Ba, Ra)SO_4$ particles with carbonate solution

The reaction of precipitated $(\mathrm{Ba, Ra})\mathrm{SO_4}$ particles with carbonate solution resulted in the release of ^{226}Ra, observed consistently across all reaction intervals (Figure 46.b). The ^{226}Ra / Ba ratios shown in Figure 46.c are closely consistent. This observation parallels the scenario seen in the transformation of IB $(\mathrm{Ba, Sr})\mathrm{SO_4}$ into witherite, where the Sr/Ba ratio remained constant in both the solution and the solid phases. This phenomenon was attributed to a kinetic effect, where the Sr/Ba ratio of the precursor $(\mathrm{Ba, Sr})\mathrm{SO_4}$ was preserved in the solution and subsequently in the formed witherite, as discussed earlier in section 8.2.

Similarly, the congruent release of ^{226}Ra and Ba from $(\mathrm{Ba, Ra})\mathrm{SO_4}$ during dissolution and witherite precipitation suggests that the ^{226}Ra / Ba ratio is maintained in the solution and likely in the solid phase as well. The surface morphology of the witherite particles, which exhibit remnants of dendritic structures (Figure 45), suggests that witherite forms closely attached to the dissolving $(\mathrm{Ba, Ra})\mathrm{SO_4}$ particles. This proximity likely limits the escape pathway of ^{226}Ra , ensuring its uptake by the forming witherite and preserving the ^{226}Ra /Ba ratio.

The consistency of the ^{226}Ra /Ba ratio in solution and solid phases is further supported by the observation that even when witherite forms with less association to IB $(\mathrm{Ba, Sr})\mathrm{SO_4}$ particles (see Figure 30.f) than witherite forming form $(\mathrm{Ba, Ra})\mathrm{SO_4}$ dendritic (Figure 45.d), the Sr/Ba ratio remained consistent. This indicates a strong likelihood that the ^{226}Ra /Ba ratio is similarly preserved in the $(\mathrm{Ba, Ra})\mathrm{SO_4}$ when witherite transformation occurs.

8.5 The precipitation of witherite in the presence of ^{226}Ra

The experimental results of witherite precipitation in the presence of ^{226}Ra reveal important insights into the structural impacts of radium incorporation on witherite that is revealed by the diffraction analysis via XRD patterns and microscopy investigation via SEM method.

The solid analysis

XRD analysis: structural characteristics

The experimental results of witherite precipitation in the presence of ^{226}Ra reveal important insights into the structural impacts of radium incorporation on witherite. XRD patterns, as shown in Figure 47, indicate that witherite formed in both radium-containing and radium-free conditions exhibits similar peak positions, suggesting that the overall crystal structure remains consistent despite the presence of ^{226}Ra.

However, a closer examination of the diffraction patterns reveals subtle differences in peak intensities, particularly at higher angles. The lower intensities observed for the Ra-witherite peaks compared to radium free witherite can be attributed to the smaller quantity of solid measured for safety reasons, rather than a significant structural deviation. This safety constraint likely caused an apparent reduction in peak intensities, especially at higher diffraction angles. Despite this, peaks at lower angles (19.48^0 and 19.89^0) exhibit similar intensities between radium containing and radium free witherite, indicating that radium does not drastically alter the basic crystal structure of witherite.

Interestingly, witherite containing higher radium concentrations shows increased peak intensities at specific angles (19.48^0 and 24.24^0) compared to both low radium and radium free witherite. This suggests that radium incorporation may influence the crystallographic planes of witherite, potentially enhancing the stability or altering the density of certain planes within the crystal lattice. Such variations in peak intensities highlight the nuanced role that ^{226}Ra plays in the crystallographic characteristics of witherite.

SEM analysis of morphological aspects

The inspection of the images obtained by SEM in Figure 48 reveals that the crystallographic features of witherite particles are preserved as they show to a good extent hexagonal shape. However, the particles spatial arrangement differs depending on the size of the particles that differ as well. The images in Figure 48 whether for ^{226}Ra contained or free witherites, all show

large particles with micrometer sizes that clearly show the common witherite hexagonal prismatic crystal structures. Though large particles appear to have tiny particles at their surface, these tiny ones most likely are not attached to the large ones, but rather loosely associated with large particles surfaces.

The other particles that are forming ^{226}Ra-witherite and witherite are small ones with nano-size that show prismatic features, although not as clear as the large ones. This shape unclarity is related to the fact that these small particles are attached to one another and to the large ones in a back-to-back attachment style, leading to the hiding of bipyramidal ends that reveal the distinct shapes of witherite and other analogous aragonite mineral types. The back-to-back attachment leads to the formation of larger rod-like structures of witherite.

A close inspection of these rods reveals the following: the rods are mostly formed out of these small particles, the large particles can contribute to these rods by locating mostly at the rods ends, and the rods appear seemingly not to attach to one another, meaning that there is no observable side attachment between the particles, but limited to the ends.

This formation mechanism aligns well with the dipole driven self-assembly model proposed by Zhou et al., 2009. In their study, $BaCO_3$ nanocrystals were synthesized in the presence of a strong polar solvent and subsequently washed to remove organic stabilizers. When these washed nanocrystals were redispersed in deionized water, they assembled into organized mesocrystals of $BaCO_3$. The dipole-dipole interactions between the assembled $BaCO_3$ nanorods were found to be the driving force for the formation of these organized mesorods.

Applying this model to our experiments, the witherite rods observed can be attributed to similar dipole-dipole interactions. During the synthesis, Na_2CO_3 was added to $BaCl_2$ and $BaCl_2$+^{226}Ra solutions, precipitating witherite and ^{226}Ra-witherite. After the precipitation reaction, where the concentrations of $BaCl_2$ (8.36E-3 M) and Na_2CO_3 (0.1 M) were relatively high and led to rapid particle formation, subsequent washing cycles with deionized water were carried out. These washing cycles possibly helped remove excess reactants and ions from the particle surfaces, mitigating their influence on particle alignment and assembly. As a result, the $BaCO_3$ nanoparticles could undergo self-assembly driven by dipole-dipole interactions, forming larger mesocrystals and rod-like structures.

Moreover, Schwarzer and Peukert, 2002 have showed that agglomeration can be controlled by changing the composition of the suspension in which precipitation takes place. Increasing the concentration Ba ions lead to stabilization of the particles against dipole-dipole interactions. This stabilization is achieved by the adsorption of Ba ions onto the particle surfaces, creating a

positive surface charge that prevents particles from aligning and forming larger structures. Therefore, the removal of these stabilizing Ba ions through washing cycles facilitates the self-assembly process, leading to the formation of witherite nanorods.

The difference in size for witherite particles found in both ^{226}Ra-contained and free samples is an outcome of the present study, as the experimental conditions were kept strictly the same for all batches throughout the precipitation durations. One possible reason for such a difference is incomplete mixing during the precipitation processes, leading to the creation of zones with different concentrations of reactants, which manifested into different particle sizes.

The ^{226}Ra partition coefficient into witherite

Though the experimental method used in the current study to obtain the partition coefficient involved a high precipitation rate (7.32) differing from Yoshida et al., 2014, who employed the free drift method by adjusting pH via bubbling/degassing CO_2 for coprecipitation under equilibrium conditions, both studies converge to similar partition coefficients as shown in (Figure 58). This similarity suggests that the limited partitioning of ^{226}Ra into witherite is a robust finding, relatively independent of the specific experimental conditions. The similarity in results, despite the differences in methodologies, underscores the low affinity of ^{226}Ra for witherite.

The partition coefficient of ^{226}Ra into witherite was thought to be higher than above stated values of the current study and Yoshida et al., 2014. The radium carbonate solubility product ($K_{sp,\ RaCO_3} = 10^{-8.30}$) that was obtained by Langmuir & Melchior, 1985 via the extrapolation from the witherite solubility product of witherite ($K_{sp,\ witherite} = 10^{-8.58}$) was long time accepted. When using the value solubility products ($K_{sp,\ RaCO_3} = 10^{-8.30}$) and ($K_{sp,\ witherite} = 10^{-8.58}$) from Langmuir & Melchior, 1985 as well as the non-ideality parameter obtained in this study (0.58) for radium substitution of barium in witherite (0.58) into Equation 24, the partition coefficient is (0.45). This value is much higher than what's reported here and reported by Yoshida et al., 2014 (Figure 58). However, when using the solubility product ($K_{sp,\ RaCO_3} = 10^{-7.57}$) that was obtained via using a thermodynamic model to derive the value at zero ionic strength and ambient by P.L. Brown et al., 2019, the partition coefficient becomes (0.06). This value is rather close to the value obtained in the present study and in a full agreement with the value obtained by Yoshida et al., 2014 considering the uncertainty of the average value (Figure 58). This shows that DFT calculations that were carried out by the present study is reliable in determining the mixing properties of $(Ba, Ra)CO_3$.

The partition coefficient of ^{226}Ra into witherite was initially thought to be higher than the values obtained in the current study and the partition coefficient reported by Yoshida et al. (2014). Langmuir & Melchior 1985 derived the radium carbonate solubility product ($K_{sp,\ RaCO_3} = 10^{-8.30}$) through extrapolation from the witherite solubility product ($K_{sp,\ witherite} = 10^{-8.58}$) as reported by Millero et al., 1984, and this value has been widely accepted for a long time. Using the solubility products ($K_{sp,\ RaCO_3} = 10^{-8.30}$) and ($K_{sp,\ witherite} = 10^{-8.58}$) along with the non-ideality parameter obtained in this study (0.58) for the substitution of radium for barium in witherite, the partition coefficient calculated using Equation 24 is (0.45). This theoretical value is significantly higher than the experimentally determined values reported in the current study and by Yoshida et al., 2014, as shown in Figure 58.

However, when applying the solubility product ($K_{sp,\ RaCO_3} = 10^{-7.57}$) derived by Brown et al., 2019 using a thermodynamic model at zero ionic strength and ambient conditions, the calculated partition coefficient is (0.06). This value aligns more closely with the experimentally obtained values from the present study and is fully consistent with Yoshida et al., 2014 when considering the uncertainty of the average value (Figure 58).

This comparison indicates that the density functional theory (DFT) calculations conducted in this study are reliable for determining the mixing properties of $(Ba, Ra)CO_3$. While the efforts of Langmuir & Melchior 1985 provided a valuable foundation in understanding radium behavior, the solubility product derived by Brown et al., 2019 offers a more accurate prediction of the partition coefficient for radium in witherite.

Though the partition coefficient derived in the present study is close to the theoretical value, a small difference between the two can be seen as the experimental value is higher (Figure 58). One can attribute such difference to the high precipitation rate (7.32), with which ^{226}Ra was being taken up into witherite structure along Ba. This implies that in the experiment for ^{226}Ra had only a short time to diffuse and redistribute, resulting in higher concentrations ^{226}Ra being trapped in the growing witherite crystal lattice compared to growth at equilibrium conditions. This is shown by the slightly higher ^{226}Ra and Ba concentrations for RW batches compared to equilibrium concentrations of both cations as can be seen in Figure 49.a,b. This indicates that the system did not attain equilibrium after 44 days reaction time.

A study carried out by Rihs, Condomines and Sigmarsson, 2000 on U, Ra, and Ba incorporation in calcite in CO_2-rich hydrothermal systems is further supporting this. The study shows that

partition coefficients can be much higher than equilibrium values due to high precipitation rates; they suggest that such higher partition coefficient can applicable to natural systems with high precipitation rates.

The small difference between the experimental and theoretical Ba concentrations that indicates unattained equilibrium could explain the difference between the particle sizes seen in Figure 48. It is likely that the rapid formation of witherite in early reaction stages resulted in small particles as nucleation theory classical dictates, then later the reaction slowed down and particles were growing but slowly and that allowed particles to grow larger.

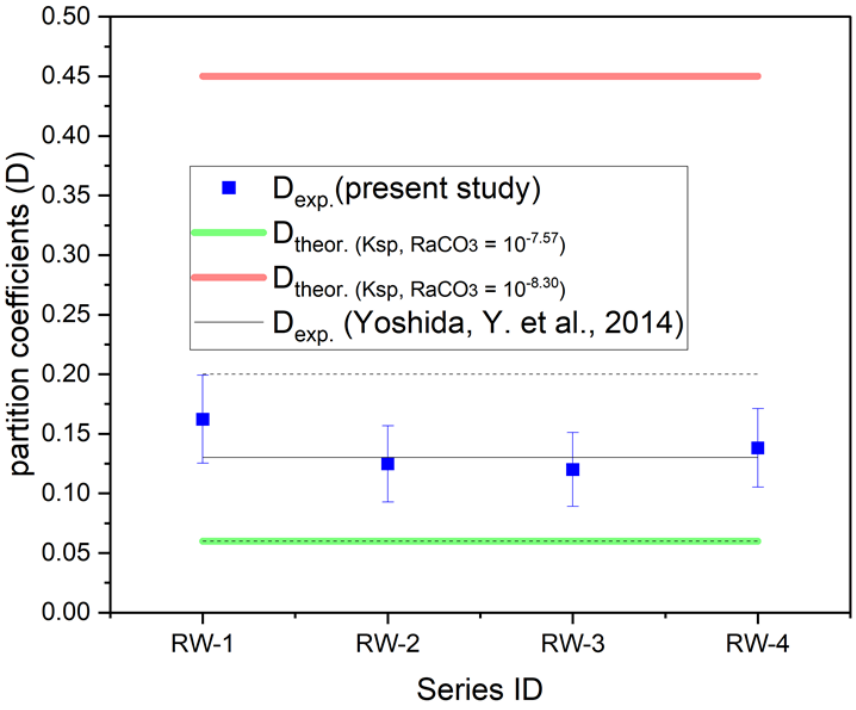

Figure 58. shows $D_{exp.}$ for radium into witherite that was obtained in the present study compared with what was obtained experimentally by Yohshida et al., 2014, a theoretical value calculated via using the long time accepted radium carbonate $RaCO_3$ solubility product ($K_{sp,\ RaCO_3} = 10^{-8.30}$) by Langmuir and Melchior, 1985 and the recently calculated ($K_{sp,\ RaCO_3} = 10^{-7.57}$) by Brown et al., 2019.

9 Summary and conclusions

This Ph.D. thesis has successfully addressed the influence of dissolved carbonate on the uptake of radium by two naturally occurring host minerals, barite and witherite. In order to study the processes of coupled barite dissolution and witherite precipitation as well as the uptake of radium and strontium in the two host minerals, a combination of different experimental, analytical and computational approaches were applied. Results of this Ph.D. work offer information on the behavior of Ra in different ambient geochemical settings, which can be implemented when considering protective strategies to mitigate the impact of ^{226}Ra and other abundant Ra isotopes on human health and environmental and safety.

Firstly, outcomes are summarized and conclusions drawn based on experimental and theoretical studies on recrystallization of barite to witherite in the presence of aqueous carbonate. Based on this, the summary and conclusions deal with experimental and theoretical studies on incorporation of Ra during Ra doped barite to witherite transformation and coprecipitation in Ba^{2+}(aq) + CO_3^{2-}(aq) + Ra^{2+}(aq) bearing solutions.

Experiments on barite single crystals confirmed the familiar picture of recrystallization reactions (replacement, coupled recrystallization) and precipitation of a secondary mineral, here witherite. Experiments with barite powder samples showed, however, that powders are by no means just small single crystals, but that an enormously increased complexity of the processes taking place can be observed here due to shifts in the reaction rates. Recrystallization experiments with macroscopic crystal cubes of pure natural Androvo barite and natural Iberg barite containing traces of Sr demonstrate that at ambient temperature even at high carbonate concentration, and thereby a high degree of oversaturation with respect to witherite, barite reacts slowly to witherite. Only at 60°C in highly alkaline solution with an elevated carbonate concentration (pH 11 and 0.1 M CO_3^{2-}), a considerable amount of barite dissolves and witherite is formed as secondary mineral. According to PHREEQC calculations for full equilibration of the Ba^{2+}(aq)-SO_4^{2-}-CO_3^{2-}-H_2O-system, a solid phases composition of approximately 60 wt.% of barite and 40 wt.% witherite is expected under these conditions. However, after one month reaction time, the replaced solid sample contains about 15 wt.% of witherite in the experiments with Iberg barite single crystals, compared to only about 5 wt.% of witherite in the experiments with Androvo barite single crystals. Both type of barite crystals display an increasing rim of witherite around the barite relict, with considerable differences between the crystals in the experiments with Androvo and Iberg barite. Based on microscopic analyses it is concluded that the development of the porosity of the growing witherite layer is a major controlling factor for the progress of reaction. The experimental results indicate that passivation of the barite surface by the growing witherite is to be expected to last over longer periods of time. In pure Androvo barite, a sharp interface between barite and the witherite rim zone, associated with a sharp decrease in sulfur and an increase in carbon is observed. The Ba^{2+} content slightly increases due to the change in stoichiometry from barite, Ba:S:4O, to witherite Ba:C:3O. Notably, in experiments with Iberg barite the Sr/Ba ratio across the interface between barite and witherite does not change significantly, although thermodynamically a significant change would be expected. This indicates that at the barite-witherite interface, where the replacement reaction takes place, Ba^{2+} and Sr^{2+} cations released by barite dissolution are incorporated into witherite at the ratio of their dissolution from the initial $(Ba,Sr)SO_4$ solid-solution. This leads to the

conclusion that the thermodynamic affinities for incorporation Ba^{2+} and Sr^{2+} into witherite under these transport-controlled conditions play no or only a very minor role.

The progress of barite-witherite transformation (uncoupled recrystallization) of the powder samples of natural Androvo barite, natural Iberg barite and of synthetic Sachtleben barite initially display similar trends compared to those of the replacement of macroscopic Androvo and Iberg barite single crystals. As expected, reaction rates in the experiments with powders of Androvo and Iberg barites are significantly faster than those with single crystal cubes of Androvo and Iberg barites. At the onset of the powder transformation experiments a fast production of witherite is observed. Yet, the reaction slows down after about one week and does not reach the theoretically achievable limit of witherite production, as calculated by means of PHREEQC calculations for full equilibration of the Ba^{2+}(aq)-SO_4^{2-}-CO_3^{2-}-H_2O-system. Whereas Sachtleben and Iberg barite powders react at a similar rate, Androvo barite powder shows a significantly lower reactivity. This observation is in accordance with a relatively slow reaction rate of Androvo barite in the replacement experiments with single crystals. One may assume that differences in porosities of the newly formed witherite rims are controlling the reaction rates of the barite powders, too. Yet, SEM-EDX investigations demonstrate that in the powders, surface crystal rebuilding / transformation at a reactive barite-witherite interface plays a subordinate role. Instead, barite dissolves, while witherite crystals often form in idiomorphic shapes, which occur in diverse spatial arrangements with respect to the initial barite. The ratios between barite dissolution rate and witherite growth rate are decisive for the difference in the reaction progress from barite dissolution, diffusion of Ba^{2+}(aq)-CO_3^{2-}-ions in solution and / or in the solid phase and precipitation of witherite. If the barite dissolution is the slower reaction and thereby the rate-controlling process, a barite-witherite interface around a barite relict is formed, as in the replacement experiments with single crystal cubes. In contrast, when witherite growth is slower than barite dissolution, and therefore the rate-controlling reaction step, the witherite crystals grow spatially independently of the initial barite crystals, in some cases resulting in spatially separated barite relicts and newly formed witherite crystals. Results of this Ph.D. thesis show that Ra^{2+} release from Ra doped barite beyond the level of solubility of $(Ba,Ra)SO_4$ solid-solution is not to be expected. The thermodynamic model for Ra incorporation in barite was further substantiated by experiments and density functional theory, DFT, simulations. A thermodynamic model for Ra incorporation into witherite was newly created. The DFT calculation results show that the incorporation of radium in barite and witherite is almost ideal with rather small Guggenheim parameters ("non-ideality parameter") of 0.84 and 0.58 respectively. The value for radium in barite agrees very well with earlier

calculations (Vinograd et al, 2013), and is in agreement with experimental findings within the uncertainties of the relevant parameters (Brandt et al., 2015; Heberling et al., 2018). Co-precipitation experiments at 60°C carried out as part of this work are also in excellent agreement with this value, $D_{exp} = 0.34 \pm 0.14$ and $D_{theo} = 0.42$. Co-precipitation experiments for Ra-incorporation into $BaCO_3$ over a wide range of Ra concentrations yield a distribution coefficient of $D_{exp} = 0.15 \pm 0.05$. Only few literature data is available for the Ra-witherite system. An existing partition coefficient under equilibrium condition, $D = 0.13 \pm 0.07$ (Yoshida et al., 2015), agrees with these measurements. Together with the Guggenheim parameter of 0.58 calculated here, this results in partition coefficients of $D_{theo} = 0.06$, which is close to the lower limit of the value of D_{exp} of the present study. The attempt to simulate the incorporation of sulfate into witherite by means of DFT calculation leads to a highly distorted structure indicating an extreme non-ideality of the solid solution. This corresponds to the experimental findings that sulfate could never be detected in witherite from the recrystallization experiments. Experiments on the recrystallization of radium-containing barite (Ra-barite) to radium-containing witherite showed that the various Ra barites investigated (from Heberling et al., 2018 and material synthesized in this study) were quite inert, interestingly also significantly less reactive than comparable Ra-free barites, so that it can be assumed that the radium content actually has an inhibiting influence on the barite reactivity. Nevertheless, microscopic Ra-witherite crystals were observed. But these did not contain enough radium for a quantitative evaluation of radium incorporation after recrystallization.

References

Abdelouas, A., Crovisier, J.-L., Lutze, W., Grambow, B., Dran, J.-C., Müller, R., 1997. Surface layers on a borosilicate nuclear waste glass corroded in MgCl2 solution. Journal of Nuclear Materials 240(2), 100-111.

Agency, I.A.E., 2004. Extent of environmental contamination by naturally occurring radioactive material (NORM) and technological options for mitigation. International Atomic Energy Agency.

Ahmed, R.S., 2021. A review on soil radionuclide distribution in Iraq analysed using gamma ray spectroscopy. Environmental Forensics 22(1-2), 91-98.

Al-Awad, M.N., Al-Qasabi, A.O., 2001. Characterization and testing of Saudi barite for potential use in drilling operations. Journal of King Saud University-Engineering Sciences 13(2), 287-298.

Alexiev, D., Reinhard, M., Mo, L., Rosenfeld, A., Smith, M., 2002. Review of Ge detectors for gamma spectroscopy. Australasian physical & engineering sciences in medicine 25(3), 102-109.

Altree-Williams, A., Pring, A., Ngothai, Y., Brugger, J., 2015. Textural and compositional complexities resulting from coupled dissolution–reprecipitation reactions in geomaterials. Earth-Science Reviews 150, 628-651.

Antao, S.M., 2012. Structural trends for celestite (SrSO4), anglesite (PbSO4), and barite (BaSO4): Confirmation of expected variations within the SO4 groups. American Mineralogist 97(4), 661-665.

Arai, K., Toguri, J., 1984. Leaching of lead sulphate in sodium carbonate solution. Hydrometallurgy 12(1), 49-59.

Arai, K., Toguri, J., 1984. Leaching of lead sulphate in sodium carbonate solution. Hydrometallurgy 12(1), 49-59.

Attallah, M., Hamed, M.M., El Afifi, E., Aly, H., 2015. Removal of 226Ra and 228Ra from TENORM sludge waste using surfactants solutions. J Environ Radioactiv 139, 78-84.

Balasubramanian, K., Encyclopedia of Computational Chemistry, Wiley-Inter-science, New York, NY (1998).

Baldasari, A., Speer, J., 1979. Witherite composition, physical properties, and genesis. American Mineralogist 64(7-8), 742-747.

Barton, P.B., 1957. Some limitations on the possible composition of the ore-forming fluid. Economic Geology 52(4), 333-353.

Benjamin, M.M., 2014. Water chemistry. Waveland Press.

Berner, U., 1992. Evolution of pore water chemistry during degradation of cement in a radioactive waste repository environment. Waste management 12(2-3), 201-219.

Blochl, P.E., 1994. Projector Augmented-Wave Method. Physical Review B 50(24), 17953-17979. doi.org/DOI 10.1103/PhysRevB.50.17953.

Brandt, F., Curti, E., Klinkenberg, M., Rozov, K., Bosbach, D., 2015. Replacement of barite by a (Ba, Ra) SO4 solid solution at close-to-equilibrium conditions: A combined experimental and theoretical study. Geochim Cosmochim Ac 155, 1-15.

Brantley, S.L., Kubicki, J.D., White, A.F., 2008. Kinetics of water-rock interaction.

Brower, E., Renault, J., 1971. Solubility and enthalpy of the barium-strontium sulfate solid solution series. New Mexico State Bureau of Mines and Mineral Resources.

Brown, P.L., Ekberg, C., Matyskin, A.V., 2019. On the solubility of radium and other alkaline earth sulfate and carbonate phases at elevated temperature. Geochim Cosmochim Ac 255, 88-104.

Brown, P.L., Ekberg, C., Ramebäck, H., Hedström, H., Matyskin, A., 2015. Solubility of radium and strontium sulfate across the temperature range of 0 to 300 C, Uranium-Past and Future Challenges: Proceedings of the 7th International Conference on Uranium Mining and Hydrogeology. Springer, pp. 553-564.

Bulatovic, S.M., 2015. Beneficiation of barite ores. Handbook of flotation reagents: chemistry, theory and practice, 129-141.

Bunaciu, A.A., UdriŞTioiu, E.G., Aboul-Enein, H.Y., 2015. X-ray diffraction: instrumentation and applications. Critical reviews in analytical chemistry 45(4), 289-299.

Buzgar, N., Apopei, A.I., 2009. The Raman study of certain carbonates. Geologie Tomul L 2(2), 97-112.

Castillejos, A., Uribe, A., 1996. The direct conversion of celestite to strontium carbonate in sodium carbonate aqueous media. Hydrometallurgy 40(1-2), 207-222.

Chang, L.L., 1971. Subsolidus Phase Relations in the Aragonite-Type Carbonates: I. The System Cac03-SrC03-BaC03. American Mineralogist: Journal of Earth and Planetary Materials 56(9-10), 1660-1673.

Connolly, J.R., 2007. Introduction to X-ray powder diffraction. European Physical Society of Journal 4, p400.

Curti, E., Fujiwara, K., Iijima, K., Tits, J., Cuesta, C., Kitamura, A., Glaus, M., Müller, W., 2010. Radium uptake during barite recrystallization at 23±2 C as a function of solution composition: An experimental 133Ba and 226Ra tracer study. Geochim Cosmochim Ac 74(12), 3553-3570.

Curti, E., Kulik, D., Tits, J., 2005. Solid solutions of trace Eu (III) in calcite: Thermodynamic evaluation of experimental data over a wide range of pH and pCO2. Geochim Cosmochim Ac 69(7), 1721-1737.

Das, R.S., Agrawal, Y., 2011. Raman spectroscopy: Recent advancements, techniques and applications. Vibrational spectroscopy 57(2), 163-176.

Deer, W., Howie, R., Zussman, J., 1992. Serpentine. Deer WA, Howie RA, Zussman J. An introduction to the rock-forming minerals. 2nd ed. Pearson Education Limited, 344-352.

Desideri, D., Meli, M.A., Feduzi, L., Roselli, C., 2006. The importance of radiochemistry for the characterization of NORM and of environments contaminated by NORM. Int J Environ an Ch 86(8), 601-613. doi.org/10.1080/03067310500392011.

Doerner, H.A., Hoskins, W.M., 1925. Co-Precipitation of radium and barium sulfates1. Journal of the American Chemical Society 47(3), 662-675.

Douvris, C., Trey, V., Bussan, D., Bartzas, G., Thomas, R., 2023. How ICP-OES changed the face of trace element analysis: Review of the global application landscape. Sci Total Environ, 167242.

Efremov, E.V., Ariese, F., Gooijer, C., 2008. Achievements in resonance Raman spectroscopy: Review of a technique with a distinct analytical chemistry potential. Analytica chimica acta 606(2), 119-134.

Fernandez-Diaz, L., Pina, C.M., Astilleros, J.M., Sanchez-Pastor, N., 2009. The carbonatation of gypsum: Pathways and pseudomorph formation. American Mineralogist 94(8-9), 1223-1234.

Forjanes, P., Astilleros, J.M., Fernández-Díaz, L., 2020. The formation of barite and celestite through the replacement of gypsum. Minerals 10(2), 189.

Gaines, R.V., Skinner, H.C.W., Foord, E.E., Mason, B., Rosenzweig, A., 1998. Dana's New Mineralogy. Journal of the American Chemical Society 120(11), 2693.

Glynn, P., 2000. Solid-solution solubilities and thermodynamics: sulfates, carbonates and halides. Reviews in Mineralogy and Geochemistry 40(1), 481-511.

Goldstein, J.I., Newbury, D.E., Michael, J.R., Ritchie, N.W., Scott, J.H.J., Joy, D.C., 2017. Scanning electron microscopy and X-ray microanalysis. springer.

Gong, Y., Dutrizac, J., Chen, T., 1992. The conversion of lead sulphate to lead carbonate in sodium carbonate media. Hydrometallurgy 28(3), 399-421.

Gonzalez-Illanes, T., Borrero, M.T., Herraez, M.M., Pimentel, C., Pina, C.M., 2017. Pseudomorphic replacement of Mg–Ca carbonates after gypsum and anhydrite. ACS Earth and Space Chemistry 1(3), 168-178.

Gorski, C.A., Fantle, M.S., 2017. Stable mineral recrystallization in low temperature aqueous systems: A critical review. Geochim Cosmochim Ac 198, 439-465.

Grandstaff, D., 1978. Changes in surface area and morphology and the mechanism of forsterite dissolution. Geochim Cosmochim Ac 42(12), 1899-1901.

Griffith, E.M., Paytan, A., 2012. Barite in the ocean–occurrence, geochemistry and palaeoceanographic applications. Sedimentology 59(6), 1817-1835.

Grivé, M., Duro, L., Colàs, E., Giffaut, E., 2015. Thermodynamic data selection applied to radionuclides and chemotoxic elements: an overview of the ThermoChimie-TDB. Applied Geochemistry 55, 85-94.

Guggenheim, E., 1937. The theoretical basis of Raoult's law. Transactions of the Faraday Society 33, 151-156.

Gundlach, H. (1959) UntersuchuDgen zur Geochemie des Strontians auf hydrothermalen Lagerstatten. Geol. Jahrb., 76, 637712.

Hancox, E., 1934. Witherite and barytes. Mining Mag 51, 76-79.

Hanor, J.S., 2000. Barite–celestine geochemistry and environments of formation. Reviews in Mineralogy and Geochemistry 40(1), 193-275.

Hazen, R.M., Downs, R.T., Jones, A.P., Kah, L., 2013. Carbon mineralogy and crystal chemistry. Reviews in Mineralogy and Geochemistry 75(1), 7-46.

Heberling, F., Bosbach, D., Eckhardt, J.-D., Fischer, U., Glowacky, J., Haist, M., Kramar, U., Loos, S., Müller, H.S., Neumann, T., 2014. Reactivity of the calcite–water-interface, from molecular scale processes to geochemical engineering. Applied geochemistry 45, 158-190.

Heberling, F., Metz, V., Böttle, M., Curti, E., Geckeis, H., 2018. Barite recrystallization in the presence of 226Ra and 133Ba. Geochim Cosmochim Ac 232, 124-139.

Helz, G., Holland, H., 1965. The solubility and geologic occurrence of strontianite. Geochim Cosmochim Ac 29(12), 1303-1315.

Hohenberg, P., Kohn, W., 1964. Inhomogeneous electron gas. Physical review 136(3B), B864.

Hou, X., Jones, B.T., 2000. Inductively coupled plasma/optical emission spectrometry. John Wiley & Sons Chichester, UK, pp. 9468-9485.

Hövelmann, J., Austrheim, H., Jamtveit, B., 2012. Microstructure and porosity evolution during experimental carbonation of a natural peridotite. Chem Geol 334, 254-265.

Hövelmann, J., Austrheim, H., Jamtveit, B., 2012. Microstructure and porosity evolution during experimental carbonation of a natural peridotite. Chem Geol 334, 254-265.

Hummel, W., Berner, U., Curti, E., Pearson, F.J., Thoenen, T., 2002. Nagra/PSI chemical thermodynamic data base 01/01. Radiochimica Acta 90(9-11), 805-813.

Hummel, W., Berner, U., Curti, E., Pearson, F.J., Thoenen, T., 2002. Nagra/PSI chemical thermodynamic data base 01/01. Radiochimica Acta 90(9-11), 805-813.

Jagtap, R., Ambre, A., 2006. Overview literature on atomic force microscopy (AFM): Basics and its important applications for polymer characterization.

King, H.E., Plümper, O., Putnis, A., 2010. Effect of secondary phase formation on the carbonation of olivine. Environ Sci Technol 44(16), 6503-6509.

Klinkenberg, M., Brandt, F., Breuer, U., Bosbach, D., 2014. Uptake of Ra during the recrystallization of barite: A microscopic and time of flight-secondary ion mass spectrometry study. Environ Sci Technol 48(12), 6620-6627.

Knoll, G.F., 2010. Radiation detection and measurement. John Wiley & Sons.

Kohn, W., Sham, L.J., 1965. Self-consistent equations including exchange and correlation effects. Physical review 140(4A), A1133.

Kolawole, F., Bergerman, M., Ulsen, C., Kolawole, S., 2019. a Global Review of Barite Beneficiation Processes: a Case Study of Azara Barite Ores in Nigeria. Nigerian Journal of Engineering Vol 26(1).

Kondash, A.J., Warner, N.R., Lahav, O., Vengosh, A., 2014. Radium and Barium Removal through Blending Hydraulic Fracturing Fluids with Acid Mine Drainage. Environ Sci Technol 48(2), 1334-1342. doi.org/10.1021/es403852h.

Kresse, G., Furthmüller, J., 1996. Efficiency of ab-initio total energy calculations for metals and semiconductors using a plane-wave basis set. Computational materials science 6(1), 15-50.

Kresse, G., Furthmüller, J., 1996. Efficient iterative schemes for ab initio total-energy calculations using a plane-wave basis set. Physical review B 54(16), 11169.

Kresse, G., Hafner, J., 1993. Ab initio molecular dynamics for liquid metals. Physical review B 47(1), 558.

Kresse, G., Joubert, D., 1999. From ultrasoft pseudopotentials to the projector augmented-wave method. Physical review b 59(3), 1758.

Krumgalz, B., 2018. Temperature dependence of mineral solubility in water. Part 3. Alkaline and alkaline earth sulfates. Journal of Physical and Chemical Reference Data 47(2).

Lafuente, B., Downs, R.T., Yang, H., Stone, N., Armbruster, T., Danisi, R.M., 2015. The power of databases: the RRUFF project. Highlights in mineralogical crystallography 1, 25.

Langmuir, D., Melchior, D., 1985. The geochemistry of Ca, Sr, Ba and Ra sulfates in some deep brines from the Palo Duro Basin, Texas. Geochim Cosmochim Ac 49(11), 2423-2432.

Li, S., Xu, J., Luo, G., 2007. Control of crystal morphology through supersaturation ratio and mixing conditions. Journal of Crystal Growth 304(1), 219-224.

Liang, Y., Guan, L., Xu, X., Han, S., Guo, J., Wang, J., Chen, X., Zhang, Z., Li, X., 2020. Effects of the Dopant Site on the Absorption Properties of CsPb1–x M x I2Br (M= Ge, Sn, Sr, and Cu): A First-Principles Investigation. The Journal of Physical Chemistry C 124(11), 6028-6037.

Martin, A., Crusius, J., McNee, J.J., Yanful, E., 2003. The mobility of radium-226 and trace metals in pre-oxidized subaqueous uranium mill tailings. Applied Geochemistry 18(7), 1095-1110.

Matyskin, A.V., Ebin, B., Allard, S., Torapava, N., Eriksson, L., Persson, I., Brown, P.L., Ekberg, C., 2023. Disordered Crystal Structure and Anomalously High Solubility of Radium Carbonate. Inorganic Chemistry 62(30), 12038-12049. doi.org/10.1021/acs.inorgchem.3c01513.

Mohammed, A., Abdullah, A., 2018. Scanning electron microscopy (SEM): A review, Proceedings of the 2018 International Conference on Hydraulics and Pneumatics—HERVEX, Băile Govora, Romania. pp. 7-9.

Momma, K., Izumi, F., 2008. VESTA: a three-dimensional visualization system for electronic and structural analysis. Journal of Applied crystallography 41(3), 653-658.

Parkhurst, D.L., Appelo, C., 1999. User's guide to PHREEQC (Version 2): A computer program for speciation, batch-reaction, one-dimensional transport, and inverse geochemical calculations. US Geological Survey.

Perdew, J.P., Burke, K., Ernzerhof, M., 1996. Generalized gradient approximation made simple. Physical review letters 77(18), 3865.

Polly, R., Heberling, F., Schimmelpfennig, B., Geckeis, H., 2017. Quantum chemical investigation of the selenite incorporation into the calcite (1014) surface. The Journal of Physical Chemistry C 121(37), 20217-20228.

Poonoosamy, J., Wanner, C., Alt Epping, P., Águila, J., Samper, J., Montenegro, L., Xie, M., Su, D., Mayer, K., Mäder, U., 2021. Benchmarking of reactive transport codes for 2D simulations with mineral dissolution–precipitation reactions and feedback on transport parameters. Computational geosciences 25, 1337-1358.

Prieto, M., 2009. Thermodynamics of solid solution-aqueous solution systems. Reviews in Mineralogy and Geochemistry 70(1), 47-85.

Prieto, M., 2009. Thermodynamics of solid solution-aqueous solution systems. Reviews in Mineralogy and Geochemistry 70(1), 47-85.

Prieto, M., Astilleros, J.M., Fernández-Díaz, L., 2013. Environmental remediation by crystallization of solid solutions. Elements 9(3), 195-201.

Prieto, M., Fernández-González, A., Putnis, A., Fernández-Díaz, L., 1997. Nucleation, growth, and zoning phenomena in crystallizing (Ba, Sr) CO3, Ba (SO4, CrO4),(Ba, Sr) SO4, and (Cd, Ca) CO3 solid solutions from aqueous solutions. Geochim Cosmochim Ac 61(16), 3383-3397.

Putnis, A., 2002. Mineral replacement reactions: from macroscopic observations to microscopic mechanisms. Mineralogical Magazine 66(5), 689-708.

Putnis, A., 2009. Mineral replacement reactions. Reviews in mineralogy and geochemistry 70(1), 87-124.

Putnis, A., 2015. Transient porosity resulting from fluid–mineral interaction and its consequences. Reviews in Mineralogy and Geochemistry 80(1), 1-23.

Putnis, A., 2021. Fluid–mineral interactions: controlling coupled mechanisms of reaction, mass transfer and deformation. Journal of Petrology 62(12), egab092.

Putnis, A., Putnis, C.V., 2007. The mechanism of reequilibration of solids in the presence of a fluid phase. Journal of Solid State Chemistry 180(5), 1783-1786.

Putnis, C.V., Mezger, K., 2004. A mechanism of mineral replacement: isotope tracing in the model system KCl-KBr-H2O. Geochim Cosmochim Ac 68(13), 2839-2848.

Putnis, C.V., Tsukamoto, K., Nishimura, Y., 2005. Direct observations of pseudomorphism: compositional and textural evolution at a fluid-solid interface. American Mineralogist 90(11-12), 1909-1912.

Qian, G., Brugger, J., Skinner, W.M., Chen, G., Pring, A., 2010. An experimental study of the mechanism of the replacement of magnetite by pyrite up to 300 C. Geochim Cosmochim Ac 74(19), 5610-5630.

Redlich, O., Kister, A., 1948. Thermodynamics of nonelectrolyte solutions-xyt relations in a binary system. Industrial & Engineering Chemistry 40(2), 341-345.

Renderson, L., Kracek, F., Parsons, C.L., Moore, R., Lind, S., Schaefer, O., Niermann, J., Scholl, C.E., Strong, R., Mc Coy, H., 1928. Die fraktionierte fällung von barium-und radiumchromaten. Zeitschrift für analytische Chemie 74, 255-259.

Rendón-Angeles, J., Matamoros-Veloza, Z., López-Cuevas, J., Pech-Canul, M., Yanagisawa, K., 2008. Stability and direct conversion of mineral barite crystals in carbonated hydrothermal fluids. Journal of materials science 43(7), 2189-2197.

Rendon-Angeles, J., Yanagisawa, K., Ishizawa, N., Oishi, S., 2000. Conversion of calcium fluorapatiteinto calcium hydroxyapatite under alkaline hydrothermal conditions. Journal of Solid State Chemistry 151(1), 65-72.

Rihs, S., Condomines, M., Sigmarsson, O., 2000. U, Ra and Ba incorporation during precipitation of hydrothermal carbonates: Implications for 226Ra-Ba dating of impure travertines. Geochim Cosmochim Ac 64(4), 661-671.

Rostron, P., Gaber, S., Gaber, D., 2016. Raman spectroscopy, review. laser 21, 24.

Rowland, R.E., Stehney, A.F., Lucas, H.F., 1978. Dose-Response Relationships for Female Radium Dial Workers. Radiat Res 76(2), 368-383. doi.org/Doi 10.2307/3574786.

Ruiz-Agudo, E., Putnis, C., Putnis, A., 2014. Coupled dissolution and precipitation at mineral–fluid interfaces. Chem Geol 383, 132-146.

Schwarzer, H.C., Peukert, W., 2002. Experimental investigation into the influence of mixing on nanoparticle precipitation. Chemical engineering & technology 25(6), 657-661.

Shikazono, N., 1994. Precipitation mechanisms of barite in sulfate-sulfide deposits in back-arc basins. Geochim Cosmochim Ac 58(10), 2203-2213.

Shtukenberg, A.G., Punin, Y.O., Azimov, P., 2006. Crystallization kinetics in binary solid solution–aqueous solution systems. American Journal of Science 306(7), 553-574.

Stober, I., 2014. Hydrochemical properties of deep carbonate aquifers in the SW German Molasse basin. Geothermal Energy 2, 1-20.

Suárez-Orduña, R., Rendón-Angeles, J., López-Cuevas, J., Yanagisawa, K., 2004. The conversion of mineral celestite to strontianite under alkaline hydrothermal conditions. Journal of Physics: Condensed Matter 16(14), S1331.

Suárez-Orduña, R., Rivas-Vazquez, L., Rendón-Angeles, J., Yanagisawa, K., 2009. Kinetic study of the conversion of mineral barite to barium carbonate under alkaline hydrothermal conditions. Mineral Processing and Extractive Metallurgy 118(1), 18-22.

Varley, A., Tyler, A., Smith, L., Dale, P., Davies, M., 2016. Mapping the spatial distribution and activity of 226Ra at legacy sites through Machine Learning interpretation of gamma-ray spectrometry data. Sci Total Environ 545, 654-661.

Vinograd, V., Brandt, F., Rozov, K., Klinkenberg, M., Refson, K., Winkler, B., Bosbach, D., 2013. Solid–aqueous equilibrium in the BaSO4–RaSO4–H2O system: first-principles calculations and a thermodynamic assessment. Geochim Cosmochim Ac 122, 398-417.

Wang, C., Zhou, L., Zhang, S., Wang, L., Wei, C., Song, W., Xu, L., Zhou, W., 2021. Morphology of Barite Synthesized by In-Situ Mixing of Na2SO4 and BaCl2 Solutions at 200° C. Crystals 11(8), 962.

Wang, X., Li, W., Harrington, R., Liu, F., Parise, J.B., Feng, X., Sparks, D.L., 2013. Effect of ferrihydrite crystallite size on phosphate adsorption reactivity. Environ Sci Technol 47(18), 10322-10331.

Weber, J., Barthel, J., Brandt, F., Klinkenberg, M., Breuer, U., Kruth, M., Bosbach, D., 2016. Nano-structural features of barite crystals observed by electron microscopy and atom probe tomography. Chem Geol 424, 51-59.

Weber, J., Barthel, J., Klinkenberg, M., Bosbach, D., Kruth, M., Brandt, F., 2017. Retention of 226Ra by barite: The role of internal porosity. Chem Geol 466, 722-732.

Welham, N., Llewellyn, D., 1998. Mechanical enhancement of the dissolution of ilmenite. Minerals Engineering 11(9), 827-841.

Weller, J. M., R. M. Grogan and F. R. Tippie (1952) Geology of the fluorite deposits of Illinois. Illinois State Geol. Sum. Bull.76.

White, G.J., Rood, A.S., 2001. Radon emanation from NORM-contaminated pipe scale and soil at petroleum industry sites. J Environ Radioactiv 54(3), 401-413. doi.org/Doi 10.1016/S0265-931x(00)00156-9.

White, W., 1997. Thermodynamic equilibrium, kinetics, activation barriers, and reaction mechanisms for chemical reactions in karst terrains. Environmental Geology 30, 46-58.

Wong, D., Jaworski, Z., Nienow, A., 2001. Effect of ion excess on particle size and morphology during barium sulphate precipitation: an experimental study. Chemical engineering science 56(3), 727-734.

Ye, Y., Smyth, J.R., Boni, P., 2012. Crystal structure and thermal expansion of aragonite-group carbonates by single-crystal X-ray diffraction. American Mineralogist 97(4), 707-712.

Yoshida, Y., Nakazawa, T., Yoshikawa, H., 2015. Partition coefficient of Ra in witherite. Journal of Radioanalytical and Nuclear Chemistry 303, 147-152.

Yuan, K., Starchenko, V., Rampal, N., Yang, F., Yang, X., Xiao, X., Lee, W.-K., Stack, A.G., 2021. Opposing effects of impurity ion Sr2+ on the heterogeneous nucleation and growth of barite (BaSO4). Crystal growth & design 21(10), 5828-5839.

Zhang, Z., Zhou, F., Lavernia, E., 2003. On the analysis of grain size in bulk nanocrystalline materials via X-ray diffraction. Metallurgical and Materials Transactions A 34, 1349-1355.

Zhou, G.-T., Yao, Q.-Z., Ni, J., Jin, G., 2009. Formation of aragonite mesocrystals and implication for biomineralization. American Mineralogist 94(2-3), 293-302.

Appendices

Appendix. A

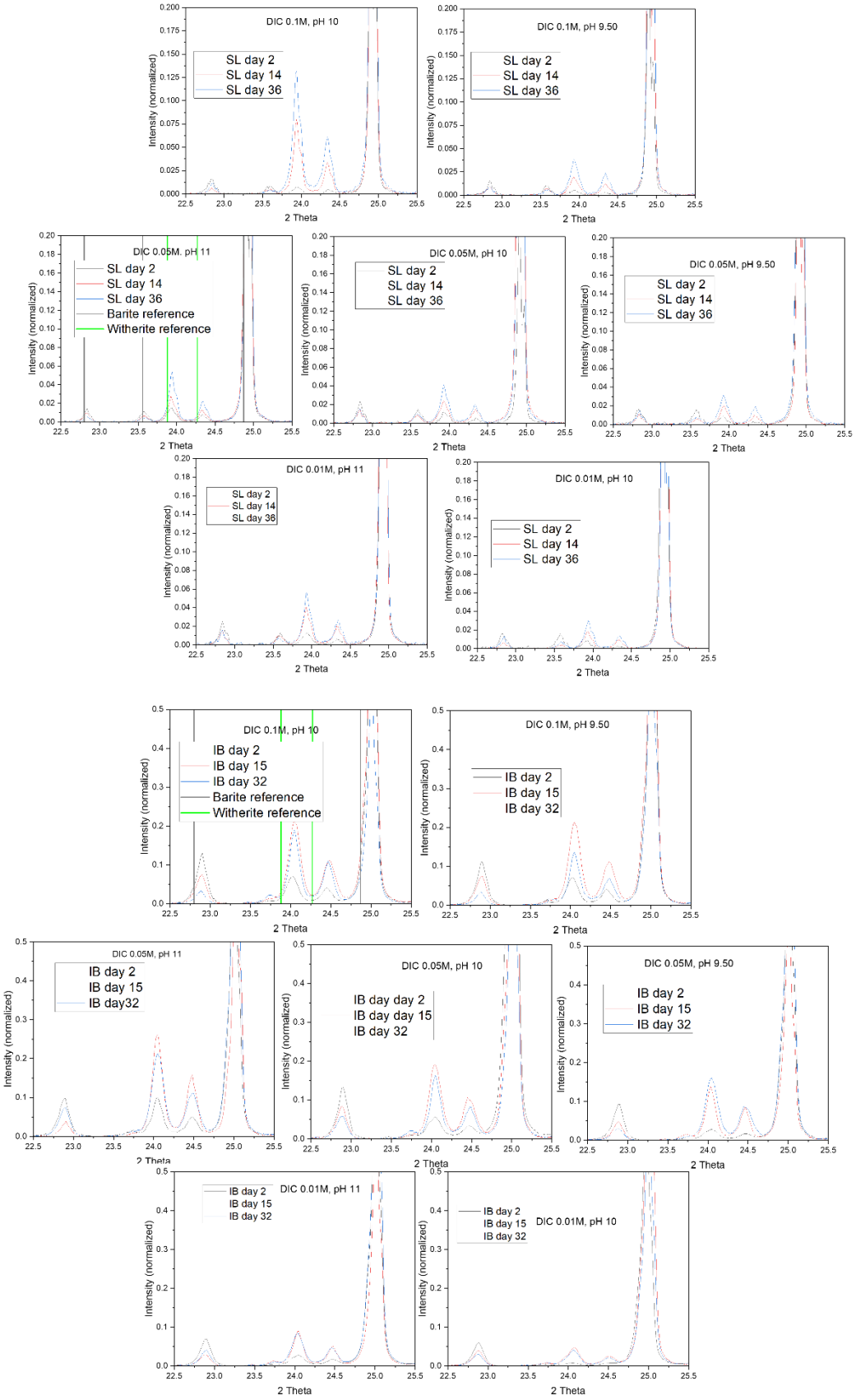

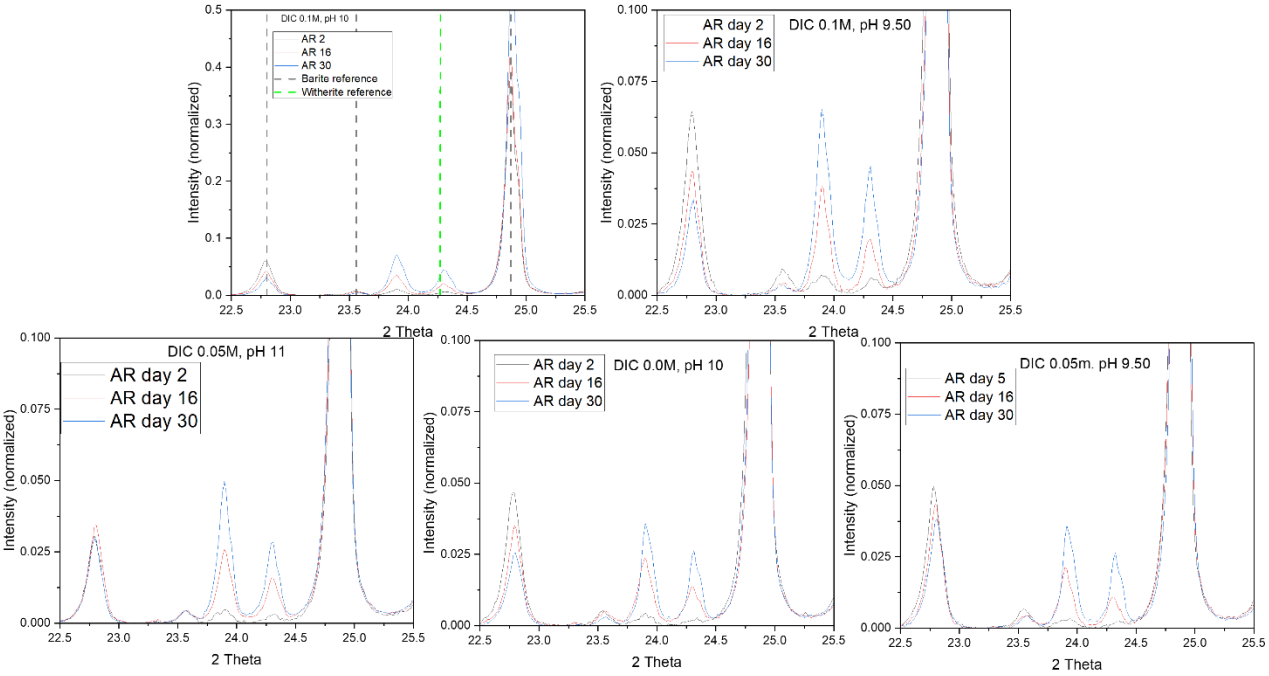

Figure A.1. XRD Diffractograms of the different types of barites that were reacted with carbonate solutions of concentration (0.1M, 0.05M and 0.01M) and pH 9.50, 10 and 11 for selected time intervals. IB shows witherite patterns shift to a higher angle. Reference diffractograms for phases involved in the reactions (witherite and strontianite references were obtained from Ye, Y., Smyth and Boni 2012, whereas barite and celestine from Antao, 2012.

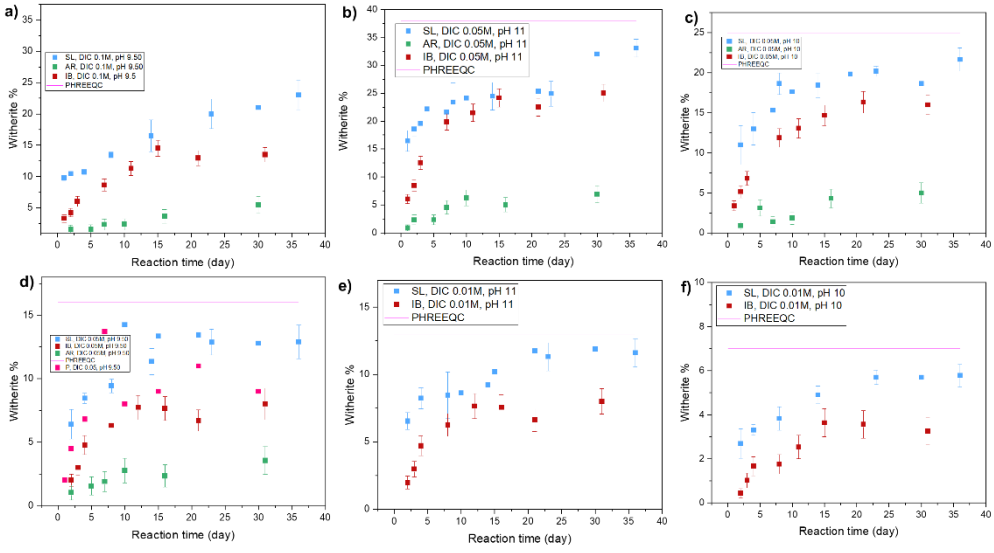

Figure A.2. Witherite percentages for different powders that reacted with carbonate (0.1M, 0.05M and 0.01M) and pH 11, 10 and 9.50.